THESIS FOR THE DEGREE OF DOCTOR OF PHILOSOPHY

Unlocking the potential of a caged star: Thermoelectric quaternary clathrates

JOAKIM BRORSSON

Department of Chemistry and Chemical Engineering
CHALMERS UNIVERSITY OF TECHNOLOGY
Göteborg, Sweden 2021

Unlocking the potential of a caged star:
Thermoelectric quaternary clathrates
JOAKIM BRORSSON

ISBN 978-91-7905-531-8
Doktorsavhandlingar vid Chalmers tekniska högskola. Ny serie nr 4998
ISSN 0346-718X

Department of Chemistry and Chemical Engineering
Chalmers University of Technology
SE-412 96 Göteborg, Sweden
Telephone +46 31 772 00 00

Cover: "A caged star can never fall for it has yet to rise". Illustration showing a typical clathrate structure surrounded by ternary diagrams showing site occupancy factors for $Ba_8Al_xGa_yGe_{46-x-y}$. For clarification, see Fig. 4.7.

Chalmers digitaltryck
Göteborg, Sweden 2021

Unlocking the potential of a caged star: Thermoelectric quaternary clathrates

JOAKIM BRORSSON
Department of Chemistry and Chemical Engineering
Chalmers University of Technology

Abstract

Heat losses are an inevitable consequence of any energy conversion process, dictated by the second law of thermodynamics. This not only leads to an eternal struggle, via the pursuit of maximal efficiency, it also undermines our efforts to solve the two issues that pose the most significant challenges to modern society: climate change and the worlds surging energy need. Thanks to our inherent ingenuity, humankind has, however, been adept at finding ways of harnessing the power of heat; from the fires that lit up the neolithic era to the steam engines of the industrial revolution. Thermoelectrics can, in some sense, be seen as the next step in this endeavour, since they allow the direct conversion of a temperature difference to an electric voltage.

This thesis summarises a seven year long journey, which has focused on a fascinating and unique group of thermoelectric materials, namely inorganic clathrates. Though these have been the subject of intense research over the last three decades, many of their properties and attributes have, as of yet, not been fully explored. In particular, this project has addressed three fundamental questions: (i) *Why is the lattice thermal conductivity intrinsically low?* (ii) *What is the impact of chemical ordering on the physical properties?* (iii) *How can the electronic transport be optimised?*

Due to the inherent complexity of these materials, computational and experimental methods should ideally be used in tandem, in order to gain further insights. This project has, thus, involved the use of both atomic scale simulations, based on a combination of density functional theory, alloy cluster expansions, and Monte Carlo simulations, as well as advanced measurement and characterisation techniques. Through these efforts, the confusion regarding the origin of the low lattice thermal conductivity has partly been clarified. In addition, it has been shown that chemical ordering in these materials leads to the emergence of an order-disorder transition, which has a direct impact on the physical properties. Last but not least, it is found that the consideration of ternary systems can facilitate the enhancement of the thermoelectric performance by enabling not only independent tuning of doping level and band structure via the composition, but also manipulation of the nano- and microstructure.

Keywords: Thermoelectrics, Inorganic clathrates, Cluster expansion, Monte Carlo, Boltzmann Transport

LIST OF PUBLICATIONS

This thesis consists of four introductory chapters and the following papers:

I **Thermal conductivity in intermetallic clathrates: A first-principles perspective**
Daniel O. Lindroth, Joakim Brorsson, Erik Fransson, Fredrik Eriksson, Anders E. C. Palmqvist, and Paul Erhart
Physical Review B, **100**, 045206 (2019)

II **Enhanced thermoelectric performance of $Ba_8Ga_{16}Ge_{30}$ clathrate by modulation doping and improved carrier mobility**
Yifei Zhang, Joakim Brorsson, Ren Qiu, and Anders E. C. Palmqvist
Advanced Electronic Materials, **7**, 2000782, (2020)

III **Order—disorder transition in inorganic clathrates controls electrical transport properties**
Joakim Brorsson, Yifei Zhang, Anders E. C. Palmqvist, and Paul Erhart
Chemistry of Materials, **33**, 4500 (2021)

IV **Investigating the chemical ordering in quaternary clathrate $Ba_8Al_xGa_{16-x}Ge_{30}$**
Yifei Zhang, Joakim Brorsson, Takashi Kamiyama, Takashi Saito, Paul Erhart, and Anders E. C. Palmqvist
Submitted

V **Efficient calculation of the lattice thermal conductivity by atomistic simulations with ab-initio accuracy**
Joakim Brorsson, Arsalan Hashemi, Zheyong Fan, Erik Fransson, Fredrik Eriksson, Tapio Ala-Nissila, Arkady V. Krasheninnikov, Hannu-Pekka Komsa, and Paul Erhart
Submitted

VI **Strategic optimization of the electronic transport properties of pseudo-ternary clathrates**
Joakim Brorsson, Anders E. C. Palmqvist, and Paul Erhart
Submitted

VII **Effect of Al/Ga ratio on atomic vacancies content and thermoelectric properties in clathrates $Ba_8Al_xGa_{16-x}Ge_{30}$**
Yifei Zhang, Joakim Brorsson, Ren Qiu, Paul Erhart, and Anders E. C. Palmqvist
In manuscript

VIII **First-principles study of order-disorder transitions in pseudo-binary clathrates**
Joakim Brorsson, Anders E. C. Palmqvist, and Paul Erhart
Submitted

The author's contribution to the papers:

I Surveyed the relevant literature and extracted experimental data. Calculated vibrational spectra as well as the electronic contribution to the thermal conductivity. Responsible for revising the final version of the paper.

II Planned and tested the experimental procedure. Synthesised some of the material. Assisted with the electronic and thermal transport measurements. Participated in the analysis of the experimental data. Aided in the writing of the manuscript.

III Performed all calculations and analysed the results. Synthesised the material. Wrote the manuscript.

IV Synthesised and conducted the initial analysis of some of the material. Performed all first-principles calculations. Participated in the analysis of the experimental data. Helped write the manuscript.

V Responsible for the calculations related to clathrates. Contributed to the analysis of all results. Aided in the writing of the final version of the manuscript.

VI Performed all calculations and analysed the results. Wrote the manuscript.

VII Responsible for all first-principles calculations. Aided in the data analysis. Helped write the manuscript.

VIII Performed all calculations and analysed the results. Wrote the manuscript.

Contents

List of abbreviations

BTT Boltzmann transport theory 7, 19, 30, 34, 45, 54, 61, 63, 66, 67

CE cluster expansion 18, 19, 28, 38, 39, 45, 47–49, 52, 54

DFT density functional theory 18, 19, 31, 36, 38, 45–47, 63, 72

DOS density of state 32, 37, 63, 66–68, 75, 76, 78

DSC differential scanning calorimetry 25, 28, 38

HNEMD homogeneous nonequilibrium molecular dynamics 37, 66, 67

IFC interatomic force constant 25, 28–33, 35, 36, 45, 47, 66

MC Monte Carlo 18, 36, 38, 49, 50, 52–54, 72, 73

MD molecular dynamics 25, 31, 34–37

PF power factor 19, 23, 73–76

PGEC phonon-glass electron-crystal 8, 9, 12, 13

RTA relaxation time approximation 35, 61, 63

SOF site occupancy factor 17, 19, 38, 50, 68–73

SPS spark plasma sintering 25, 39, 55, 56, 74, 76

TPS transient plane source 25, 27

VCSGC variance constrained semi-grand canonical 50, 52

WL Wang-Landau 38, 51–53

XRF X-ray fluorescence 38, 44, 45

Imagine us saying that the organising principle in the world is mutually beneficial relationships and partnerships rather than … who wins the race
–Janine Benyus, Le génie des arbres

1 Introduction

Climate change and the world's heavy reliance on fossil energy are two of the most significant challenges facing humanity in the 21st century. According to the most recent report by the international panel on climate change (IPCC), the probability that the increase in the average temperature, which has been observed during the last 50 years, has been caused by anthropogenic activities is more than 90 % [1]. The fact that between 55 % and 65 % of the annual greenhouse gas emissions, which are the major cause of global warming, stem from the combustion of fossil fuels and industrial processes, indicates that the two aforementioned problems are strongly correlated. It can thus be concluded that research focused on the generation of clean energy or minimisation of waste is a key area where the scientific community can contribute to sustainable development. While significant progress has been made within multiple areas, both in terms of energy harvesting, transport, and utilisation, losses in the form of heat are an inevitable outcome of all energy conversions. Therefore, methods for increasing the efficiency of such processes are likely to be as relevant today as in the foreseeable future, which means that technologies such as thermoelectrics can play a key role in the ongoing transition to a more sustainable society.

1.1 Global energy demand

To understand the urgent need for societal change, combined with technological advances, it is informative to consider the world energy consumption and how it is distributed between different sources, information that is regularly published by the International Energy Agency (IEA). In the report "World Energy Balances: Overview" [2] it is, specifically, stated that the total primary energy supply (TPES) has increased by

a factor of 2.5 between 1971 and 2016, from 7.3 TW yr to 16.3 TW yr[1]. As is shown by the pie charts in Fig. 1.1, the contribution of renewable sources has remained relatively small, at around 13 %, over the last five decades. Even today, the supply is dominated by oil, followed by coal and natural gas.

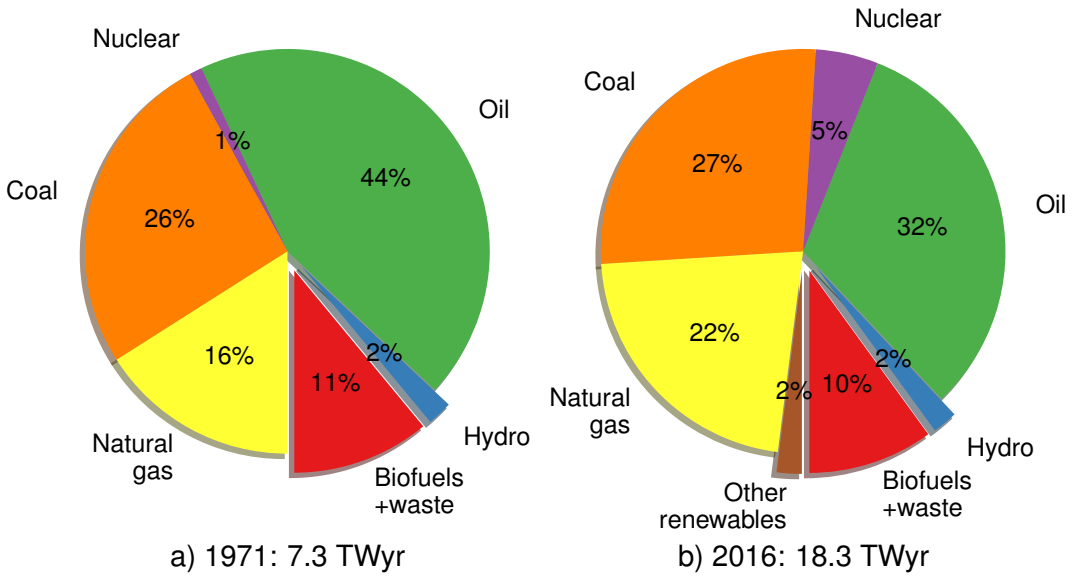

Figure 1.1: Chart showing how the total primary energy supply is distributed between different types of fuels on a global level. The displaced slices correspond to renewable resources. This figure has been created using data from "World Energy Balances: Overview" [2].

Another important problem associated with the energy systems of today are the significant losses that occur throughout the supply chain. This is apparent from Fig. 1.2, which is based on data regarding the energy consumption in the U.S. published annually by the Lawrence Livermore National Laboratory [4]. As can be seen from this diagram, a substantial amount of energy is lost as heat, both when electricity is generated and when a given resource is consumed. In fact, as much as 67 percent of the total energy is wasted. It is, moreover, apparent that the main contributions to the total losses stem from transportation and electricity generation. In fact, the efficiency associated with the latter is 35 percent and the former 21 percent. The percentages for the residential, commercial and industrial sectors are significantly higher, corresponding to 65 %, 65 % and 49 %, respectively. Hence, waste heat recovery has immense potential and is applicable in a wide variety of different contexts. These conclusions are highly relevant for the study at hand since thermoelectric materials, as will be further explained in the following two sections, are useful for converting heat directly into electricity.

[1]The original data, given in tonne oil equivalents, have been converted to TW yr using the information regarding "energy units" provided by the American Physical Society [3].

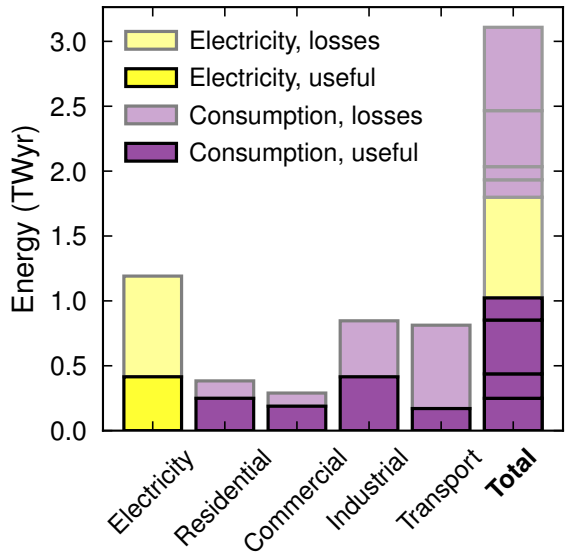

Figure 1.2: Diagrams displaying the production and consumption of energy in the U.S. in 2020. Specifically, the bars show the used and lost energy associated with the electricity generation as well as various consumer sectors. Note that the useful electricity is not included in the total amount, as indicated by the bar colours, since this energy is distributed between the individual consumer groups, and is, hence, included in the corresponding sums. This figure has been created using data from the Lawrence Livermore National Laboratory [4].

1.2 Thermoelectric principles

One of the main driving forces for researching thermoelectric materials is the prospect of developing devices for solid-state power generation. The basic principle for such a generator is illustrated in Fig. 1.3, which shows one of the multiple couples that make up an actual device. Specifically, each of these consists of two "legs", of which one is an n-doped and the other a p-doped semiconductor, connected so as to form a closed circuit. As a result, the temperature difference between the heat source and the heat sink causes a current to flow through the couple, as is depicted in the same figure. Physically, this can be explained by the fact that the electrons at the hot side have higher kinetic energy and, therefore, a greater tendency to migrate compared to those on the cold side. Devices that operate in the reversed fashion are generally referred to as Peltier coolers since these are used to withdraw energy from the cold side by supplying a current.

The maximum efficiency of a thermoelectric power-generator can be estimated using

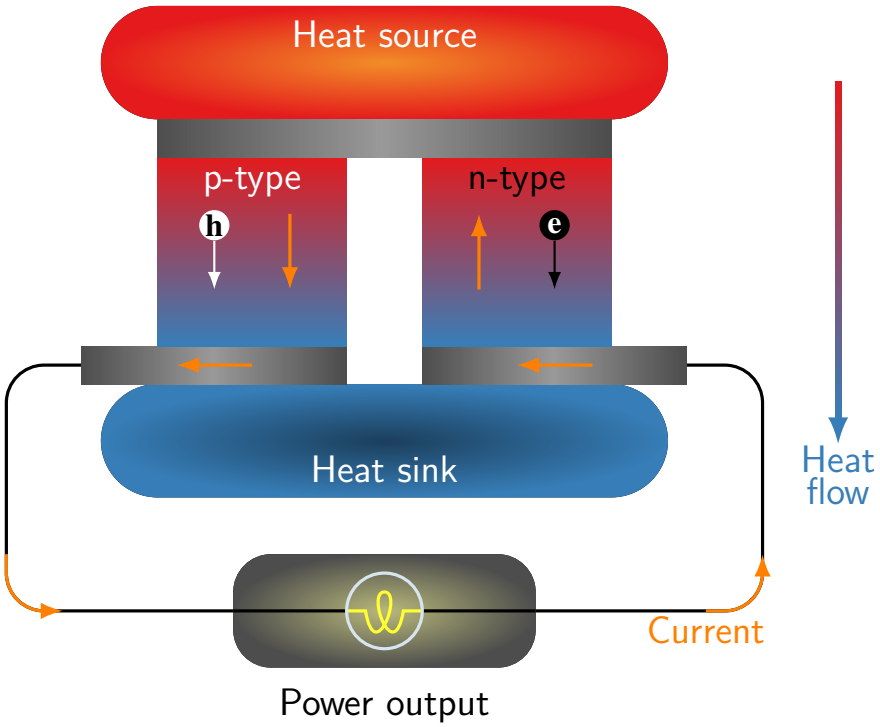

Figure 1.3: Schematic diagram showing the working principle of a thermoelectric generator. The electrons flow in opposite directions in the two legs due to the temperature difference between the heat source and sink, which means that an electric circuit is generated.

the following formula

$$\eta = \underbrace{\frac{T_\mathrm{h} - T_\mathrm{c}}{T_\mathrm{h}}}_{\text{Carnot efficiency}} \frac{\sqrt{1+ZT}-1}{\sqrt{1+ZT}+\frac{T_\mathrm{c}}{T_\mathrm{h}}}, \tag{1.1}$$

where T_h and T_c are the temperatures at the hot and cold sides, respectively, while $T = (T_\mathrm{h} + T_\mathrm{c})/2$ corresponds to their average. As is indicated, the first factor corresponds to the Carnot efficiency. Since this corresponds to the theoretical upper limit for the performance of any heat engine

$$\lim_{ZT\to\infty} \eta = \frac{T_\mathrm{h} - T_\mathrm{c}}{T_\mathrm{h}}. \tag{1.2}$$

which is apparent from Fig. 1.4. Here, Eq. (1.1) has been plotted as a function of T_h, under the assumption that $T_\mathrm{c} = 300\,\mathrm{K}$, for different values of ZT, which corresponds to the figure of merit for a single couple [5]. The latter is related to the physical properties

of the n-type and p-type leg

$$Z = \frac{S_{np}^2}{\left(\sqrt{\frac{\kappa_n}{\sigma_n}} + \sqrt{\frac{\kappa_p}{\sigma_p}}\right)^2}, \tag{1.3}$$

where S_{np} represents the differential Seebeck coefficient between the two materials while σ and κ correspond to the electric and thermal conductivities, respectively. In practice, however, it is often more convenient to consider the material specific figure of merit,

$$zT = \frac{\sigma S^2}{\kappa} T, \tag{1.4}$$

which has been made dimensionless through multiplication with the temperature T. By comparing Eq. (1.3) and Eq. (1.4), it is evident that ZT and zT are equivalent if the two legs have similar material properties, which is often a reasonable assumption.

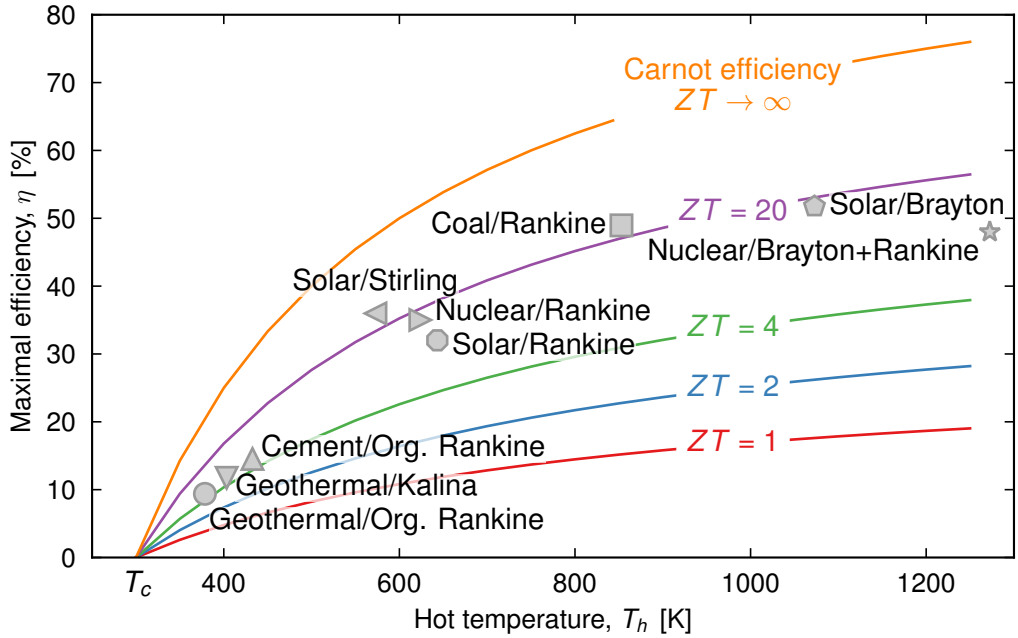

Figure 1.4: Plot of the conversion efficiency for a thermoelectric generator when the temperature at the hot side (T_h) is varied while it is kept fixed on the cold side ($T_\mathrm{c} = 300\,\mathrm{K}$) for various ZT values. The diagram also includes the efficiencies of different mechanical heat engines that are relevant for comparison [6].

A fundamental issue is that all three properties in Eq. (1.4) are interrelated in such a way that there exists an optimal charge carrier concentration at each temperature, as

well as the vice versa, that maximises the zT as shown in Fig. 1.5. Assuming that the bands of a heavily doped (degenerate) semiconductor are parabolic and unaffected by the level of doping, it can be shown that the Seebeck coefficient [7]

$$S = \frac{8\pi^2 k_B}{3q_e h^2} m^* T \left(\frac{\pi}{3n}\right). \tag{1.5}$$

Here, k_B is the Boltzmann constant, q_e the electron charge, h Planck's constant, T the temperature and n the charge carrier concentration. It is crucial to note that the effective mass m^* is related to the effective band mass m_b^*, which depends on the curvature of the bands, and the number of equivalent degenerate valleys N_V via the formula

$$m^* = N_V^{2/3} m_b^*. \tag{1.6}$$

Since the electrical conductivity is directly proportional to the mobility μ and $\mu \propto m_b^{*5/2}$, it can thus be concluded that [8]

$$\sigma = nq_e\mu \propto m_b^{*5/2}. \tag{1.7}$$

Tuning of n and m_b^*, which are two ways of optimising the zT (Sect. 1.4), is consequently not as straightforward as it may first appear. What makes matters even more complicated is that the electronic part κ_e of the thermal conductivity $\kappa = \kappa_e + \kappa_l$, which also includes a contribution from lattice vibrations (phonons) κ_l, is directly related to the electrical conductivity σ. This is especially apparent from the Wiedemann-Franz law (Sect. 3.3.3) [9],

$$\kappa_e = L\sigma T = \{Eq.\ (1.7)\} = Lnq_e\mu T, \tag{1.8}$$

where L is the so called Lorenz number.

The fact that large S are typical for semiconductors while metals have high σ and glasses low κ can be seen as an indicator that identifying candidate materials for thermoelectric applications is not an easy task [7]. Indeed, overcoming interdependencies of the properties that determine the figure of merit is one of the most fundamental and challenging issues facing the thermoelectric research community. The fact that this only applies to S, σ, and κ_e, however, means that two basic strategies can be identified: optimisation of the electronic properties, so as to achieve a high power factor, σS^2, and minimisation of the lattice thermal conductivity, κ_l [12]. Another practical issue revealed by Fig. 1.5 is that a given thermoelectric material only has a decent efficiency in an interval around the temperature at which the zT reaches a maximum. As a consequence, different materials need to be employed depending on the temperature range and, thus, the application.

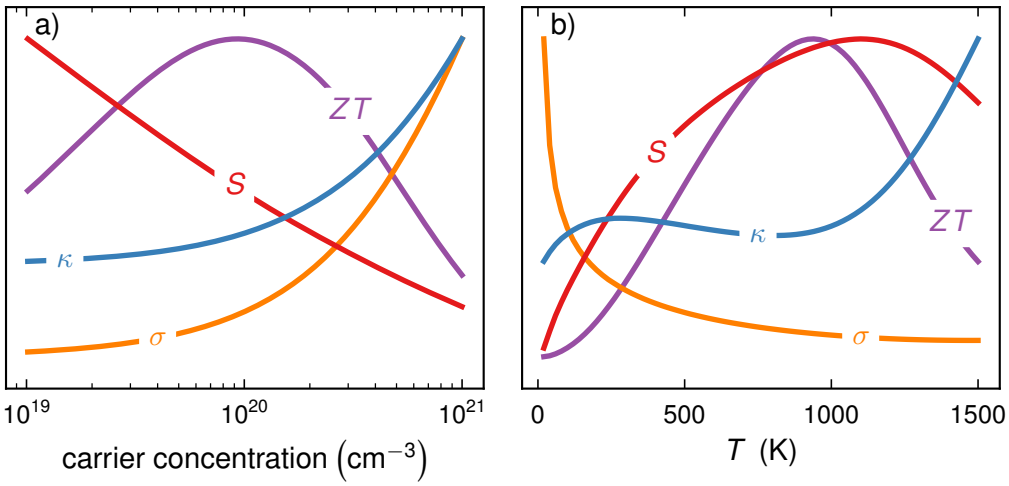

Figure 1.5: Diagrams showing the dependencies of the physical properties that determine the efficiency of a thermoelectric material, namely the Seebeck coefficient (S) as well as the electric and thermal conductivities (σ, κ) as functions of (a) the carrier concentration and (b) the temperature. These results have been calculated via BTT (Sect. 3.3.6), as implemented in the BoltzTraP2 software [10], using a ground state $Ba_8Ga_{16}Ge_{30}$ structure. In addition, it has been assumed that the lattice contribution is constant ($1\,\mathrm{W\,m^{-1}\,K}$) while the relaxation time is given by $\tau = 15\,\mathrm{fs} \times (T/300\,\mathrm{K})^{1/2}$ [11].

1.3 History of thermoelectric research

Though the concept of thermoelectrics is relatively unknown to the average consumer, the underlying phenomena were discovered and conceptualised already during the second half of the 19$^{\text{th}}$ century thanks to the pioneering work by Seebeck, Peltier and Thomson [13]. Specifically, in 1821 J. T. Seebeck discovered that a voltage V is produced if a pair of dissimilar conductors, which are connected electrically in series and thermally in parallel, are subjected to a temperature difference, ΔT. Twelve years later, J. Peltier showed that the opposite is also true, namely that when a current is supplied to such a couple, heat is absorbed at one junction and produced at the other. The connection between these two effects remained unknown until 1851 when W. Thomson was able to derive the formula for their interrelationship based on thermodynamic arguments. In addition, he predicted that a small amount of heat is generated, reversibly, when a current passes through a conductor that is, simultaneously, subjected to a temperature difference, which is referred to as the Thomson effect.

Though the Seebeck effect was used for several years to measure temperature and detect thermal radiation, the next big leap forward came in 1911 when Altenkirch provided a theoretical framework for explaining thermoelectic generation and cooling [13]. He also introduced the thermoelectric figure of merit by noting that good thermoelec-

tric materials need to have high Seebeck coefficients and electrical conductivities together with low thermal conductivities. Unfortunately, the materials available at the time were not sufficiently efficient to be of practical use. Consequently, it was not until the late 1930s that thermoelectric research begin to surge forward once more, due to the development of semiconducting materials. For instance, Telkes constructed a working generator with a 5 % efficiency already in 1947. Soon thereafter Ioffe made a number of important contributions, which included a theoretical description of semiconducting thermoelements, in 1949, as well as the discovery that isomorphus alloying could significantly improve the zT in 1956. In addition, Goldsmid and Douglas were able to show that thermoelectric refrigeration systems could be used to reach temperatures below 0 °C.

The fast development of novel semiconductors for other applications in the middle of the 20$^{\text{th}}$ century facilitated the discovery of multiple promising candidates for thermoelectric applications. The flurry of detailed surveys that were undertaken during this era resulted in the identification of several materials with zT values reaching as high as 1.5 [13]. The alloying concept introduced by Ioffe is deemed to have been very important for this development since many of the top performing thermoelectric materials take the form of mixed-crystal semiconductors [14]. In particular, he was able to show that the reduction of the thermal conductivity exceeds the deterioration of the electrical conductivity when alloying known thermoelectric materials, including Bi_2Te_3, PbTe and Ge, with 20 % to 30 % of an additional element. The progress during the following three decades was very slow, since no appreciable improvement in the zT values were achieved [15]. Although the international research community showed little interest for this field during this period, the industry continued to grow.

In the beginning of the 1990ies the US Department of Defence launched a successful initiative to stimulate thermoelectric research [15]. As a result, two different venues for finding new thermoelectric materials were found, based on the results in a number of key theoretical papers, which came to inspire a resurgence of interest for thermoelectric research that has subsequently led to several major breakthroughs during the last three decades. Firstly, in 1993 the potential of low-dimensional systems was identified by Dresselhaus and co-workers [16, 17], who showed that remarkable improvements of the zT could be achieved through quantum confinement. Two years later, Slack [14] introduced the PGEC concept together with a number of selection criteria. In particular, an ideal structure should be such that the phonons are effectively scattered as in a glass, while the electrons are not, which is typically the case for crystalline materials [18]. He, moreover, suggested that inorganic compounds with host-guest structures ought to possess such traits and several groups of promising thermoelectric materials were indeed discovered based on these criteria [14]. Another concept that have aided the search for the materials with improved thermolelectric properties was formulated by Mahan and Sofo [19] in 1996. More precisely, they provided evidence that such materials should, optimally, have a sharp peak in the electronic density of states near

the fermi level.

1.4 Enhancing the thermoelectric properties

As can be gathered from the expression in Eq. (1.4), the thermoelectric performance can be enhanced by either lowering the thermal conductivity or increasing the power factor. These goals can, in turn, be achieved by exploiting the fact that electrons and phonons are generally scattered most effectively by structural features with length scales similar to their respective wavelengths [8]. Since these are often longer for phonons than electrons, it should be possible to minimise the lattice thermal conductivity, while leaving the electrical properties unaffected or even enhancing them [7, 8]. In fact, it is possible to identify two alternative strategies for realising this concept: controlling the material on an atomic level, which, for instance, includes alloying; defect engineering; and exploiting phase transformations, or engineering the nano-, meso- and microstructure.

Novel approaches have, in recent times, begun to emerge that combine the benefits of quantum confinement and the PGEC concept [15]. This has led to the development of new types of bulk thermoelectrics, which are either nanostructured or contain nanoinclusions, with significantly improved zT values. As explained in multiple reviews [7, 8, 12, 18, 20–24], it is possible to identify a number of key concepts for enhancing thermoelectric properties that have proven to be particularly successful. A selection of these deemed to be the most relevant for the project at hand, are briefly outlined below. In addition, their relationship to the two alternative strategies and goals mentioned earlier are illustrated in Fig. 1.6.

- The most fundamental approach for maximising the thermoelectric figure of merit is, as eluded to earlier, to find the optimal carrier concentration. Historically, this has most often been achieved through **conventional doping**, which involves either adding extrinsic dopants or controlling the density of intrinsic defects. For certain materials, such as inorganic clathrates, it is possible to tune the carrier concentration by carefully changing the composition [25]. More advanced approaches include **graded or temperature-dependent doping** [7, 24]. The former is based on the idea that an optimal performance would be achieved if the legs that make up the thermoelectric generator consist of multiple layers, each of which has a maximum zT for the temperature at the corresponding position. Numerous studies have, however, revealed that this concept suffers from significant drawbacks, mainly because the concentration gradients have a tendency to become homogenised over time via interlayer diffusion [7, 24]. By contrast, the more recently conceived T-dependent doping has been successfully implemented for a variety of composites. This strategy relies on the temperature dependent sol-

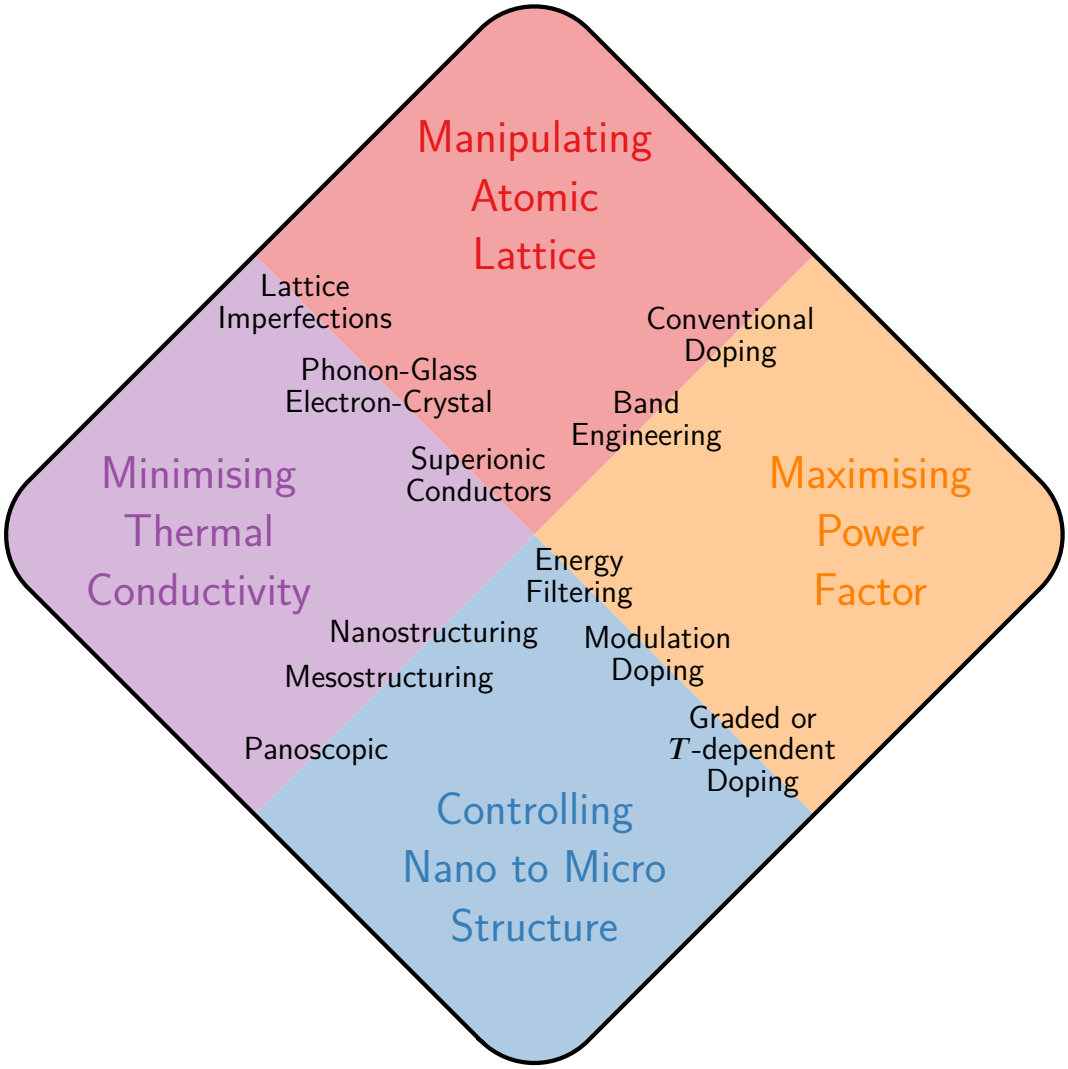

Figure 1.6: Illustration of various concepts for enhancing thermoelectric performance, which aim to reduce the thermal conductivity or boost the power factor by manipulating the structure on the atomic level or the nano- to microscale.

ubility of one phase in the other, which, for a suitably selected pair of materials, makes the doping level increase with temperature [26].

- By suitably tuning the band structure it is possible to enhance the Seebeck coefficient, specifically, by increasing the effective carrier mass, m^* (Eq. (1.5)) [7, 8, 19, 24]. As indicated by Eq. (1.6), this can be achieved by enhancing either the band effective mass, m_b^*, or the number of band extrema N_V. In particular, m_b^* can be increased by flattening the bands or introducing resonant levels. Though N_V

can be enhanced through band convergence, it also tends to be large for highly symmetric structures. At the same time, it is possible to adjust the band gap and, thereby, shift the excitation temperature for the minority charge carriers, above which the Seebeck coefficient decreases while the thermal conductivity increases because of bipolar diffusion [7, 8]. In spite of the fact that this approach leads to a lower electrical conductivity, see Eq. (1.7), it has been proven to yield significant improvements of the zT for various systems.

- At the atomic level, increased phonon scattering can be achieved through the introduction of **lattice imperfections**, which can either be in the form of foreign elements or vacancies [7, 8, 24]. While this is a natural consequence of doping, even greater effects can be achieved through cross-substitution, which is not as restrictive since each element is replaced by a pair of species that has been chosen so as to maintain the charge balance of the compound.

- The benefits of restricting the dimensions of thermoelectric materials were, as was mentioned in the previous subsection, recognised already in the beginning of the 1990ies, when it was predicted that quantum confinement could lead to an exceptionally low lattice thermal conductivity. Though progress has been made in the development of such low-dimensional nanomaterials, in the form of quantum dots, nanowires and thin films, the very high zT value predicted by theory have yet to be demonstrated. An alternative approach for reducing the lattice contribution to heat transport is to enhance phonon scattering, which is the main idea behind the concept of **nanostructured** bulk materials [7, 8, 22, 27–30]. It has moreover been demonstrated that an even lower thermal conductivity can be achieved through the introduction of **mesostructures**, which can scatter the phonons with long wavelengths. Based on the same logic, one would imagine to hinder propagating lattice modes across the entire spectrum by fabricating materials that include atomic, mesoscopic, and nanoscale features, which is sometimes referred to as a **panoscopic** approach (or "all-scale hierarchical architecture") [7, 22, 28–31].

- It has been shown that **energy filtering**, which effectively removes low-energy, or minority, carriers, can be achieved in nanostructured materials, given that a suitable band offset exists between the host and guest phases [7, 8, 24]. Although this may have a slight deteriorating effect on the electrical conductivity, the significant enhancement of the Seebeck coefficient leads to a larger power factor. In addition, it is possible to increase the former, without significantly affecting the latter, through modulation doping. This approach, while well established in the context of developing devices for microelectronic and phononic applications, has only sparingly been applied to bulk thermoelectric materials [32]. It is based on the idea that in a composite made up of a matrix and a doped phase, charge

carriers can spill over from the latter into the former, provided that the band structures are properly aligned. Because the matrix phase will contain significantly fewer point defects, this should lead to an enhancement of the mobility, and thus also the power factor, compared to a conventionally doped material with the same, effective, carrier concentration.

- The previously mentioned **PGEC** concept has strongly influenced the search for new thermoelectric materials during the last three decades and has enable the (re-)discovery of several classes that exhibit intrinsically low thermal conductivities and relatively high power factors. This includes inorganic clathrates, which will be further discussed in the next chapter [18].

- **Superionic conductors** can be viewed as an extended version of the PGEC concept and are sometimes also referred to as "phonon-liquid electron-crystal" materials [7, 8]. Key representatives include compounds in which anions form a well-defined crystal structure while the cations are completely disordered and possess superionic mobilities. Due to this liquid-like behaviour, the phonons are strongly scattered, which leads to extremely low lattice thermal conductivities.

2

Inorganic Clathrates

Since being discovered in the 1960ies inorganic clathrates have fascinated and intrigued the scientific community because of their complex crystal structure and physical properties [33–36]. Their usefulness for thermoelectric applications was recognised during the 1990ies when it was hypothesised, and later proven, that semiconducting materials with host-guest structures could be potential realisations of the PGEC concept, as already mentioned in Chap. 1 [14]. The most relevant and well-studied clathrates consist of alkaline or alkaline earth "guest" atoms that are trapped inside a "host" framework, made up of elements from groups 13 and 14 of the periodic table [35, 36]. Over the years, however, a multitude of different variants have been discovered that either incorporate other types of guest or host atoms, such as rare earth elements in the former case and transition metals as well as elements from the nitrogen family (pnycogens) in the latter. In addition, there exists a subgroup commonly referred to as inverse clathrates, with reversed host-guest polarity, in which the guests are commonly halogens while the framework elements belong to group 14 as well as 15, 16 or 17 [37].

Though there exist nine different archetypal structures, which are referred to by roman numerals, most inorganic clathrates discovered so far have been classified as type I. A small number belong to group II, VIII and IX while type III and VII are even less common [36]. The focus of this thesis, however, are type I clathrates, for which the chemical formula can be written as $A_8B_xC_{46-x}$ where A represents the guest while B and C are host atoms. The corresponding structural motif, which belongs to space group $Pm\bar{3}n$ (International Tables of Crystallography A number 223), is illustrated in Fig. 2.1, from which it is apparent that the framework is made up of two types of cages, namely pentagonal dodecahedra and tetrakaidecahedra, each of which contains a single guest atom. It is commonly assumed that the latter is located at the cage centres, which correspond to the 6*d* and 2*a* Wyckoff positions, respectively. The 46 host atoms, meanwhile, are distributed between the 6*c*, 16*i*, and 24*k* sites.

Both experimental [38–57] and theoretical [58–60] studies indicate that the guests tend to be displaced from the 6*d* but not the 2*a* sites. The magnitude of the displacement has been shown to depend on a number of factors, including the size of the guest species compared to the cage [40–42, 45, 47, 49, 50, 54] and the configuration of the framework [44, 46, 48, 53, 56, 60]. Though even the earliest studies of $Sr_8Ga_xGe_{46-x}$ and $Eu_8Ga_xGe_{46-x}$ established that the Sr and Eu atoms should be modelled as being split between the four 24*i* or 24*j* sites located within each of the large cages, [38–42], it has later been discovered that this is neither a unique nor a universal feature for these systems. For instance, it was later discovered that the same applies for β-$Ba_8Ga_xSn_{46-x}$ [47, 61]. In addition, the off-centre distance has been found to vary with Ga content $Sr_8Ga_xGe_{46-x}$ [56], be more significant for p-type than n-type $Ba_8Ga_{16}Ge_{30}$ [46], and increase with temperature for the quasi-on-centre systems $Ba_8Al_{16}Ge_{30}$ [48] and $Ba_8Ga_{16}Si_{30}$ [43].

As explained in Sect. 1.4, the optimisation of any thermoelectric materials generally involves measures aimed at enhancing the electronic transport properties and/or minimising the lattice thermal conductivity. For inorganic clathrates, it is possible to identify three fundamental problems that have served as the foundation for most studies of this group of materials conducted so far. Since the same is true for this PhD project, these three questions, which are listed below, will serve as points of departure not only in the presentation below but also when discussing the methodologies and scientific results in the following chapters.

- Why is the lattice thermal conductivity intrinsically low?
- What is the impact of chemical ordering on the physical properties?
- How can the electronic transport be optimised?

2.1 Phonon transport

The inherently low thermal conductivity is one of the foremost qualities that makes clathrates attractive for thermoelectric applications. Though it is therefore not surprising that this property has been the focus of intense research, it has also been the subject of a great deal of controversy since there exist several alternative hypotheses regarding its origin. Already in the pioneering studies of this group of materials, it became evident that there was a strong correlation between the thermal transport and the displacement of the guest atom. For instance, the low temperature thermal conductivity shows a plateau, similar to glasses, in both $Eu_8Ga_xGe_{46-x}$ and $Sr_8Ga_xGe_{46-x}$ [40, 62, 63] and a crystalline peak in n-type $Ba_8Ga_xGe_{46-x}$, for which the Ba atoms are approximately on-centre [44]. The displacement is, however, more pronounced in the p-type version of the latter material, which possesses a glass-like lattice thermal conductivity [44]. It

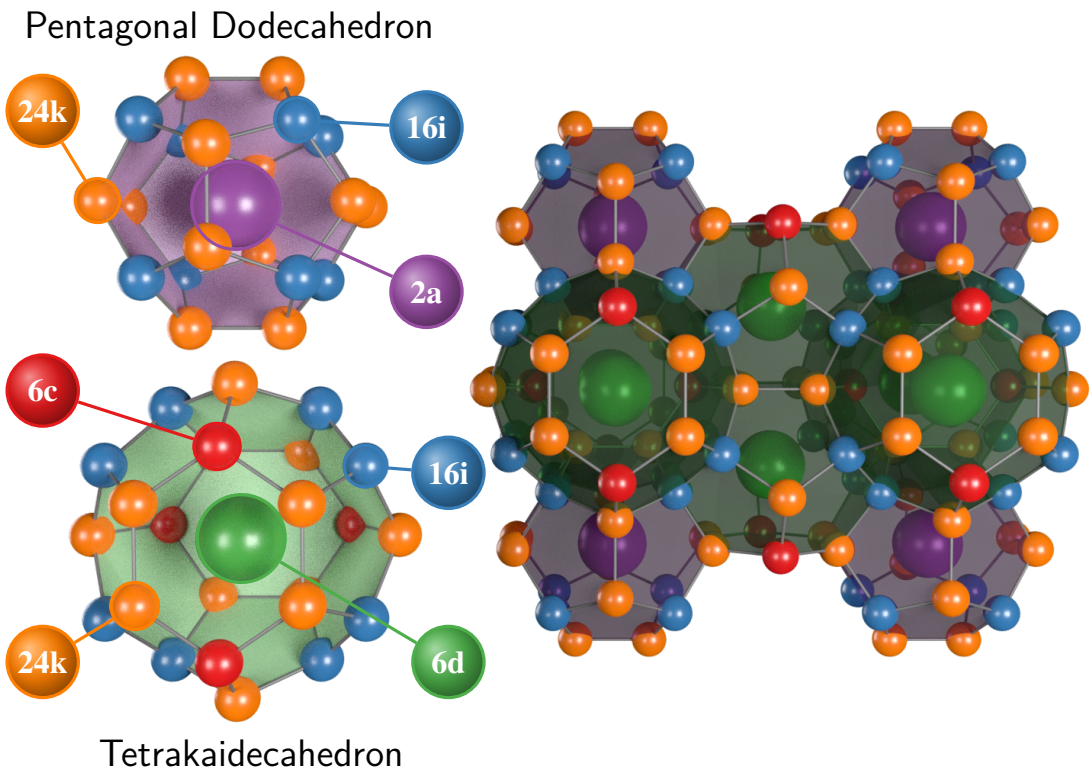

Figure 2.1: Illustration of the type I clathrate structure, including views of the large tetrakaidecahedral and small pentagonal dodecahedral cages. Specifically, these encapsulate the 6*d* (green) and 2*a* (purple) guest positions and form part of the host framework, which is made up of 6*c* (red), 16*i* (blue), and 24*k* (orange) Wyckoff sites.

has furthermore been discovered that the thermal conductivity can be tuned, from glass-like to crystalline, by altering not only the Ge/Si ratio in $Sr_8Ga_{16}Si_xGe_{46-x}$ [49] but also the Ga content in $Sr_8Ga_xGe_{46-x}$ [56] as well as $Ba_8Ga_{16}Ge_{30}$ and β-$Ba_8Ga_{16}Sn_{30}$ [47]. In this context, it is interesting to note that the tin based clathrate β-$Ba_8Ga_xSn_{46-x}$ typically exhibits a lower lattice thermal conductivity than, for instance, $Ba_8Ga_xGe_{46-x}$ [47]. While this can partly be explained by the greater mass of Sn, compared to Ge, there is significant evidence that this is also related to the dynamics of the off-centred Ba atom at the 6*d* site, which exhibits a behaviour very similar to Sr in $Sr_8Ga_xGe_{46-x}$ and Eu in $Eu_8Ga_xGe_{46-x}$ [52].

Initially, it was argued that the source of the low thermal conductivity was related to a combination of resonant scattering of phonons by the large amplitude localised vibrations, or "rattling motion", of the guest atoms within the large cages together with their "tunneling" between equivalent sites [40, 63, 64]. The relevance of the latter mechanism

came in doubt, however, when it was discovered that there is a glass-like plateau in the low-temperature thermal conductivity of p-type $Ba_8Ga_xGe_{46-x}$ even though the disorder of the guest atom was similar to n-type $Ba_8Ga_xGe_{46-x}$, which by contrast displays a crystalline peak [44, 46]. Instead, it was suggested that the low κ_l was due to extensive charge-carrier scattering. It has later been concluded, based on a thorough investigation of the structural, electrical and thermal properties for a set of $Sr_8Ga_xGe_{46-x}$ compounds, that neither of these explanations are satisfactory [56]. The need for a better understanding of the underlying phenomena and, especially, more accurate calculations was stressed Lory *et al.* [65], who was able to accurately measure the phonon lifetimes in $Ba_{7.81}Ge_{40.67}Au_{5.33}$. In particular, they found that the heat was mainly carried by low-energy acoustic modes with very long mean-free-paths.

New insights regarding the interrelation between thermal transport and the lattice dynamics have, however, been gained thanks to a number of recent computational studies. For instance, it has been shown that a key difference between the on- and off-centre systems $Ba_8Ga_xGe_{46-x}$ and $Ba_8Ga_xSn_{46-x}$, respectively, is that the heat carrying acoustic phonons correspond to extended modes in the former while they are localised, above a certain frequency, in the latter [66]. In addition, this phenomenon appears to be linked to the onset of the plateau in the lattice thermal conductivity. By using Ba_8Si_{46} and the unfilled clathrate Si_{46}, Chen *et al.* [67] could moreover reveal that the presence of the guest atoms is essential for inhibiting thermal transport. Tadano *et al.* [68, 69] came to similar conclusions based on their study of $Ba_8Ga_{16}Ge_{30}$, thus confirming that the weak interactions between host and guest atoms give rise to low frequency modes that couple with the acoustic branches of the framework, thereby introducing an avoided crossing, as illustrated in Fig. 2.2. Interestingly, this not only flattens the latter, which reduces the group velocities, but also suppresses the phonon lifetimes by both shifting the acoustic phonons to lower frequencies and introducing resonant scattering in the vicinity of the hybridised modes. The complexity of this phenomenon is emphasised by Ikeda *et al.* [70] who, based on a combined experimental and computational study of $Ba_8Cu_{4.8}Ge_{41.2-x-y}\square_yGa_x$, have proposed that this is caused by a Kondo-like effect. Not only does this idea confer a new perspective on the phononic heat transport of inorganic clathrates, it also has practical implications. Specifically, the Kondo description implies that the lattice thermal conductivity could be further reduced in systems with small Einstein temperatures (Sect. 3.1.6), even beyond the widely accepted theoretical minimum, for disordered solids, defined by Cahill *et al.* [71]. Taken together, these computational results confirms earlier experimental [72] and theoretical [59] evidence for the importance of phonon-phonon coupling. Crucial insights have, thus, been gained regarding the low temperature lattice thermal conductivity, even though it is, for instance, not yet known why such contrasting behaviour is displayed by n- and p-type compounds. Although the thermal transport of clathrates above $\sim 100\,\mathrm{K}$ has generally received less attention, Xi *et al.* [73] have recently discovered that the experimentally observed saturation of the thermal conductivity for off-centre systems within this tem-

perature regime is correctly predicted if host-guest interactions are taken into account.

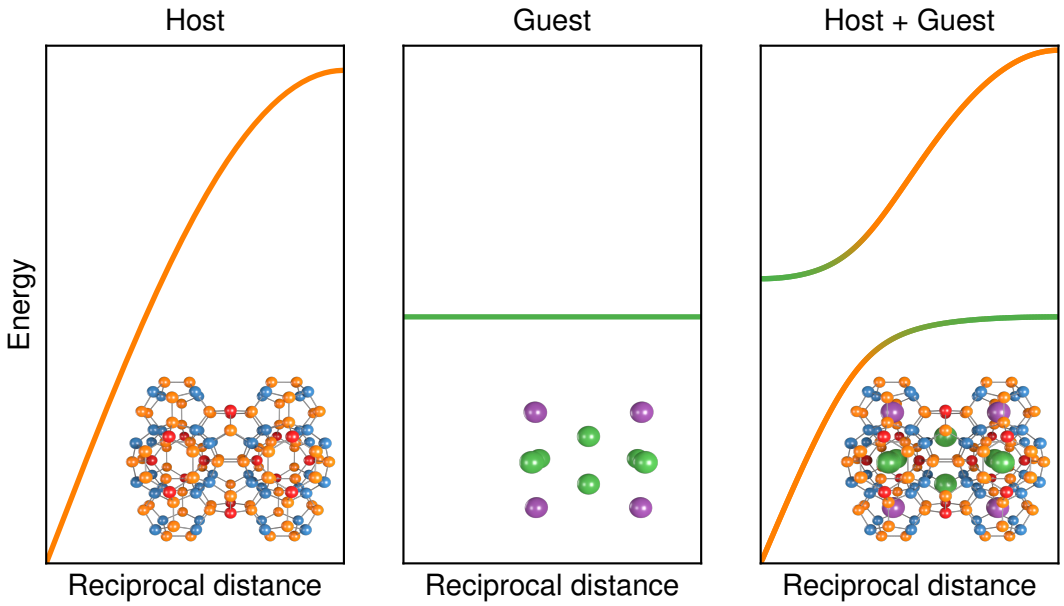

Figure 2.2: Schematic illustration of the hybridisation of host and guest modes, leading to an avoided-crossing in the phonon dispersion. Formally, the former (*left*) can be modelled as a linear chain of atoms (Sect. 3.1.5) and the latter (*middle*) as an Einstein oscillator (Sect. 3.1.6). Christensen *et al.* [72] have shown that the dynamics of the combined system (*right*) can be captured using a classical spring model with two interconnected subsystems, corresponding to the guest atom and the surrounding cage.

2.2 Chemical ordering

In spite of the fact that even the earliest crystallographic studies of $Ba_8Ga_{16}Ge_{30}$ and $Sr_8Ga_{16}Ge_{30}$ [38] suggested that the distribution of the host elements in inorganic clathrates is not random, it took several years before this became an established fact [48, 74]. This can partly be explained by the similarities in the X-ray, and to some extent even neutron, scattering cross sections for a few of the key elements, especially Ga/Ge and, to a lesser degree, Al/Si. Another reason, was that many studies focused on the guest atoms and, therefore, largely ignored the host framework. A pioneering work in this context is the detailed investigation of $Ba_8Al_{16}Ge_{30}$ performed by Christensen *et al.* [48], who employed a combination of synchrotron X-ray and neutron diffraction to determine the SOFs for multiple samples, synthesised via different methods. They were, moreover, able to show that their observations followed a set of rules that could

be formulated based on the notion that bonds between trivalent elements are generally unfavourable:

1. SOF(trivalent@6c) $\leq$ 100 %
2. SOF(trivalent@16i) $\leq$ 50 %
3. SOF(trivalent@24k) $\leq$ 50 %
4. SOF(trivalent@6c) + SOF(trivalent, 24k) $\leq$ 100 %
5. SOF(trivalent@16i) + SOF(trivalent, 24k) $\leq$ 50 %

It was later confirmed that the above constraints also agree very well with previously reported experimental data for a number of other clathrate systems [74]. To understand their physical origin, however, one must consider the local chemical environments of the atoms that make up the host framework. As is illustrated in Fig. 2.3, the 6c sites are unique in the sense that they are only connected to 16i and 24k sites, which explains why 100 % occupation is allowed (rule 1). Since both of the latter have one other site of the same type as a nearest neighbour, only half of them can be occupied by trivalent elements (rules 2 and 3). The last two rules (4 and 5) meanwhile result from the fact that each 24k site is connected to one 6c and two 16i sites.

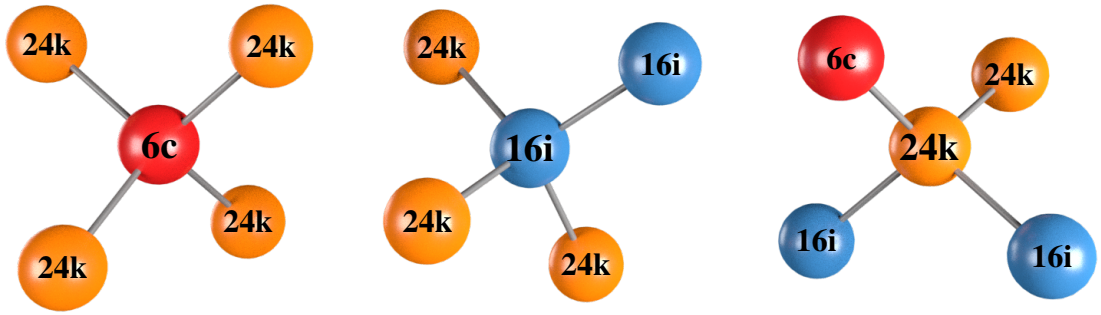

Figure 2.3: Illustration of the local chemical environment around the host sites 6c (red), 16i (blue), and 24k (orange).

The set of empirical guidelines listed above were more recently verified by atomic scale simulations using an approach based on DFT calculations, alloy CEs, and MC simulations, which will be further detailed in Sect. 3.2 [11, 60, 75]. These studies can be regarded as a major breakthrough since it is impossible to effectively sample the

configuration space, which is vast even for a pseudo-binary[1] clathrate[2] using DFT calculations directly. Crucially, the calculated SOFs were shown to give excellent agreement with the experimental data for $Ba_8Ga_xGe_{46-x}$, $Ba_8Ga_xSi_{46-x}$, $Ba_8Al_xGe_{46-x}$, and $Ba_8Al_xSi_{46-x}$, thereby demonstrating the predictive power of this approach [60]. What these calculations also show is that the strengths of the pair interactions between the host species are fundamental for understanding the temperature and composition dependence of the SOFs. From these results, one can conclude that the rules specified earlier are in fact not sufficient to describe the predicted and measured variations [60, 75]. For instance, these studies show that the interactions between pairs of Al atoms are more unfavourable then those between Ga atoms, which is reflected by the SOFs. It should also be emphasised that the computational methodology outlined above is not limited to predicting the chemical ordering. As has been demonstrated for $Ba_8Ga_{16}Ge_{30}$ [11], the same approach combined with BTT calculations can be used to identify the atomic arrangement that corresponds to the most optimal band structure and thus maximises the PF.

A key conclusion that can be drawn from the results presented earlier is that the clathrate phase should become less stable as the content of trivalent elements increases. This could, for instance, be the reason why the solubility limit seems to be less than, or close to, Al/Ga $= 16$ for several clathrate systems, such as $Ba_8Ga_xGe_{46-x}$ [76]; $Ba_8Ga_xSi_{46-x}$ [77]; $Ba_8Al_xGe_{46-x}$ [78]; and $Ba_8Al_xSi_{46-x}$ [79]. Together with the fact that compositions that are close to charge-balanced are the most likely to show a good thermoelectric performance, this partly explains why $Ba_8Ga_xGe_{46-x}$, for which p-type samples with $x > 16$ have been successfully synthesised [46], generally displays a significantly higher performance than, for example, $Ba_8Al_xSi_{46-x}$ [79–82]. It is moreover interesting to note that chemical disorder might have an impact on not only the electronic but also the heat transport. For instance, the previously mentioned study of *n*-type and *p*-type $Ba_8Ga_xGe_{46-x}$ by Christensen *et al.* [46] was actually based on single crystals that had been prepared using different methods, namely Czochralski-pulling and flux-growth, respectively. Their results furthermore reveal that the SOF at the 6*c* site is significantly lower for the *p*-type ($\sim 60\,\%$) compared to the *n*-type ($\sim 74\,\%$). Since the former value is closer to the occupation expected for a completely random distribution ($16/46 \approx 35\,\%$), this suggests that the flux-grown sample is more disordered. It is hence not unreasonable to hypothesise that the chemical ordering on

[1] Although a clathrate that includes one guest and two host elements is a ternary chemical compound, the fact that the guest and the hosts reside on different sublattices means that the system is effectively pseudo-binary from a chemical ordering perspective, which is for instance relevant when constructing an alloy CE. For the sake of clarity, the term "pseudo-binary" will be used in all such cases while $Ba_8Al_xGa_yGe_{46-x-y}$ or $Ba_8Ga_xGe_ySi_{46-x-y}$ will be referred to as pseudo-ternaries.

[2] For a general type I clathrate, $A_8B_xC_{46-x}$, with $x = 16$ there are $46!/(30!16!) \approx 10^{12}$ ways to select the 16 sites occupied by B atoms, which is reduced by about a factor of 10 if symmetry is taken into account [60].

the host site might help determine the lattice thermal conductivity, in part by affecting the off-centring of the guest atom in the large cage.

2.3 Performance optimisation

The electronic structure of clathrate compounds is commonly described with help of the Zintl concept [36, 83]. The latter states that the cations, in this case the guests, donate their electrons to the anionic sublattice, which corresponds to the host framework, to enable all of the atoms to obtain a full octet. Taking $Ba_8Ga_{16}Ge_{30}$ as an example, each Ba atom must relinquish a pair of electrons to reach a noble gas configuration. Given that the type I framework consists of 46 tetrahedrally bonded atoms, this means that a total of 184 electrons are required to ensure that the octet rule is satisfied. In order to compensate for the surplus provided by the Ba guests, 16 of the tetravalent hosts (Ge) must be replaced with a trivalent element (Ga) in order to end up with a charge balanced compound. While one should therefore expect that such materials should be intrinsic (charge balanced) semiconductors, the samples obtained in practice typically deviate from the nominal stoichiometric composition (Ga $=$ 16). This leads to an intrinsic doping effect, resulting in p-type (Ga $>$ 16) or n-type (Ga $<$ 16) behaviour. Since the lattice parameter for $Ba_8Ga_{16}Ge_{30}$ is about 10 Å, one can estimate that replacement of one Ge atom with Ga increases the number of free electrons by $1/(10\,\text{Å})^3 \approx 10^{21}\,\text{cm}^{-3}$. Given that high-performance thermoelectric materials typically have a charge carrier concentration between $10^{19}\,\text{cm}^{-3}$ and $10^{21}\,\text{cm}^{-3}$ [83, 84], type I clathrates with between 15 and 17 trivalent elements per unit cell are likely to be of practical interest.

Based on the arguments presented above, it might appear that the optimisation of thermoelectric clathrates is relatively straightforward, since it is, in principle, not necessary to introduce any extrinsic dopants. As indicated by numerous studies, synthesising a clathrate compound with a specific composition is, however, not as easy as it may seem [25, 77, 79–82, 85–92]. This helps explain why the attempts at achieving an optimal performance via intrinsic doping have had mixed success, especially given the fact that even slight deviations in the number of trivalent atoms, as mentioned earlier, lead to significant changes in the charge carrier concentration. Moreover, substantial discrepancies in the property measurements are often observed for samples that have the same nominal composition. Not only is this effect even more pronounced when the products of alternative synthesis methods are compared, it actually gives rise to significant differences in the atomic structure, for the reasons discussed in the previous subsection [48, 74].

From a thermodynamic perspective, one would expect that the addition of a third framework species should lead to more stable systems, due to the favourable entropic contribution, which is fundamental for the formation of high-entropy alloys [93–95]. At the same time, the extra element will increase the number of possible secondary

phases, which is already quite large for most of the relevant ternary systems, thereby further complicating the synthesis procedure [96]. This is known to be the case for high-entropy alloys, since many such materials that have been presumed to be single-phase, because they are made up of five or more components with almost equal proportions [93], are in fact multi-phase [97]. There are, however, a few intriguing studies of quarternary clathrates indicating that the addition of a fourth element can indeed stabilise the clathrate phase. An interesting example is $Sr_8Al_xGa_{16-x}Si_{30}$, which has been shown to crystallise in clathrate type I and VIII structures for $0 \leq x \leq 7$ and $8 \leq x \leq 13$ [98, 99]. By contrast, the maximum Ga content in $Sr_8Ga_xSi_{46-x}$ that has been reported so far is $x = 13.82$ [100] while $Sr_8Al_xSi_{46-x}$ is only stable within a narrow interval around $x = 10$ [101]. The situation is similar for $Ba_8Al_xGa_ySi_{46-x-y}$ since samples with a total content of trivalent atoms as high as 16.8 have been synthesised [102], which is well above the presumed solubility limits ($x \lesssim 15$) of both Al in $Ba_8Al_xSi_{46-x}$ [79–81] and Ga in $Ba_8Ga_xSi_{46-x}$ [77]. It should, in other words, be possible to obtain almost charged-balanced $Ba_8Al_xGa_ySi_{46-x-y}$ ($x+y \approx 16$) with thermoelectric properties that ought to be superior to those reported for $Ba_8Al_xSi_{46-x}$ [79–82] and $Ba_8Ga_xSi_{46-x}$ [77], because the latter typically have too high carrier concentrations due to the low content of trivalent elements.

In spite of the previously described problems, there have been efforts to try to enhance the thermoelectric performance of inorganic clathrates by utilising some of the concepts that were outlined in Sect. 1.4 [36, 84]. Various nanomaterials have, for instance, been synthesised, including $Ba_8Ga_{16}Ge_{30}$ thin films [103, 104], nanostructured $Ba_8Ga_{16}Si_{30}$ [105] and $Ba_8Cu_5Si_xGe_{35-x}$ [106] prepared via a combination of planetary ball milling and pressure assisted sintering, sintered $Ba_8Ga_{16}Ge_{30}$ nanoparticles [107], melt-spun $Ba_8Au_xSi_{46-x}$, $Ba_8Ga_{16}Ge_{30}$, and $Ba_8Cu_5Si_6Ge_{35-x}Sn_x$ [106] as well as nanocomposites made up of $Ba_8Ga_{16}Ge_{30}$-$EuTiO_{3-\delta}$ [106], $Ba_8Cu_{4.8}Si_{41.2}$-SiC [106], and $Ba_8Ga_{16}Ge_{30}$-TiO_2 [108]. There have also been attempts at producing functionally graded clathrates, specifically in the form of $Ba_8Ga_{16}Si_xGe_{30-x}$ [109] as well as $Ba_8Au_xSi_{46-x}$ [110, 111]. A more common method, which has been successfully applied to, among others, $Ba_8Ga_{16}Ge_{30}$ [84, 112], is to replace some of the host atoms with elements that belong to groups other than 13 and 14, such as transition metals. As explained in Sect. 1.4, the basic idea is to introduce ionised impurities and point defects that scatter respectively carriers and phonons, thereby enhancing the transport properties. One should also note that simply varying the ratio between the number of trivalent and tetravalent elements, for instance in $Ba_8Ga_xGe_{46-x}$, should have a similar effect [85, 88]. These variations are, however, limited by the fact that such substitutions inevitably lead to changes in the charge carrier concentration. Although it is equally possible to introduce an additional element on the guest sublattice, possibly with a different valence, this approach has so far not been as widely explored [84].

3

Tools and Methods

In the current research project, a combination of experimental and computational techniques has been employed in order to solve the three fundamental puzzles related to inorganic clathrates that were outlined and discussed in Chap. 2:

- Why is the lattice thermal conductivity intrinsically low?
- What is the impact of chemical ordering on the physical properties?
- How can the electronic transport be optimised?

The purpose of this chapter is to describe the methodologies that have been applied to answer each of these questions.[1] As schematically shown in Fig. 3.1, some of the tools have only contributed to a specific problem while others are more widely applicable. In such cases, the given technique will be presented within the context that is deemed to be the most appropriate.

3.1 Determining the lattice thermal conductivity

The two major heat carriers in solid materials are, as noted in Sect. 1.2, electrons and phonons. Since the contribution from the former is directly related to the electrical conductivity, seeEq. (1.8), it cannot be tuned without affecting the PF. This does not apply

[1]For each specific case, the aim is to provide enough background as well as practically relevant information so that the reader could not only use the corresponding methodology but also understand the basic principles on which it is founded. Because of this pragmatic standpoint detailed discussions of the underlying physical phenomena as well as derivations of key equations have been omitted. Interested readers are recommended to consult the cited literature.

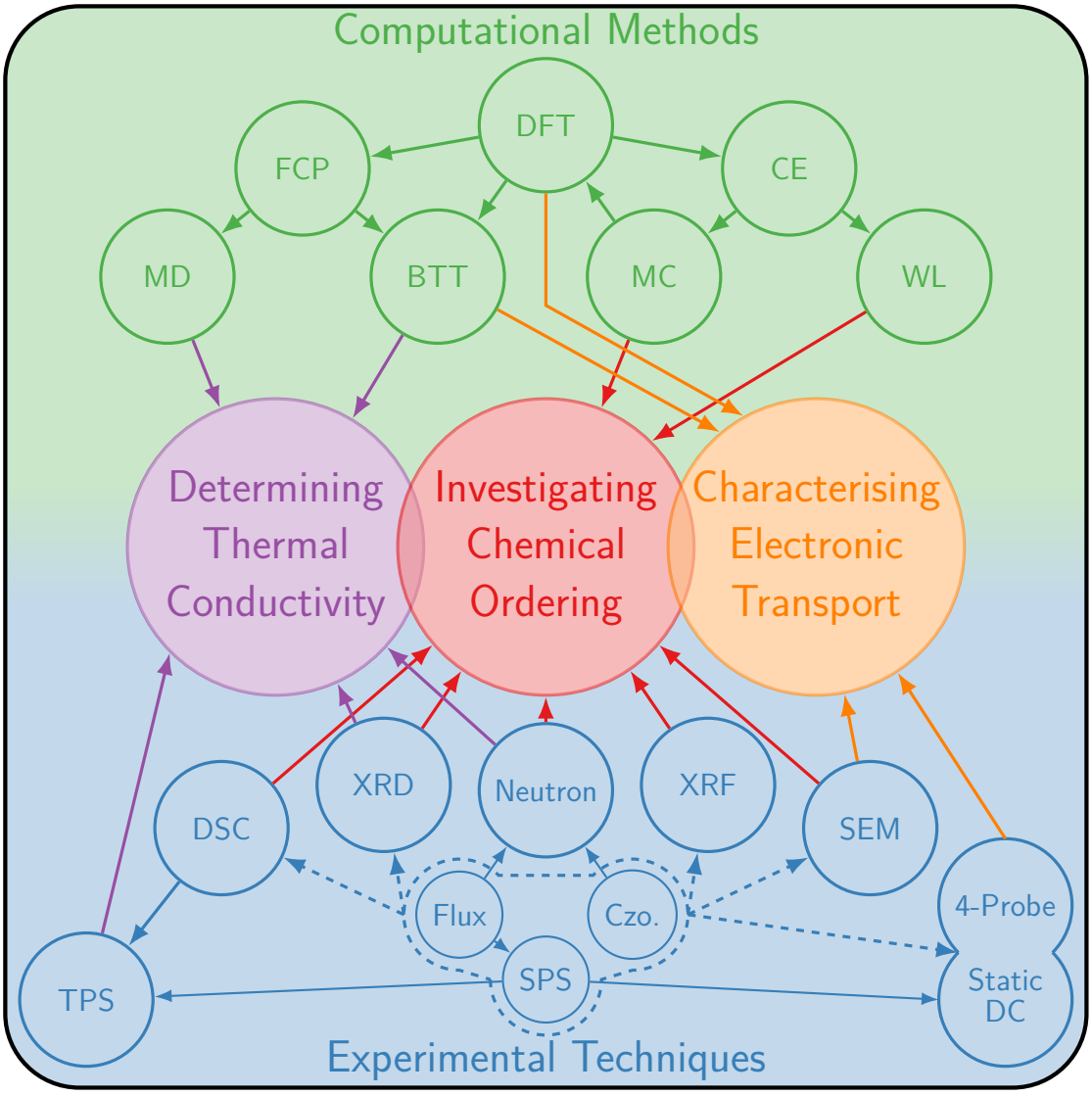

Figure 3.1: Illustration showing the different computational methods and experimental tools that have been used to find answers to the three main questions that are the focus of this thesis: (i) *Why is the lattice* ***thermal conductivity*** *intrinsically low?* (ii) *What is the impact of* ***chemical ordering*** *on the physical properties?* (iii) *How can the* ***electronic transport*** *be optimised?*

to the lattice part, which has therefore received special attention in thermoelectric research. It is, however, not always easy to determine, mainly because thermal transport is a complex process that involves multiple physical phenomena. To entangle the latter it is necessary to conduct a detailed investigation of both dynamical and structural properties.

In Paper II and Paper VII the total thermal conductivity of pellets, compacted using

SPS (Sect. 3.3.1), has been measured using the TPS method (Sect. 3.1.1). Even though this is not a strict requirement, the heat capacities of the materials where independently determined, via DSC (Sect. 3.1.2), since such data can help to reduce the error of the thermal conductivity measurement. To extract the phonon contribution, however, it is necessary subtract the electronic part (Sect. 3.3.3), which can be calculated from the measured resistivity and Seebeck coefficient (Sect. 3.3.2). In order to assess the correlation between structure and heat transport, valuable information can be obtained from X-ray and neutron diffraction studies. Specifically, in Paper IV we fitted an Einstein model (Sect. 3.1.6) to the experimental atomic displacements parameters, determined from refinement of X-ray and neutron diffraction data (Sect. 3.2.2) for flux-grown and Czochralski-pulled single crystals (Sect. 3.2.1).

In addition to the aforementioned experimental techniques, we investigated the heat transport in a representative pseudo-binary clathrate system ($Ba_8Ga_{16}Ge_{30}$) using advanced computational methods, according to the scheme in Fig. 3.2. In particular, two different approaches have been used for calculating the thermal properties, which are both based on IFC models (Sect. 3.1.4). In particular, the data presented in Paper I were obtained via Boltzmann transport theory (Sect. 3.1.7) while Paper V mainly involved MD simulations (Sect. 3.1.8). In these papers, as well as Paper IV, we also utilised simpler harmonic models (Sect. 3.1.5) to extract additional information regarding various dynamical properties.

3.1.1 Transient plane source method

The TPS, originally developed by Gustafsson [113], allows one to simultaneously determine the thermal diffusivity D_T and conductivity κ via a single experiment. While the method is applicable for a wide variety of different materials and setups, the current discussion will focus on the basic procedure for performing high temperature measurements using a Hot Disk® TPS 3500 instrument, which has been employed in all studies related to this project. The measurements have been performed by sandwiching a sensor, in the form of a mica covered nickel double spiral, between a pair of, preferably identical, disk shaped samples within a specially designed oven, which allows the ambient temperature to be controlled. Thanks to the purposefully developed "hot disk" pattern, the probe can both serve as a heater, via the Joule effect, and be used to measure the resulting response, at the same time.

An experiment involves sending an electrical pulse through the spiral and recording the resulting change in the resistivity [113]

$$R(t) = R_0 \cdot (1 + \mathrm{TCR} \cdot \Delta T(t)) \tag{3.1}$$

$$\Leftrightarrow \Delta T(t) = \frac{1}{\mathrm{TCR}} \cdot \left(\frac{R(t)}{R_0} - 1 \right), \tag{3.2}$$

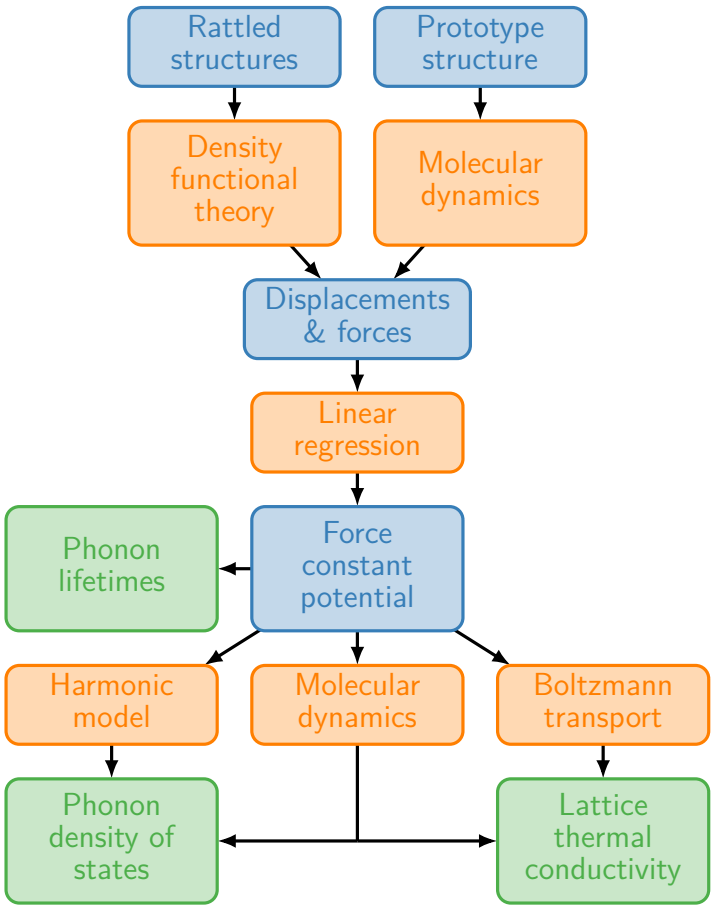

Figure 3.2: Schematic illustration of the procedure used for predicting key properties related to the phononic heat transport via atomic scale calculations. Here, methods, input/output data and final results have respectively been coloured in orange, blue and green.

where R_0 is the initial electrical resistance and TCR is the temperature coefficient of resistivity for the probe. By solving the thermal transport equation for a "hot disk" geometry, it is possible to derive a theoretical formula for the temperature of the sensor

$$\Delta T(\tau) = \frac{P_0}{\pi^{3/2} \cdot r_{\text{sensor}} \cdot \kappa} \cdot \Lambda(\tau). \tag{3.3}$$

Here, P_0 represents the total output power, r_{sensor} the radius of the spiral, and $\Lambda(\tau)$ is a dimensionless function that accounts for geometrical aspects. The dimensionless time $\tau = \sqrt{t/t_{\text{trans}}}$, meanwhile, has been defined by introducing a scale $t_{\text{trans}} = r^2_{\text{sensor}}/D_T$, which is sometimes referred to as the "transient time of the transient recording". As is evident from this pair of formulas, κ can be determined from the slope of the curve obtained by plotting $\Delta T(\tau)$, calculated from the measured $R(t)$, as a function of $\Lambda(\tau)$.

A key parameter to consider when using the TPS method is the probing depth

$$\Delta_p = K \cdot \sqrt{D_T \cdot t_{\text{meas}}}, \tag{3.4}$$

which gives an indication of how far into the sample the heat pulse will penetrate within the measurement time t_{meas} [114]. In this formula, K is a method and equipment dependent parameter, which has been empirically found to take on the value of 2 for the case at hand. From a practical perspective, it must be ensured that the heat pulse does not reach the physical limits of the sample before the end of the measurement. For a pair of identical disk shaped samples, this means that the thickness and radius must be larger than Δ_p and $r_{\text{sensor}} + \Delta_p$, as illustrated in Fig. 3.3. In addition, it has been found that the best accuracy is achieved if the measurement time satisfies the criterion

$$0.3 t_{\text{trans}} \leq t_{\text{meas}} \leq 1.1 t_{\text{trans}}. \tag{3.5}$$

Even though the t_{meas} can be as short as 0.1 s when using a Hot Disk® TPS 3500 instrument, the fact that the smallest available sensor for high temperature measurements has a radius of 3.2 mm limits the minimum size of the samples that can be probed. For this reason, we have only been able to determine the thermal conductivity for sintered pellets (Sect. 3.3.1) and not for the pristine flux-grown and Czochralski-pulled (Sect. 3.2.1) single crystals.

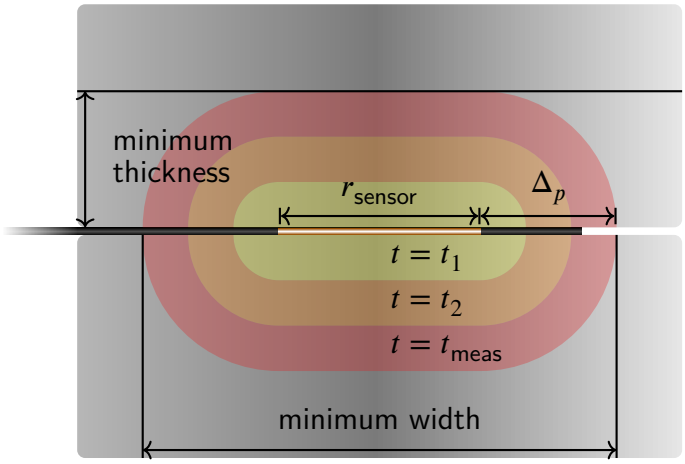

Figure 3.3: Schematic sketch of a measurement based on the TPS method. In particular, it illustrates that the dimensions of the sample must be such that the heat pulse is not able reach the physical limits within the measurment time t_{meas}. In the case of a pair of identical disks, this means that thickness and width must be smaller than Δ_p and $r_{\text{sensor}} + \Delta_p$, where r_{sensor} is the radius of the sensor and $\Delta_p \propto \sqrt{D_T t_{\text{meas}}}$ is the probing depth.

3.1.2 Differential scanning calorimetry

The basic purpose of DSC is to determine the difference in heat flux of a sample and a suitable reference, which is achieved by monitoring their respective temperatures as a function of time [115]. For the project at hand, the goal of these experiments, which were conducted using a Mettler Toledo DSC2 instrument, was to measure the specific heat capacity. The reason for this was for two-fold. Firstly, it is recommended that this property is supplied when using the smallest Hot Disk® sensor (Sect. 3.1.1) and, secondly, because it is suitable for characterising phase transitions (Sect. 3.2.8). In practice, this involves three separate measurements, namely on (i) an empty crucible, (ii) a reference compound (sapphire), and (iii) the material of interest. The specific heat capacity can then be calculate as [116]

$$c_p^{\text{material}} = \frac{\dot{H}_{\text{material}} - \dot{H}_{\text{empty}}}{m_{\text{material}}} \frac{m_{\text{sapphire}}}{\dot{H}_{\text{sapphire}} - \dot{H}_{\text{empty}}} \tag{3.6}$$

where $\dot{H} = \partial H/\partial t$ is the time derivative of the enthalpy, which in this context is equivalent to the measured heat flow, while m is the mass. It is recommended to use a large amount of material while at the same time ensuring that the heat capacities for the actual and reference samples are about the same,

$$c_p^{\text{material}} \cdot m_{\text{material}} \approx c_p^{\text{sapphire}} \cdot m_{\text{sapphire}}, \tag{3.7}$$

so as to obtain high heat flow signals of comparable magnitude. The fact that the crucibles, additionally, need to be made of a thermally conductive material poses a problem in the present context since many inorganic clathrates have a tendency to react even with noble metals. For this reason, the crucibles that were used to conduct such experiments in this project had to be lined with graphite sheets.

3.1.3 Cluster representation

When extracting IFCs (Sect. 3.1.4), as well as constructing alloy CEs (Sect. 3.2.5), significant simplifications, which reduce the computational effort, can be achieved by taking advantage of the inherent symmetries of the structure of interest [117, 118]. To facilitate this process, it is advantageous to represent the lattice in a way that makes it easy to identify equivalent groups of sites. The latter, which are generally referred to as "clusters", are commonly classified as singlets, pairs, triplets, quadruplets and so on depending on the number of sites, as depicted in Fig. 3.4. After having obtained a complete list of all such clusters, these can be grouped into so called "orbits". This is achieved by testing their equivalence with respect to both permutations of the lattice sites as well as the symmetry operations of the underlying space group.

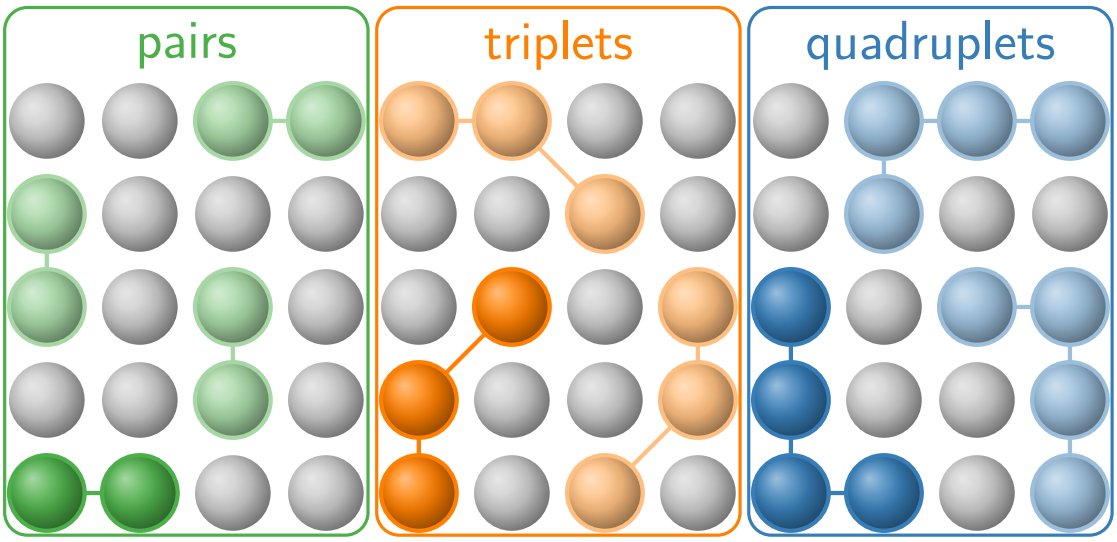

Figure 3.4: Schematic illustration of the principle behind cluster construction. The atoms on a lattice can be grouped into pairs (green), triplets (orange), quadruplets (blue) etc. Since the clusters shown in bright colours are symmetry equivalent to those of the same order depicted with a paler tone, they all belong to the same orbit.

3.1.4 Interatomic force constants

IFCs offer a convenient way of calculating the dynamical properties of materials since they represent the forces acting between the constituent atoms and can be directly evaluated given that all atomic positions are known [118]. Each IFC corresponds to a single coefficient in the Taylor series of the potential energy surface V with respect to the atomic displacements $\mathbf{u} = \mathbf{R} - \mathbf{R}_0$, where $\mathbf{R}_0$ indicates a set of reference positions,

$$\begin{aligned} V =& V_0 + \sum_i \sum_\alpha \Phi_i^\alpha u_i^\alpha + \frac{1}{2!} \sum_{ij} \sum_{\alpha\beta} \Phi_{ij}^{\alpha\beta} u_i^\alpha u_j^\beta + \frac{1}{3!} \sum_{ijk} \sum_{\alpha\beta\gamma} \Phi_{ijk}^{\alpha\beta\gamma} u_i^\alpha u_j^\beta u_k^\gamma \\ &+ \frac{1}{4!} \sum_{ijkl} \sum_{\alpha\beta\gamma\eta} \Phi_{ijkl}^{\alpha\beta\gamma\eta} u_i^\alpha u_j^\beta u_k^\gamma u_l^\eta + \cdots \end{aligned} \tag{3.8}$$

Here, each Φ represents the IFC that is related to the specific atoms and coordinate directions indicated by the Latin and Greek indices, respectively. In practice, however, it is possible to disregard both the first and second term. The reason is, respectively, that the addition of a constant term does not affect the dynamical properties and because it is possible to choose the equilibrium lattice at zero temperature as the reference, for which all forces must vanish. This means that the α component of the force that acts

on atom i can be expressed as

$$F_i^\alpha = -\frac{\partial V}{\partial u_i^\alpha} = -\sum_j \sum_\beta \Phi_{ij}^{\alpha\beta} u_j^\beta - \frac{1}{2!} \sum_{jk} \sum_{\beta\gamma} \Phi_{ijk}^{\alpha\beta\gamma} u_j^\beta u_k^\gamma - \frac{1}{3!} \sum_{jkl} \sum_{\beta\gamma\eta} \Phi_{ijkl}^{\alpha\beta\gamma\eta} u_j^\beta u_k^\gamma u_l^\eta + \cdots \tag{3.9}$$

Depending on the information that one seeks to obtain, the expansion in Eq. (3.8) is truncated at different orders [118]. In the harmonic approximation, which is commonly used for determining the dynamical properties of materials (Sect. 3.1.5), only the second order IFCs are considered. The next term is, however, required when calculating the thermal conductivity, using BTT (Sect. 3.1.7), while higher orders must be included to be able to account for the temperature dependence of the phonon modes.

As should be expected, extraction of reliable IFCs from a set of reference forces becomes increasingly difficult the higher the order and various methods have therefore been developed to solve this problem. In this project, harmonic IFCs have, for instance, been obtained by using the so-called direct approach [119], as implemented in the Phonopy toolkit [120]. The underlying principle for this method is that $\Phi_{ij}^{\alpha\beta}$ can be calculated if one displaces atom j by a distance u_j^β in the direction β and determines the resulting force F_i^α on atom i along α since

$$\Phi_{ij}^{\alpha\beta} = \frac{\partial V}{\partial u_i^\alpha \partial u_j^\beta} \approx \frac{F_i^\alpha}{u_j^\beta}. \tag{3.10}$$

The problem, however, is that the number of reference calculations required rises sharply as the size of the unit cell increases, the symmetry is reduced, and/or additional orders are taken into account. The direct method is, therefore, only suitable for relatively simple cases.

A more efficient methodology, which is implemented in the hiphive package [118], is to use regression schemes based on machine learning techniques (Sect. 3.2.6) [121, 122]. Significant simplifications can, additionally, be made by taking advantage of the inherent symmetries of the underlying atomic structure as well as the constraints that can be placed on the IFCs, which reduces the number of independent parameters that needs to be considered. In practice, this is achieved by collecting the atoms into clusters (Sect. 3.1.3), from which symmetry equivalent sets can be identified. Additionally, it is often possible to disregard IFCs that are numerically insignificant, because their magnitude tends to decay with the order as well as the number of interacting atoms and the distance between them. The resulting system of equations can be expressed in matrix form as

$$\mathbf{F} = \mathbf{A}\mathbf{x}, \tag{3.11}$$

where **F** is the set of reference forces, **x** denotes the free parameters, which are to be determined, while **A** represents the so-called sensing matrix. Each row in the latter is constructed based on the displacement vector associated with the corresponding force subject to the symmetry constraints as well as the sum rules, which are required to ensure that the IFCs are rotationally and translationally invariant. Depending on the dimensions of **A**, or more precisely whether the corresponding system of equations is over- or underdetermined, one then has to choose a suitable regression technique and decide if it is desirable to employ a feature selection method to identify the most important parameters. The gain of doing so is often three-fold since it not only reduces the risk of overfitting but also makes the model more transferable and computationally efficient.

In this project, the target forces have be obtained in either of two forms, namely a set of "rattled" structures or MD trajectories [118]. The first alternative, which is implemented HIPHIVE [118], is suitable when only considering IFCs of the lowest orders. In particular, it involves taking a reference structure and applying random displacements drawn from a Gaussian distribution, with a standard deviation that has been selected so as to give amplitudes on the order of 0.01 Å. Note that it is, generally, advisable to include IFCs of one order higher than what is strictly required, since their contributions will otherwise be effectively included in the lower-order terms. The corresponding forces are usually obtained via DFT calculations (Sect. 3.2.4), for instance, using VASP [123]. Extracting IFCs from MD simulations, which can be performed with the same type of software, is even more straightforward since the trajectories will automatically contain all the necessary information, in the form of both displacements and forces.

3.1.5 Harmonic lattice dynamics

The most common approach for calculating the dynamical properties of a material is to use the harmonic approximation, which is phenomenologically equivalent to modelling the material as a collection of spheres connected by springs [124]. According to Hooke's law, this means that the forces and displacements are linearly dependent and as a result only second-order IFCs are taken into account. The key benefit of this simplification is that it allows the thermodynamic properties to be treated analytically. One of the simplest yet physically relevant conceptual models is the monoatomic chain [125]. If only nearest-neighbour interactions are taken into account the corresponding equation of motion for atom j can be written as

$$m\frac{\mathrm{d}^2 u_j}{\mathrm{d}t^2} = \Phi\left(u_{j+1} + u_{j-1} - 2u_j\right), \tag{3.12}$$

where m represents the mass, Φ is the second-order IFC and u the displacement. By assuming that the time dependence is given by a factor of $\exp(i\omega t)$, one obtains a set

of plane wave solutions of the form

$$u_{j\pm1} = u \exp\left(i(j \pm 1)qa\right), \tag{3.13}$$

where a is the lattice spacing. In turn, these can be used to derive the following dispersion relationship between the frequency ω and the wavenumber q:

$$\omega^2 = \frac{4\Phi}{m} \sin^2\left(\frac{qa}{2}\right), \tag{3.14}$$

which is depicted in Fig. 2.2.

When considering more complex systems, it is convenient to introduce the dynamical matrix $\mathbf{D}(\mathbf{q})$, which is defined in such a way that the harmonic frequencies $\omega_{\mathbf{q}j}$ can be determined by solving the eigenvalue problem [120]

$$\mathbf{D}(\mathbf{q})\mathbf{e}_{\mathbf{q}j} = \omega_{\mathbf{q}j}\mathbf{e}_{\mathbf{q}j}, \tag{3.15}$$

where $\mathbf{e}_{\mathbf{q}j}$ is the phonon polarisation vector for wave vector $\mathbf{q}$ and band index j. By using a notation that keeps tracks of both the atomic (k) and the unit cell (l) indices, the elements in $D(\mathbf{q})$ take on the form

$$D^{\alpha\beta}_{kk'} = \sum_{l'} \frac{\Phi_{\alpha\beta}(0k, l'k')}{\sqrt{m_k m_{k'}}} \exp\left(i\mathbf{q} \cdot \left[\mathbf{r}(l'k') - \mathbf{r}(0k)\right]\right), \tag{3.16}$$

where $\Phi_{\alpha\beta}(lk, l'k')$ are the second-order IFCs while $\mathbf{r}(lk)$ corresponds to the equilibrium position and m_k the mass of atom k.

Once the harmonic frequencies have been determined from the second-order IFCs, the phonon DOS can be directly calculated as [120]

$$\rho_{\mathrm{ph}}(\omega) = \frac{1}{N_{\mathrm{uc}}} \sum_{\mathbf{q}j} \delta\left(\omega - \omega_{\mathbf{q}j}\right), \tag{3.17}$$

where N_{uc} is the total number of unit cells. The same is true for a number of key thermal properties including the internal energy,

$$E = \sum_{\mathbf{q}j} \hbar\omega_{\mathbf{q}j} \left[\frac{1}{2} + \frac{1}{\exp\left(\hbar\omega_{\mathbf{q}j}/k_B T\right) - 1}\right], \tag{3.18}$$

the entropy

$$S = \frac{1}{2T} \sum_{\mathbf{q}j} \hbar\omega_{\mathbf{q}j} \coth\left[\hbar\omega_{\mathbf{q}j}/2k_B T\right] \tag{3.19}$$

$$- k_B \sum_{\mathbf{q}j} \ln\left[2 \sinh\left(\hbar\omega_{\mathbf{q}j}/2k_B T\right)\right], \tag{3.20}$$

the Helmholtz free energy

$$F = \frac{1}{2T}\sum_{\mathbf{q}j}\hbar\omega_{\mathbf{q}j} + k_B T\sum_{\mathbf{q}j}\hbar\omega_{\mathbf{q}j}\ln\left[1-\exp\left(\hbar\omega_{\mathbf{q}j}/k_B T\right)\right], \tag{3.21}$$

as well as the heat capacity at constant volume

$$c_v = \sum_{\mathbf{q}j}\hbar\omega_{\mathbf{q}j}k_B\left(\frac{\hbar\omega_{\mathbf{q}j}}{k_B T}\right)^2\frac{\exp\left(\hbar\omega_{\mathbf{q}j}/k_B T\right)}{\left[\exp\left(\hbar\omega_{\mathbf{q}j}/k_B T\right)-1\right]^2}. \tag{3.22}$$

In this work, Phonopy [120] has been used to evaluate the above equations using second-order IFC extracted with hiphive [118] (Sect. 3.1.4)

3.1.6 Einstein model

In addition to the previously discussed harmonic description, there exists a number of even simpler analytical models that have been developed for the purpose of describing the lattice dynamics in crystalline materials. Among these, the theories developed respectively by Debye and Einstein are perhaps the most well-established and have, for instance, frequently been applied to extract information regarding thermodynamic properties from diffraction experiments [74]. The former, is specifically based on the assumption that the system can be represented by an elastic continuum. As a result, the dispersion relation, which relates the vibrational frequency and the distance $\mathbf{q}$ in reciprocal space, is linear; $\omega = vq$, where $\mathbf{v}$ is the sound velocity. Although the Debye approximation is convenient for modelling the host framework in clathrates, it cannot account for the behaviour of the guest atoms. For this purpose, the Einstein model is more suitable, which is based on the approximation that the material behaves as a collection of independent oscillators with the same frequency ω_0 [74, 125]. This effectively means that the guest-host interactions are sufficiently weak that their respective vibrations are more or less independent, which leads to the following expression for the atomic displacement

$$u(T) = \frac{\hbar}{2mk_B T_E}\coth\left(\frac{T_E}{2T}\right) + d^2, \tag{3.23}$$

where $\hbar$ is Planck's constant, T_E the Einstein temperature and m the atomic mass while d represents the static disorder. Since T_E is a characteristic property it is convenient for comparing the dynamical responses of different materials. The temperature-independent d parameter meanwhile is of special interest in this work since it can be used to assess how the off-centring of the guest atom is affected by the degree of chemical ordering (Sect. 3.2).

3.1.7 Boltzmann transport theory for phonons

The two main computational methods used in this project for modelling heat transport are BTT and MD simulations (Sect. 3.1.8). The BTT approach has been implemented in several software packages including Phono3py [126] and shengBTE [127]. In this work, the lattice thermal conductivity has been calculated using the latter and the phonon life times via the former. To understand the basic principle for this approach, the first step is to note that the heat current $\mathbf{J}$ that results from a temperature gradient $\boldsymbol{\nabla} T$ can be expressed as [127]

$$\mathbf{J} = \sum_b \int n_s \hbar \omega_s \mathbf{v}_s \frac{\mathrm{d}\mathbf{q}}{(2\pi)^3}. \tag{3.24}$$

In this equation, ω_s and $\mathbf{v}_s$ represent the angular frequency and group velocity, respectively, while s corresponds to the mode in branch (b) with wave vector $\mathbf{q}$ and n_s is the mode occupation number. In equilibrium, which means that there are no thermodynamic forces present, the latter follows Bose-Einstein statistics,

$$n_0(\omega_s) = \frac{1}{\exp\left(\hbar\omega_s / k_B T\right) - 1}. \tag{3.25}$$

BTT provides a way of calculating the deviation between n_s and $n_0(\omega_s)$ caused by the temperature gradient $\boldsymbol{\nabla} T$ [127]. The resulting force drives a diffusion process that is counteracted by various types of scattering. Since the corresponding rates of change with respect to the phonon distribution must vanish under steady state conditions, one finds that

$$\left.\frac{\partial n_s}{\partial t}\right|_{\text{scattering}} = -\left.\frac{\partial n_s}{\partial t}\right|_{\text{diffusion}} = \boldsymbol{\nabla} T \cdot \mathbf{v}_s \frac{\partial n_s}{\partial T}. \tag{3.26}$$

While the first term in the above expression can encompass a wide range of different processes, in the case of lattice thermal transport it is typically dominated by phonon-phonon scattering together with interactions between phonons and lattice imperfections, including both isotope mass variations and chemical disorder. Under the assumption that the temperature gradient is sufficiently small, the perturbed distribution can be expressed as

$$n_s = n_0(\omega_s) - \mathbf{F}_s \cdot \boldsymbol{\nabla} T \frac{\partial n_0(\omega_s)}{\partial t}. \tag{3.27}$$

According to Li *et al.*[127], it is possible to derive a linearised version of this equation,

$$\mathbf{F}_s = \tau_s^0 (\mathbf{v}_s + \boldsymbol{\Delta}_s), \tag{3.28}$$

provided that only two- and three-phonon scattering is taken into account.

The relaxation time, or equivalently the lifetime of the phonon mode s, τ_s^0 is often calculated in the RTA using perturbation theory. This means that the term $\mathbf{\Delta}_s$ essentially gives a measure of how much the system deviates from this approximation, which will be reflected by both the distribution n_s as well as the heat current $\mathbf{J}$. As the lattice thermal conductivity tensor can be written as

$$\kappa^{\alpha\beta} = \frac{1}{k_B T^2 \Omega} \sum_s n_0(n_0+1)(\hbar\omega_s)^2 v_s^\alpha F_s^\beta, \tag{3.29}$$

where Ω is the volume, the main problem is to evaluate τ_s^0 and $\mathbf{\Delta}_s$. This requires at least the third-order IFCs $\Phi_{ijk}^{\alpha\beta\gamma}$ via the three-phonon scattering rates, which means that $\boldsymbol{\kappa}$ can be readily calculated once the former have been extracted for the system of interest (Sect. 3.1.4). Specifically, this is achieved by iteratively solving the linearised Boltzmann transport equation, as represented by Eq. (3.28), based on the initial assumption $\mathbf{F}_s^0 = \tau_s^0 \mathbf{v}_s$.

Another interesting property that can be directly obtained from the third-order IFCs are the phonon lifetimes τ_s, which can, for example, help explain why the thermal conductivity exhibits a specific behaviour. In particular, these are defined as the reciprocals of the corresponding linewidths,

$$\tau_s = \frac{1}{2\Gamma_s(\omega_s)}, \tag{3.30}$$

which can, in turn, be obtained once the third order IFCs have been transformed to reciprocal space ($\tilde{\Phi}_{ss's''}$). Specifically, these are related by the following formula

$$\begin{aligned}\Gamma_s(\omega) = \frac{18\pi}{\hbar^2} \sum_{s's''} \left|\tilde{\Phi}_{ss's''}\right|^2 \Big\{ &\left(n_{s'} + n_{s''} + 1\right) \delta\left(\omega - \omega_{s'} - \omega_{s''}\right) \\ &+ \left(n_{s'} - n_{s''}\right) \left[\delta\left(\omega + \omega_{s'} - \omega_{s''}\right) - \delta\left(\omega - \omega_{s'} + \omega_{s''}\right)\right] \Big\},\end{aligned} \tag{3.31}$$

which can be derived using Fermi's golden rule.

3.1.8 Molecular dynamics simulations

In this project, MD simulations have been performed for two separate purposes: firstly to generate reference data that can be used to extract IFCs and, secondly, to calculate the lattice thermal conductivity. Specifically, the VASP software [123] was used in the former case and the GPUMD code [128], in the latter. Regardless of the implementation, the fundamental principle remains the same. MD simulations are a classical method for evolving a system from an initial condition, specified in terms of the initial position $\mathbf{r}_i$ and momentum $\mathbf{p}_i$ for each atom i, based on Newtonian mechanics. This means that the

force acting on an atom, under the influence of a force field represented by a potential V, is given by Newton's second law [129]

$$\mathbf{F}_i = -\frac{\partial V(\mathbf{r}_i)}{\partial \mathbf{r}_i} = \frac{\partial \mathbf{p}_i}{\partial t}. \tag{3.32}$$

The temperature, which is one of the key properties to consider when setting up a MD simulation can be directly related to the ensemble average of the kinetic energy per atom via the equipartition theorem,

$$T = \frac{2}{3k_B}\left\langle \frac{1}{2}m|\mathbf{v}|^2 \right\rangle. \tag{3.33}$$

As was eluded to earlier, one of the other requirements is the specification of a suitable force field. When using VASP [123], the interatomic interactions have, specifically, been modelled in the same way as when running conventional DFT calculations (Sect. 3.2.4). The GPUMD [128] simulations, meanwhile, were based on a force constant potential that had been constructed from a set of IFCs using the HIPHIVE package (Sect. 3.1.4).

While calculating the ensemble average of a given property $\langle Q \rangle$ is convenient when using an MC based approach, the same cannot be said for MD simulations, for which it is much more natural to consider the time average $\bar{Q}$ [129]. In any case, it is necessary to assume that the system is "ergodic", which means that

$$\langle Q \rangle = \bar{Q} = \int_0^\infty Q \mathrm{d}t, \tag{3.34}$$

where the integral is in practice replaced by a sum over the entire MD trajectory divided by the total number of steps. While MD simulations are conventionally performed in the microcanonical ensemble, for which the volume, energy and number of atoms are conserved, it is in many cases more desirable to use thermodynamic ensembles such as the canonical one, which keeps the temperature constant instead of the energy. This is achieved by connecting the system to a large heat bath. It is important to note that the nature of the coupling is not self-evident. Rather, many different alternatives thermostats have been developed, which are suitable for different applications. Some of these, such as the one developed by Andersen, are stochastic in nature while others are deterministic. The latter is true for the Nosé-Hoover thermostat, which has been employed for all the MD simulations in this project. GPUMD [128] employs a generalised version, which connects the system to a chain of such thermostats.

For the type of equilibrium MD simulations outlined above, the components of thermal conductivity tensor can be calculated via the Green-Kubo relation [128]

$$\kappa^{\alpha\beta}(t) = \frac{1}{k_B T^2 \Omega}\int_0^t \langle J^\alpha(t') J^\beta(0)\rangle \mathrm{d}t', \tag{3.35}$$

in which t represents the correlation time, Ω the volume, and $\langle J^{\alpha}(t')J^{\beta}(0)\rangle$ the heat current auto-correlation function. In practice, the latter can be evaluated as the average of the product between the components of the heat current $\mathbf{J}$ along α and β over different time origins. While this equilibrium MD method has been successfully used for calculating the thermal conductivities for a variety of materials, it has a potential drawback, namely that the signal-to-noise ratio decreases with the correlation time [130]. An alternative approach is HNEMD, which was exclusively employed in this project. Although it also involves calculating the thermal conductivity tensor via the the Green-Kubo relation, in this case the system is perturbed by a driving force $\mathbf{F}_e$ [130]. As a result, the components of the former can be determined via the relationship

$$\frac{\langle J^{\alpha}(t)\rangle_{\mathrm{ne}}}{T\Omega} = \sum_{\beta} \kappa^{\alpha\beta}(t) F_e^{\beta}, \tag{3.36}$$

where the nonequilibrium average of the heat current component along α is given by

$$\langle J^{\alpha}(t)\rangle_{\mathrm{ne}} = \left(\frac{1}{k_B T} \int_0^t \langle J^{\alpha}(t')J^{\alpha}(0)\rangle \mathrm{d}t' \right) \cdot \mathbf{F}_e. \tag{3.37}$$

A problem with the expression in Eq. (3.36) is that the functions $\kappa^{\alpha\beta}(t)$ tend to exhibit very large fluctuations and it is therefore more convenient to consider the accumulated average

$$\bar{\kappa}^{\alpha\beta}(t) = \frac{1}{t} \int_0^t \frac{\langle J^{\alpha}(t')\rangle_{\mathrm{ne}}}{T\Omega F_e^{\beta}} \mathrm{d}t'. \tag{3.38}$$

In many cases it is valuable to discern the relative contribution of different phonon modes to the lattice thermal conductivity at a given temperature. This can be achieved via a spectral decomposition, which leads to the expression[130]

$$\frac{\langle J^{\alpha}(\omega)\rangle_{\mathrm{ne}}}{T\Omega F_e} = \sum_{\beta} \kappa^{\alpha\beta}(\omega) F_e^{\beta}. \tag{3.39}$$

Note that this equation is identical to Eq. (3.36) except for the fact that it includes the spectral heat current $J^{\alpha}(\omega)$ and the thermal conductivity $\kappa^{\alpha\beta}(\omega)$. Yet more information can be gained by calculating the phonon DOS $\rho_{\mathrm{ph}}(\omega)$ utilising the fact that it is equivalent to the Fourier transform of the velocity ($\mathbf{v}(t)$) autocorrelation function [131]

$$\langle v^{\alpha}(t)v^{\alpha}(0)\rangle = \frac{1}{2\pi} \int_{-\infty}^{\infty} \rho_{\mathrm{ph}}(\omega) e^{-i\omega t} \mathrm{d}\omega. \tag{3.40}$$

3.2 Investigating chemical ordering

In order to assess the degree of chemical ordering, it is necessary to probe the atomic structure of the material of interest. In the case of inorganic clathrates, this requires, as mentioned in Sect. 2.2, state-of-the-art experimental and computational methods. Due to similarities in the relevant scattering cross-sections, we used a combination of X-ray and neutron diffraction experiments (Sect. 3.2.2) performed on single crystals synthesised via either flux-growth or Czochralski-pulling (Sect. 3.2.1) in order to determine the SOFs. Independent measures of the chemical compositions were obtained by performing XRF (Sect. 3.2.3) as well as energy dispersive X-ray spectroscopy (Sect. 3.3.5). In Paper III, and to some extent Paper VII, we focused on a different aspect of chemical ordering, namely the existence of order-disorder transitions. To this end, we used DSC to determine the heat capacities (Sect. 3.1.2).

As was mentioned in Sect. 2.2, it is necessary to use an approach based on a combination of DFT (Sect. 3.2.4) calculations, alloy CEs (Sect. 3.2.5) and MC simulations (Sect. 3.2.7), as outlined in Fig. 3.5, in order to efficiently sample the large configuration space. In fact, we employed this approach in Paper III, Paper IV, Paper VI, and Paper VIII for the purpose of calculating the SOFs, since these give a direct measure of the chemical ordering. In addition, the structures employed to investigate the lattice dynamics in Paper I, Paper IV, and Paper V as well as the electronic transport in Paper III and Paper VII were generated using the same CEs. In order to study transformations between ordered and disordered states, which was the aim of Paper III and Paper VIII, we had to employ a slightly different approach, which entailed using the WL algorithm (Sect. 3.2.8).

3.2.1 Synthesis methods

To date, a wide variety of methods has been employed to produce thermoelectric materials in general and inorganic clathrates in particular [74, 96, 132]. In this project, however, only three different techniques have been employed: direct reaction, Czochralski-pulling, and flux-growth. The former is generally deemed to be the most conventional and involves first mixing and then heating the pure elements, or precursors, under vacuum or an inert atmosphere. While simple, there are several key issues to consider when implementing this method. Firstly, it is important to ensure that the reaction mixture is sufficiently homogeneous. Since the batches prepared in this project have been relatively small ($\leq 12\,\mathrm{g}$) and the constituent elements melt congruently, no special precautions were required. One must, moreover, pay heed to the volatility of the reactants, since it might be necessary to compensate for the resulting loss of material as well as the suitability of the container in order to avoid unwanted side reactions. Both of these considerations are relevant in the present context. To be precise, an excess of barium had to be added because of its high vapour pressure at the reaction temperature,

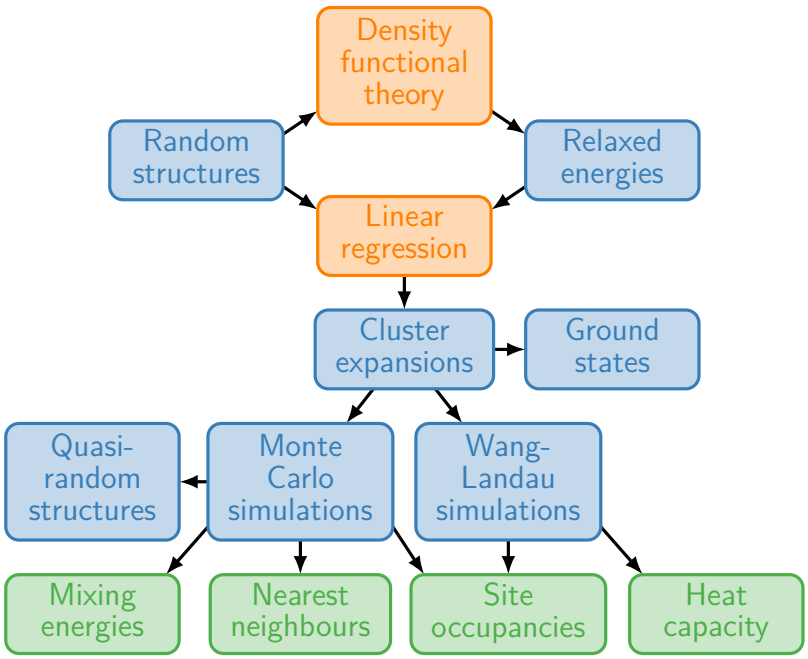

Figure 3.5: Conceptual illustration of the procedure for constructing and sampling an alloy CE model. Here, methods, input/output data and final results have respectively been coloured in orange, blue, and green.

which in the case of the Ge-based clathrates exceeds $\sim$ 900 °C. In addition, the choice of container is very relevant since the elements of which inorganic clathrates typically consist have strong tendencies to react with some typical crucible materials [96]. Here, alumina has been consistently used since it is suitable for compounds that contain alkaline earth metals and is less costly than some of the alternatives. While the approach outlined above is relatively straightforward and is not reliant on advanced equipment other than a glove box and a high temperature furnace, a potential drawback is that the product is typically a brittle polycrystalline powder or ingot, which is ill-suited for property measurements. As a result, the as-cast material must often be compacted into pellets, for instance via SPS, before it is possible to measure the thermal conductivity (Sect. 3.1.1) as well as the resistivity and Seebeck coefficient (Sect. 3.3.2).

While conducting diffraction experiments (Sect. 3.2.2) on a polycrystalline powder is a standard procedure in material science, single crystals are preferable for determining intrinsic physical properties [96, 132]. A convenient method for producing such samples is to allow the precursors to react within a suitable flux, typically in the form of a metal with a low melting point, that need not be one of the reactants even though this is relatively common in the case of inorganic clathrates. After heating the mixture until all reactants have dissolved, the supersaturated liquid is slowly cooled, which leads to spontaneous nucleation. The resulting collection of single crystals can be separated

either mechanically or chemically, for example through centrifugation and etching, respectively. Due to their relatively small sizes (0.1 mm to 10 mm), the crystallites are typically suitable for single crystal X-ray but not neutron diffraction. This also means that they, similarly to the material obtained using the conventional approach, must be powderised and compacted before transport property measurements can be performed.

An alternative is to use the Czochralski method, which is one of the most common commercial techniques for growing large single crystals [96]. The main inconvenience related to this process is the need for a specially designed growth apparatus, which is illustrated in Fig. 3.6. If available, however, the procedure is relatively straightforward [133]. The first step is to perform a conventional synthesis as outlined above. The material thus produced is then placed in a suitable crucible, which in the present case must be made of a material such as glassy carbon that can be heated via induction. After the mixture has been sealed within the growth chamber, the latter is evacuated before being refilled with an inert gas. Note that it is often advisable to take extra precautions to ensure that no moisture or oxygen remains. The crucible is then heated to a temperature just above the melting point of the starting material, which must melt congruently for this technique to work. Next a seed crystal, which is attached to a pulling rod, is lowered into the melt. When the latter is slowly pulled back up, while being rotated at a constant speed, a crystallisation process will takes place at the interface between the molten and solid material, which will eventually lead to the growth of a rod-shaped crystal.

3.2.2 X-ray and neutron diffraction

Powder X-ray diffraction is one the most common techniques for characterising properties related to the long-range order in crystalline solids [134, 135]. This encompasses not only determination of the crystal structure and lattice parameters but also quantification of the phases present in the sample, various measures of the microstructure as well as the electron density distribution. While there exist commercial laboratory scale instruments for conducting such experiments, better results can be obtained when using synchrotron radiation since the brilliance is about 10^{13} times higher. Here, accessibility is the main bottleneck, since there are only a few such facilities in the entire world. While neutron sources are even less abundant, the fact that these particles are scattered by the nuclei rather than the electron cloud means that the corresponding scattering cross-sections do not increase linearly with the atomic number, which is the case for X-rays. This can be a distinct advantage if the material of interest contains neighbouring elements in the periodic table, which is true for several of the systems of interest in this project. Another consequence is that the chance of an incoming neutron being scattered at a given atomic plane is significantly smaller compared to an X-ray photon, which means that the sample sizes must generally be significantly larger. Depending on the material, this can be a severe limitation, especially for single-crystal

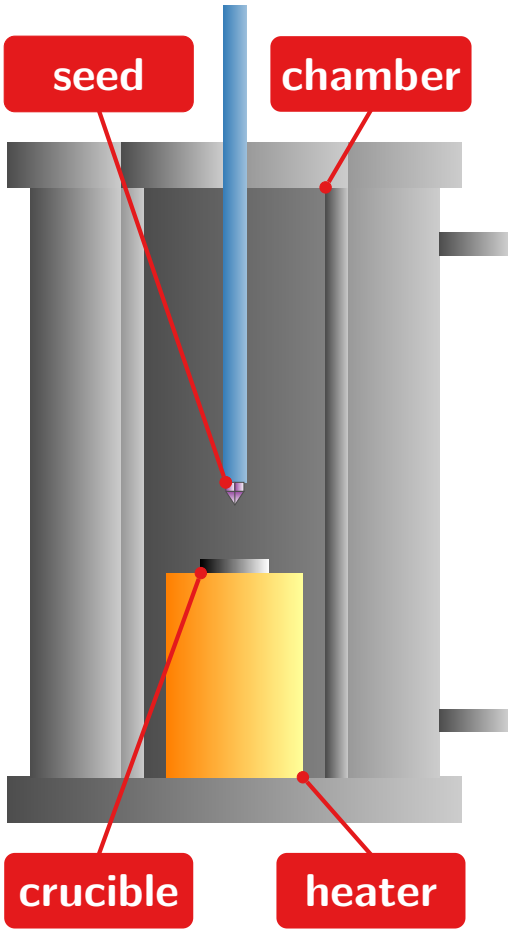

Figure 3.6: Schematic depiction of a Czochralski growth apparatus.

diffraction.

The general principle for any diffraction process is that the scattering of the incident beam, regardless of its nature, by the different crystalline planes leads to interference effects [134, 135]. In particular, the diffraction pattern will display a maximum at angles θ_{hkl} that satisfy the Bragg condition

$$n\lambda = 2a_{hkl} \sin\left(\theta_{hkl}\right), \tag{3.41}$$

since this means that the scattered waves are in phase, as can be seen from the sketch in Fig. 3.7. Here, a_{hkl} is the distance between the parallel planes that correspond to the Miller indices h, k, and l while λ is the wavelength of the radiation.

One should note that what is actually detected is a Fourier transform of the crystal

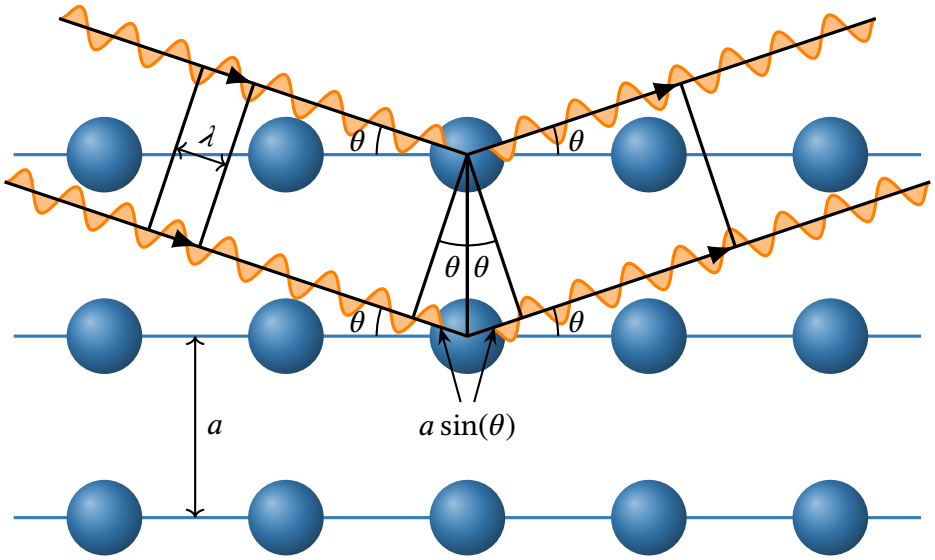

Figure 3.7: Sketch of the Bragg condition, which shows a pair of incoming rays that are scattered on the first and second atomic plane. These will arrive at the distant detector in phase, and therefore give rise to a peak in the diffraction pattern, if the difference in the distance they have travelled ($2d\sin(\theta)$) is equal to an integer multiple of the wavelength (λ).

structure in the form of intensities $I(h,k,l) \propto |F(h,k,l)|^2$, where

$$F(h,k,l) = \sum_j f_j \exp\left(hx_j + ky_j + lz_j\right) \tag{3.42}$$

are the crystallographic structure factors. Here, the sum runs over all atoms j, which are found at the coordinates (x_j, y_j, z_j) relative to the unit cell and are each associated with an atomic scattering factor f_j. As suggested by the above formulas, the main drawback of studying a powder is that the diffraction pattern will have the shape of a ring and correspond to an average over a large collection of small crystallites with different orientations. For a single crystal meanwhile the pattern is three-dimensional and contains information for each of the individual reflections. Such samples can therefore be more suitable when attempting to solve an unknown crystal structure. This is, however, not always the case. If neutron diffraction is required, for instance, the size requirements might be prohibitive.

A powder diffraction pattern acts like a fingerprint that can be used to identify individual phases in a given sample. It contains a wealth of information, which can be extracted via the Rietveld refinement method. In particular, this is achieved by modelling the locations, intensities, and shapes of the different peaks using a variety of more or less empirical functions. It is important to keep in mind that these must account for various aspects of the instrument itself in addition to the inherent properties

of the sample, which encompasses not only the lattice structure but also the geometries, orientations, and size distribution of the individual grains. Another key issue is that some peaks typically overlap, and might even be impossible to distinguish for low symmetry systems. To circumvent these issues, the Rietveld refinement approach will, given that it has been provided with a suitable trial structure, assign a suitable mathematical function, such as a Gaussian, to each peak position and then combine these into a single line pattern, which is compared to the diffraction data. By modifying the parameters that govern the intensities, shapes and locations of the peaks in an iterative procedure, the discrepancy is successively reduced.

In addition to monitoring the plot of the difference between the calculated and observed patterns, the agreement with the observations is also assessed via several measures [136]. This includes the weighted-profile R value,

$$R_{\mathrm{wp}} = \left\{ \frac{S_y}{\sum_i w_i y_i(\mathrm{obs})^2} \right\}^{1/2} , \tag{3.43}$$

where

$$S_y = \sum_i w_i \left[y_i(\mathrm{obs}) - y_i(\mathrm{calc}) \right]^2 \tag{3.44}$$

is the entity that is minimised during the Rietveld refinement. Here, $y_i(\mathrm{obs})$ and $y_i(\mathrm{calc})$ are respectively the observed and calculated intensity at step i, which corresponds to a certain diffraction angle θ_i, while w_i is the corresponding weight. It is crucial to note that this index is inappropriate for comparing different experiments since a higher background will, if included in the refinement, automatically result in a lower value. Under ideal conditions it is furthermore expected that the R_{wp} should be close to the statistically expected R value, which gives a measure of the data quality and is calculated from the number of observations $N(\mathrm{obs})$ and parameters $N(\mathrm{par})$,

$$R_{\mathrm{exp}} = \left\{ \frac{N(\mathrm{obs}) - N(\mathrm{par})}{\sum_i w_i y_i(\mathrm{obs})^2} \right\}^{1/2} . \tag{3.45}$$

This condition is equivalent to requiring that the goodness-of-fit

$$\chi^2 = \frac{R_{\mathrm{wp}}}{R_{\mathrm{exp}}} \tag{3.46}$$

approaches 1. There exists an additional index that is more directly comparable to those obtained in the refinement of single crystal data, which is defined in terms of the

observed (F_{hkl}(obs)) and calculated (F_{hkl}(calc)) structure factors,

$$R_{\mathrm{F}} = \frac{\sum_{h,k,l} \left| F_{hkl}(\mathrm{obs}) - F_{hkl}(\mathrm{calc}) \right|}{\sum_{h,k,l} \left| F_{hkl}(\mathrm{obs}) \right|}. \tag{3.47}$$

Note that this value is usually not actively monitored during the refinement. The same is true for the Bragg-intensity R value, which is similar to R_{F} but compares the intensities instead of the structure factors. It should be emphasised that in general it is necessary to not only assess the agreement via difference plot and the measures listed above, but also to check that all the calculated properties and fitted parameters are physically reasonable.

3.2.3 X-ray fluorescence spectroscopy

XRF spectroscopy relies on the fact that exposure to radiation of sufficiently high energy can cause an atom to eject one of the electrons in its inner shell [137]. In turn, this leads to the formation of an unstable ionised state, from which the atom can escape via two alternative mechanisms, namely through the emission of either so called photoelectrons, which is referred to as the Auger effect [137, 138], or X-rays. In the latter case, meanwhile, an outer shell electron will replace the one that has been lost, which means that the frequency of the emitted radiation directly reflects the difference in energy between the two states. Because of the competition between these two processes the fluorescence yield will be governed by their relative effectiveness, which in both cases depends on the atomic number. As a result, the intensity can be two orders of magnitude lower for the lightest atoms, which are, therefore, harder to detect. In spite of this, XRF can be a powerful technique for performing qualitative analyses due to the fact that each element corresponds to a unique set of emission lines, which are more or less unaffected by the chemical environment since the signals originate from the electrons in the innermost shells. Because the peak heights moreover depend on the abundance of the given species within the sample, one can even obtain quantitative measures of the composition. Given the information presented above, it is evident that an XRF spectrometer must consist of a radiation source, sample holder or container, detector, as well as a data collection and processing unit. It may include additional components that are, for instance, used to modify the incoming or outgoing beams.

The interaction between the incident beam of X-ray photons and the atoms in the sample is a complex process that produces other types of radiation, for instance from coherent and incoherent scattering, which the detector will also register. For this reason, the raw signal must typically undergo a number of processing steps before it is possible extract the information of interest. Firstly, the spectrum is "corrected", which means that the analysis software attempts to identify and remove peaks that are not

due to fluorescence. The next step is to perform a qualitative analysis or, in other words, identify all the elements present in the sample through comparison with a library of reference spectra. To obtain quantitative estimates of the chemical compositions it is thereafter necessary to subtract the background, which generally stems from an overlap of instrumental noise and scattered radiation from different sources. Since a typical specimen, especially those of practical interest, contains a wide variety of different elements, this will inevitably lead to some degree of peak overlap. The final step is to deconvolute the corrected spectrum, which can be achieved by applying some type of mathematical model that represents the latter as a sum of suitable functions, such as Gaussians, or reference profiles for pure elemental specimens.

The sample preparation is the most crucial step when performing XRF spectroscopy since it has a significant impact on the quality of the measurement. While the procedure must generally be adapted based on both the nature of the material and the information that is sought, it is always advisable to ensure that the specimen actually represents the material of interest. The processing should, hence, be kept to an absolute minimum. Fortunately, very little or no preparation is required if the analysis is purely qualitative. If the aim is to obtain a quantitative estimate, however, it is crucial to meet the precise requirements of the given instrument. Typically, this means that the sample should be homogeneous and take the form of a thin compact disk with a flat and smooth surface. In this project, for instance, all XRF measurements were performed on pellets prepared by compacting powderised samples that had been mixed with a suitable binder.

3.2.4 Density functional theory

Most of the computational methods utilised in this project require sets of atomic structures as well as values of key properties, such as energy and forces, as input. This includes the generation of target data for the construction of alloy CEs (Sect. 3.2.5), extraction of IFCs (Sect. 3.1.4) as well as the BTT (Sect. 3.3.6) calculations. DFT is a standard method for generating this type of information and has been successfully applied to a wide range of different systems, from single atoms and molecules to surfaces and bulk insulators, semiconductors, and metals [124, 139, 140]. Essentially, it offers a feasible way to solve the many-body Schrödinger equation,

$$\mathscr{H}\psi = i\hbar\frac{\partial\psi}{\partial t}, \tag{3.48}$$

where $\psi = \psi(\mathbf{r}_i, \mathbf{R}_l, t)$ is a many-body wave function, which depends on the coordinates of all electrons $\mathbf{r}_i$ and nuclei $\mathbf{R}_l$ as well as time t. The Hamiltonian $\mathscr{H}$ consists of contributions from the kinetic energies of the electrons and nuclei together with Coulombic interactions. While Eq. (3.48) is practically impossible to solve, a tractable form can be obtained by applying the Hohenberg–Kohn theorems. These, specifically, state that the ground state energy E_0 can be expressed as a functional of the electron

distribution function $E_0[n_e(\mathbf{r})]$. Thus, the problem of solving Eq. (3.48) is reduced to finding the solution $n_e(\mathbf{r})$ to a single particle Schrödinger equation, which is achieved by applying a variational procedure. This is possible since the Hohenberg–Kohn theorems state that the ground state energy is minimised if $n_e(\mathbf{r})$ takes on its exact form.

The final step in the so called Kohn-Sham approach, is to assume that $n_e(\mathbf{r})$ can be represented by a sum of single particle wave functions $\phi_j(\mathbf{r})$ [124, 140],

$$n_e(\mathbf{r}) = \sum_j \left|\phi_j(\mathbf{r})\right|^2 . \tag{3.49}$$

As a result, one is left with the problem of solving the equations

$$\left(-\frac{1}{2}\boldsymbol{\nabla}^2 + v(\mathbf{r}) + e^2 \int \frac{n(\mathbf{r}')}{|\mathbf{r}-\mathbf{r}'|}\mathrm{d}\mathbf{r}' + v_{\mathrm{xc}}(\mathbf{r})\right)\phi_j(\mathbf{r}) = \varepsilon_i \phi_j(\mathbf{r}), \tag{3.50}$$

where ε_j are the eigenvalues associated with the eigenfunctions $\phi_j(\mathbf{r})$. The first three terms in Eq. (3.50) correspond to the kinetic energy, an external potential, which includes the contributions from the nuclei, and the Coulombic electron-electron interactions, respectively. While these can be readily evaluated, finding a suitable approximation for the fourth term, which accounts for exchange-correlation effects, is one of the key problems when applying DFT in practice. In this work, the calculations have almost exclusively been based on a functional that was originally developed to account for van-der-Waals forces [141, 142], but has later proven to also yield improvements for non-van-der-Waals bonded systems compared to regular exchange-correlation functionals [143].

3.2.5 Alloy cluster expansions

Since any atomic structure can be represented as a collection of clusters (Sect. 3.1.3), it is possible to decompose a given physical property Q, which can be expressed as a function of the occupation vector $\boldsymbol{\sigma}$, as a sum over the corresponding contributions [117]. This results in an expansion with the *a priori* unknown parameters J_α, which are also referred to as effective cluster interactions,

$$Q(\boldsymbol{\sigma}) = Q_0 + \sum_\alpha m_\alpha J_\alpha \boldsymbol{\sigma} \langle \Pi_{\alpha'}(\boldsymbol{\sigma}) \rangle_\alpha . \tag{3.51}$$

Here, the sum goes over all representative clusters α, each of which corresponds to a specific orbit with a multiplicity m_α, while $\langle \cdots \rangle_\alpha$ represents the average over all clusters α' that are symmetry equivalent to α. It should also be emphasised that the basis functions $\Pi_{\alpha'}(\boldsymbol{\sigma})$ are required to form an orthogonal set in order for this decomposition to be exact.

In practice, it is necessary to truncate the expansion in Eq. (3.51), which is typically done by only considering orbits up to a certain order and geometrical size. This is physically indicated since the most important interatomic interactions are typically short-ranged and only involve a handful of atoms [117]. It is, furthermore, convenient to recast the set of equations represented by Eq. (3.51) in matrix form,

$$\mathbf{Q} = \mathbf{A}\mathbf{J}, \tag{3.52}$$

where $\mathbf{J}$ and $\mathbf{Q}$ are the unknown parameters and target data, respectively. As is evident from the expression

$$A_{ij} = m_{\alpha_j} \sigma_i \langle \Pi_{\alpha_j'}(\sigma_i) \rangle_{\alpha_j}, \tag{3.53}$$

each row in the sensing matrix $\mathbf{A}$, which is often referred to as a cluster vector, is related to a specific configuration $\boldsymbol{\sigma}_i$ while the columns correspond to the various orbits α_j. Most often, $\mathbf{Q}$ is given by a set of energies that have been obtained by relaxing the associated configurations via DFT calculations (Sect. 3.2.4). The task of finding the best solution to this set of equations is effectively achieved through the application of a suitable linear regression technique (Sect. 3.2.6). To this end, the ICET software package, which has been used to construct all models employed in this work, is interfaced with different machine learning libraries [117].

3.2.6 Linear regression techniques

Since the construction of CEs (Sect. 3.2.5) and extraction of IFCs (Sect. 3.1.4) both involve solving equations of the form

$$\mathbf{y} = \mathbf{A}\mathbf{x}, \tag{3.54}$$

it is often advisable, if not necessary, to employ linear regression techniques, which are conveniently available both in the ICET [117] and HIPHIVE [144] packages. The aim is to find the solution $\mathbf{x}$ that minimises the difference $\|\mathbf{y} - \mathbf{A}\mathbf{x}\|_2$ given the reference vector $\mathbf{y}$, usually subject to additional constraints. The simplest option is to use the ordinary least squares method, which is, however, only suitable for solving overdetermined problems and prone to overfitting. Because of these drawbacks and the fact that the rows in the sensing matrix $\mathbf{A}$ are often correlated, it is generally advisable, and for underdetermined cases even necessary, to apply some kind of regularisation technique. When constructing alloy CEs it is also important to remember that the physical interactions typically decline very quickly with distance, which, in turn, leads to an expansion that is dominated by a few nonzero terms. In other words, the solution $\mathbf{x}$ is likely to be sparse.

The main benefits of regularisation are that the resulting solution is both less likely to be overfitted and more readily transferable. One of the methods that have been tested

in this project is the least absolute shrinkage and selection operator regression, which introduces a penalty term related to the l_1 norm,

$$\mathbf{x}_{\text{opt}} = \underset{\mathbf{x}}{\text{argmin}} \left\{ \|\mathbf{y} - \mathbf{A}\mathbf{x}\|_2 + \alpha \|\mathbf{x}\|_1 \right\}. \tag{3.55}$$

While easy to implement and suitable as a comparison, the fact that this method tends to select too many features means that it is often not the best choice [117, 144]. Bayesian approaches such as automatic relevance detection regression, which has been used in this project, are therefore often preferred [145, 146]. They are based on Bayes' theorem [147],

$$P(\mathbf{x}|\mathbf{y}) = \frac{P(\mathbf{y}|\mathbf{x})P(\mathbf{x})}{P(\mathbf{y})}, \tag{3.56}$$

where $P(\mathbf{x}|\mathbf{y})$ is the probability of obtaining the solution vector $\mathbf{x}$ given the target values $\mathbf{y}$, which is often referred to as the posterior distribution. The probability $P(\mathbf{y}|\mathbf{x})$ of observing $\mathbf{y}$ given $\mathbf{x}$ can typically be assumed to follow a normal distribution, while $P(\mathbf{y})$ is used for normalisation and is thus not of particular importance. This means that the minimisation problem outlined earlier corresponds to finding the solution $\mathbf{x}$ that maximises $P(\mathbf{x}|\mathbf{y})$. The trick to facilitating this process is to properly choose the prior distribution $P(\mathbf{x})$, which means adapting the mathematical representation so as to incorporate physical and chemical intuition, including the fact that the interatomic interactions tend to weaken as cluster size and order increase.

Another regularisation method that has proven to be efficient for constructing CEs is recursive feature elimination [117]. As the name suggests, this is an iterative approach that involves the following three steps [144, 148]:

- Solve the problem using a given regression technique, such as ordinary least squares.
- Rate individual elements of the solution vector.
- Remove a given number or percentage of the weakest or the least important parameters.

This procedure is repeated until the target number of features has been reached.

As a way of assessing and comparing alternative regularisation methods, it is common to calculate cross-validation scores [117, 144]. This involves splitting the available data into training and validation sets, which are respectively used for fitting the model and calculating the root-mean-square errors. For a given property Q, the latter can be expressed as

$$\text{RMSE} = \sqrt{\frac{1}{N_{\text{validation}}} \sum_i \left(Q_i^{\text{model}} - Q_i^{\text{target}} \right)^2}, \tag{3.57}$$

where the sum goes over the entire validation set of size $N_{\text{validation}}$. Additionally, it is common to repeat this process several times, which includes randomly generating new splits and finally calculating the average score.

There are, however, other more direct ways of estimating the robustness as well as accuracy of a given model and regression method. One possibility available in ICET [117], is to simultaneously construct multiple CEs (Sect. 3.2.5) based on the same sensing matrix but different training sets, which have been selected at random, with replacement. By analysing the results obtained after the sampling, one can obtain key information regarding the sensitivity of the reference data and regression method as well as the properties of interest. Another possibility, which is more appropriate for obtaining reliable error estimates for the predictions, is to sample the posterior probability distribution of the model space via MC simulations [145, 149].

3.2.7 Monte Carlo simulations

An efficient and convenient method for predicting thermodynamic averages from CE models (Eq. (3.51)) is to perform MC sampling using the Metropolis algorithm [117, 129]. This corresponds to a random walk through the space of occupation vectors, during which a particular trial step is accepted with a probability

$$P(\text{accept}) = \min\left\{1,\, \exp\left(\frac{\Delta\Psi}{k_B T}\right)\right\}. \tag{3.58}$$

Here, $\Delta\Psi$ represents the difference in the thermodynamic potential, excluding the configurational entropy, after and before the move. If a canonical ensemble is employed, which conserves the number of particles of each species N_i, the volume V as well as the temperature T, it is given by the internal energy, $\Psi = E$. In this case, a step involves selecting a pair of lattice sites and swapping the corresponding elements with probability $P(\text{accept})$.

In situations where it is convenient to allow the concentrations to vary, for instance when constructing a phase diagram, one can instead use a semi-grand canonical ensemble, which constrains the total number of atoms N as well as the difference in the chemical potential for each species relative to the first $\Delta\mu_i = \mu_i - \mu_1$ [117]. This means that each trial step involves a switch on a single site while the thermodynamic potential takes on the form

$$\Psi = E - N\sum_{i=2} c_i \Delta\mu_i, \tag{3.59}$$

where c_i is the concentration of species i. Consequently, it is possible to continuously vary the configuration and thereby integrate thermodynamic properties with respect to concentration. A problem, however, is that there is not a one-to-one correspondence

between μ_i and c_i in two-phase regions. Fortunately, there exists an alternative that does not suffer from the same drawback, namely in the form of the so-called VCSGC [150]. While the trial move is the same as when sampling the semi-grand canonical ensemble, the thermodynamical potential is not. For a binary system, it is given by

$$\Psi = E - Nk_B T\bar{\kappa}\left(c + \frac{\bar{\phi}}{2}\right)^2, \tag{3.60}$$

where the parameters $\bar{\phi}$ and $\bar{\kappa}$ act as constraints for the average and variance of the concentration c, respectively. As a result, the canonical free energy derivative can be expressed in terms of the average observed concentration $\langle c \rangle$,

$$\frac{\partial F}{\partial c} = -2Nk_B T\bar{\kappa}\left(\langle c \rangle + \frac{\bar{\phi}}{2}\right), \tag{3.61}$$

and therefore be integrated over miscibility gaps.

Regardless of which ensemble is employed, the thermodynamical average of the property of interest Q can be calculated as

$$\langle Q \rangle = \frac{\int Q(\mathbf{r}, \mathbf{p}) e^{-\varepsilon(\mathbf{r},\mathbf{p})/k_B T} \mathrm{d}p^N \mathrm{d}r^N}{\int e^{-\varepsilon(\mathbf{r},\mathbf{p})/k_B T} \mathrm{d}p^N \mathrm{d}r^N}, \tag{3.62}$$

where $\varepsilon(\mathbf{r}, \mathbf{p})$ is the total energy of the system for a particular state while $\mathbf{r}$ and $\mathbf{p}$ represent the positions and momenta of the N particles, respectively. In practice the integrals in Eq. (3.62) are replaced by a sum over the configurations that are sampled during the simulation.

Although all of the aforementioned ensembles are available via the MCHAMMER module in the ICET python package [117], it has only been deemed worthwhile to employ the canonical and the VCSGC in the present context. In particular, the former has been employed to determine key properties, such as the SOFs, for a wide range of compositions and temperatures, while the latter has been used more sparingly and mainly for the sake of calculating mixing energies. A further extension, which is also implemented in MCHAMMER, is to use a hybrid ensemble that alternates between canonical and VCSGC ensembles. In the present context, the latter was constrained to only involve a subset of the species on the active sublattice. In this way, it was possible to sample an entire range of ratios between two of three species while keeping the concentration of the third fixed, thus allowing the corresponding mixing energy to be calculated directly along iso-concentration lines.

3.2.8 Wang-Landau algorithm

A potential disadvantage when using conventional MC sampling based on the Metropolis condition is that the temperature is fixed. Consequently, multiple simulations are

required in order to capture the temperature dependence of the properties of interest. This is especially true close to a continuous phase transition, in which case the convergence can be extremely slow, and might even be practically impossible to achieve. This issue can be circumvented by employing the WL algorithm [151, 152], which has been implemented in the MCHAMMER module of the ICET package [117]. The key difference is that this method directly obtains the microcanonical density of states $\rho(E)$. Since the average of any quantity Q can be expressed as

$$\langle Q \rangle_T = \frac{\sum_E Q\rho(E)\exp(-E/k_B T)}{\sum_E \rho(E)\exp(-E/k_B T)}, \tag{3.63}$$

knowledge of $\rho(E)$ allows one to calculate a variety of different thermodynamic properties, including the internal energy

$$U(T) \equiv \langle E \rangle_T = \frac{\sum_E E\rho(E)\exp(-E/k_B T)}{\sum_E \rho(E)\exp(-E/k_B T)}, \tag{3.64}$$

the heat capacity

$$c_v(T) = \frac{\partial U}{\partial T} = \frac{\langle E^2 \rangle - \langle E \rangle^2}{k_B T^2}, \tag{3.65}$$

the free energy

$$F(T) = -k_B T \ln\left(\sum_E \rho(E)\exp\left(-\frac{E}{k_B T}\right)\right), \tag{3.66}$$

and the entropy

$$S(T) = \frac{U(T) - F(T)}{T}. \tag{3.67}$$

Since the goal is to sample the entire energy range evenly during the random walk, it is necessary to employ a specialised procedure as well as acceptance criterion [151, 152]. More precisely, one must not only keep track of the evolution of $\rho(E)$ but also count the number of times each energy interval of the preset grid has been visited, which is the task of the histogram $h(E)$. Because $\rho(E)$ can, in practice, become extremely large, and potentially exceed the upper limit of a double precision floating point number, it is convenient to update the microcanonical entropy, $S(E) = \ln(\rho(E))$, instead. The WL algorithm therefore involves updating $S(E)$ by adding a successively smaller number f, which is referred to as the "fill factor", until the latter reaches a value sufficiently close to zero. Since $f = 0$ corresponds to the ideal case, which is expected to produce the true density of states, the predefined final value on the fill factor, f_{final}, controls the accuracy.

As is illustrated in Fig. 3.8, a WL simulation generally proceeds as follows:

1. Generate an initial configuration.
2. Set f to 1 and $S(E)$ as well as $h(E)$ to 0.
3. Propose a trial step, which can either involve a swap of two sites or a switch on a single site similarly to conventional MC simulations using canonical and VCSGC ensembles, respectively.
4. Accept the move from the "current" to the "new" state with probability
$$P = \min\left\{1,\ \exp\left[S\left(E_{\text{new}}\right) - S\left(E_{\text{current}}\right)\right]\right\}. \tag{3.68}$$
5. Update the microcanonical entropy and histogram via $S(E) \leftarrow S(E) + f$ and $H(E) \leftarrow h(E) + 1$, respectively, where E is the energy of the system after the step.
6. Check whether the histogram is sufficiently flat, which corresponds to testing the criterion
$$h(E) > \chi\langle h(E)\rangle\, \forall E, \tag{3.69}$$
where χ is some predefined percentage.
7. Terminate the loop if the fill factor is smaller than the threshold, $f < f_{\text{final}}$. Otherwise, set $h(E)$ to zero, halve the fill factor, $f \leftarrow f/2$, and return to step 3.

In this work, WL simulations have primarily been employed for the purpose of identifying and characterising the transformation between an ordered and a disordered state [152]. First-order transitions lead to discontinuities in the internal energy as well as the entropy while the heat capacity is expected to display a peak, since $c_v = \partial U/\partial T$. For a continuous phase transition, the first derivative of the free energy is continuous but c_v still diverges at the transition temperature T_c [139, 153],
$$c_v \propto \begin{cases} (T - T_c)^{\alpha} & , T > T_c \\ (T_c - T)^{\alpha'} & , T < T_c \end{cases}. \tag{3.70}$$
In other words, the heat capacity allows one to assess phase transitions, regardless of their order.

3.2.9 Extraction of representative structures

Calculations of key properties related to thermal (Sect. 3.1.4, Sect. 3.1.5, Sect. 3.1.7, Sect. 3.1.8) and electronic (Sect. 3.3.6) transport requires suitable representative structures, which can be conveniently generated via the CE (Sect. 3.2.5) for the corresponding system. In practice, these can either correspond to a unique ground state or represent the average configuration at a finite temperature.

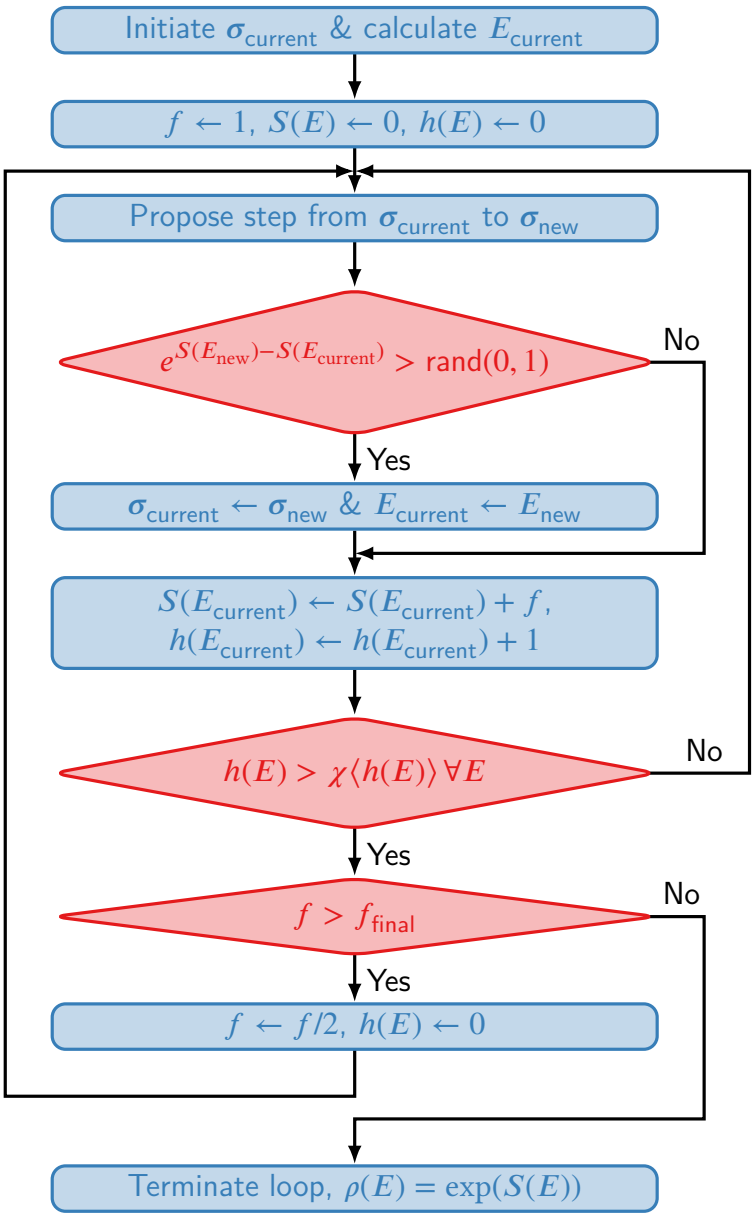

Figure 3.8: Flow chart that describes the main steps in a WL simulation.

A conventional way of obtaining the former is by simulated annealing. This typically involves running a series of MC (Sect. 3.2.7) calculations at successively lower temperatures, which should mean that the sampled states approach the configuration that corresponds to the global energy minimum. While there is a risk that a given run becomes trapped in a local minimum, this risk can be mediated through repetition. Since the sampling becomes increasingly inefficient with decreasing temperature, another

possibility, which has been employed in this project for all pseudo-ternary systems, is to assume that the ground state corresponds to the configuration with the lowest energy among those that have been sampled during the entire simulation.

A more elegant solution for pseudo-binary cases, which has been implemented in the ICET package [117], is to use a procedure based on mixed integer programming [154]. The basic principle for this approach is that the problem of constructing a CE (Sect. 3.2.5) can be reformulated by transforming the point functions that describe the occupation of the lattice point, which can take on the value of -1 or 1 (for a pseudo-binary system), to a binary variable $x \in \{0, 1\}$. In particular, this means that the new objective is to find the vector $\boldsymbol{\sigma}'$ such that $\mathbf{J}' \bullet \boldsymbol{\sigma}'$ is minimised, where J_i' is the "cost" associated with the independent variable σ_i', while subject to a number of constraints. Here, the J_i are the transformed effective cluster interactions so that the solution $\boldsymbol{\sigma}'$ represents the configuration that gives the lowest total energy.

The generation of special quasi-ordered structures is yet another technique for finding representative configurations at finite temperatures [155]. The first step of this procedure is to determine a target cluster vector by averaging over the configurations sampled during an MC simulation (Sect. 3.2.7) at the temperature of interest. Next, a cost function is defined that reflects the deviation from the target cluster vector. The resulting minimisation problem can, in practice, be solved by running a simulated annealing where the acceptance probability depends on the change in cost associated with the trial move.

3.3 Characterising the electronic transport

While determination of the power factor only requires knowledge of the electrical conductivity and the Seebeck coefficient, more elaborate investigations are required in order to understand its structural and compositional dependence, which is necessary in order to optimise the performance. In Paper II and Paper VII, we, therefore, use the measurements of the former properties (Sect. 3.3.2) to calculate the weighted mobility (Sect. 3.3.4). Since the aim of Paper II was to provide evidence that the prepared samples were modulation doped, such measurements were performed on both spark plasma sintered (Sect. 3.3.1) pellets and a Czochralski-pulled single crystal (Sect. 3.2.1). As a further validation, we investigate the microstructure of the former using scanning electron microscopy (Sect. 3.3.5).

As shown in Fig. 3.9, we have also calculated electronic transport properties using BTT (Sect. 3.3.6) based on representative structures (Sect. 3.2.9) generated with help of CE models (Sect. 3.2.5). In Paper III, Paper VI, and Paper VII, the latter took the form of of ground states as well as high temperature configurations extracted from MC simulations (Sect. 3.2.7). Since the data typically include results for a range of different doping levels and furthermore do not account for electron scattering, a fitting procedure based

on experimental data was employed to extract effective electronic lifetimes. Though the procedure described thus far can yield key information regarding the relationship between the composition and the thermoelectric performance, which is the main goal of Paper VI, additional steps were performed in Paper III and Paper VII for the purpose of determining the origin of the observed differences between the ordered and disordered states, which included a comparison of the corresponding band structures.

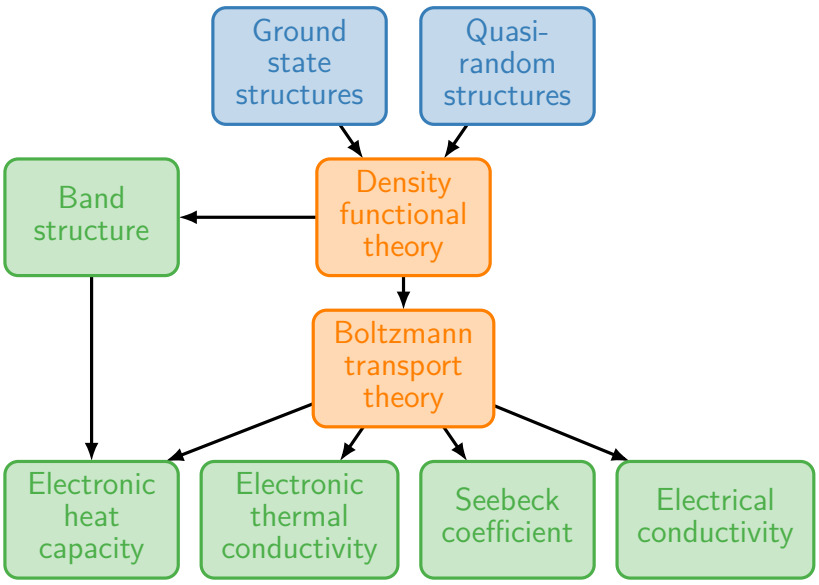

Figure 3.9: Conceptual illustration of the procedure for calculating key properties related to electronic transport via atomic scale simulations. Here, methods, input/output data and final results have respectively been coloured in orange, blue, and green.

3.3.1 Spark plasma sintering

Since the materials obtained via conventional solid state synthesis methods (Sect. 3.2.1) are typically in the form of powders or polycrystalline ingots with relatively poor mechanical properties, they must be consolidated into dense pellets before their properties can be determined. While this issue could potentially be avoided by growing single crystals (Sect. 3.2.1), producing large enough samples and machining them into suitable shapes is not always feasible. While not an absolute requirement, the first step is to ensure that the powder has been properly homogenised, for example via sieving, to ensure that the grain sizes fall within a suitable range. Though there exist many different consolidation techniques, SPS is the only one that has been employed in this work.

In preparation for sintering, the powder is typically sandwiched between two punches within a cylindrical die, designed so that the former fits neatly into the hole of the latter.

As shown in Fig. 3.10, the die-punch assembly is then placed in a chamber, which is subsequently sealed and either completely evacuated or filled with an inert gas, before being brought into contact with an upper and lower electrode. Next, a pulsed direct current is applied that will flow through the die and punches, since these are made of a electrically conductive material, as well as the sample, as long as it is not completely insulating. Thanks to the fast heating rates that can thus be achieved, the powder can be fully compacted into pellets with densities above 97 % within a few minutes. Moreover, the micro- and nanostructure is largely preserved, due to the limited grain growth that can take place within this relatively short time frame.

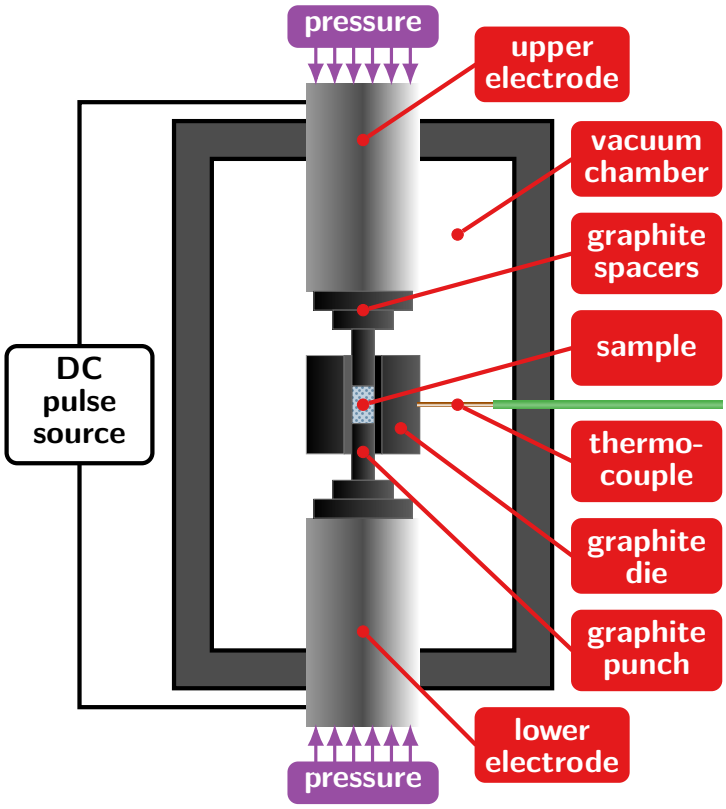

Figure 3.10: Sketch of an SPS machine.

The punches and die as well as the spacers, which are situated between the former and the electrodes, are usually made of graphite [132]. Additionally, it is common to cover all interfaces between the tools and the powder with graphite sheets, in order to avoid unwanted reactions as well as interdiffusion. During the experiment itself, there are, in principle, three tunable parameters, namely time, temperature, and pressure. Though the final density will suffer if any of latter two are too low, there is also an upper limit above which there is an increased risk for the powder to melt or decompose. Because of this fact and since pronounced atomic diffusion is almost always undesirable,

the general recommendation is to set the sintering temperature to about 70 % of the melting or decomposition point. The cooling step should also be considered since the manner in which the pressure is released has a direct impact on the rate at which the temperature drops, especially under vacuum conditions, and, thereby, the degree of residual strain. Another important aspect to consider is that the current flow through the powder, if the latter is sufficiently conductive, can become high enough to cause unwanted effects, such as extreme local heating and electromigration. For sensitive compounds and in cases where grain coarsening is not an issue, both of which apply for the materials of interest in this project, it can, hence, be advisable to insulate the sample from the punches, for instance via the application of boron-nitride spray.

3.3.2 Electronic transport measurements

Since optimising the power factor, σS^2, is key for achieving a high thermoelectric performance, it is crucial to be able to accurately measure both the electrical conductivity σ and the Seebeck coefficient S. In this work, this has been achieved with help of an ULVAC ZEM3 apparatus, which is widely used within the thermoelectric research community. One of the key features is that it employs a four-probe setup, which allows both σ and S to be measured simultaneously. The Seebeck coefficient measurement is performed under a steady state condition based on the well-established differential method [132]. This means that the sample, as illustrated in Fig. 3.11, is squeezed between an upper and lower electrode. These are, in this context, used to establish a small temperature gradient $\Delta T = T_2 - T_1$ between the two probes, which have been brought in contact with two points on the lateral surface. The resulting potential difference $\Delta V = V_2 - V_1$ can then be used to calculate the Seebeck coefficient, at the average temperature $T = (T_2 + T_1)/2$, as

$$S = \frac{\Delta V}{\Delta T}. \tag{3.71}$$

It is, however, generally not advisable to base the result on a single value. A more reliable estimate can be obtained via linear regression, given that the measurement is repeated for a range of different gradients. For instance, this eliminates the effect of a possible voltage offset.

Although it has been debated whether a four-probe or two-probe arrangement is the most accurate for determining the Seebeck coefficient, it is a well established fact that the former is advantageous when measuring the electrical conductivity [132]. Two of the main issues that can thereby be avoided are particularly relevant for thermoelectric materials. Specifically, this includes the Seebeck voltage contribution from the temperature gradient as well as the Peltier heating of the contacts caused by the voltage difference. When using the four-probe bipolar technique the former can, however, be avoided by flipping the current direction and using the average bipolar voltage V

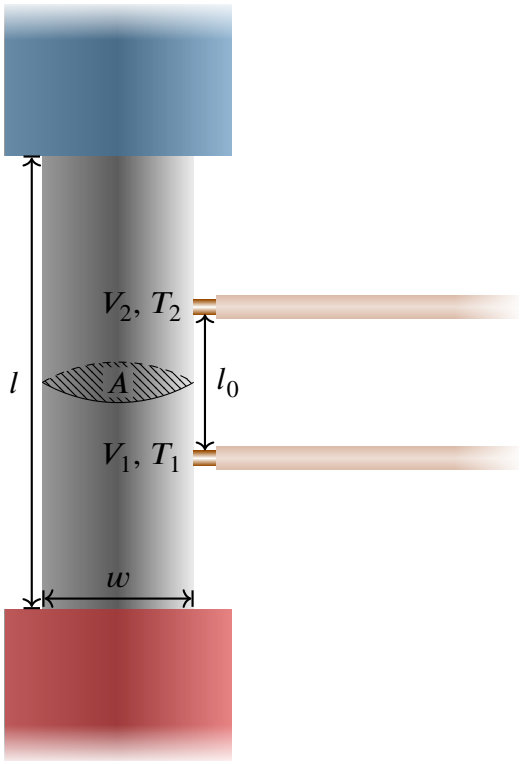

Figure 3.11: Illustration of a four-probe setup for the simultaneous measurement of electrical conductivity and Seebeck coefficient.

when calculating the resistivity via

$$\rho = \frac{V}{I}\frac{A}{l_0}, \tag{3.72}$$

where I is the current, A the cross-sectional area of the sample and l_0 the distance between the two contacts. If this switch is performed quickly enough, it is moreover possible to reduce the error resulting from the Peltier effect since a finite time is required for the heat, which is thereby generated, to diffuse between the contacts. It is generally recommended that the length l and thickness w of the rod-like sample satisfy the criterion

$$l - l_0 \leq 2w, \tag{3.73}$$

to ensure that the current flow between the voltage contacts is consistent.

3.3.3 Electronic thermal conductivity

As mentioned in Sect. 1.2, the electronic contribution to the thermal conductivity is often estimated based on the Wiedemann-Franz law, $\kappa_e = L\sigma T$ [9]. Furthermore,

it is common not only to assume that the Lorenz number, L, is a constant but also equal to $\frac{\pi^2}{3}\left(\frac{k_B}{e}\right) \approx 2.44 \times 10^{-8}\,\mathrm{W\,\Omega\,K^{-2}}$, which is only strictly valid for free electrons. It can thus only be regarded as a reasonable approximation for metals and heavily doped (degenerate) semiconductors. In fact, experimental measurements indicate that for low doping levels (non-degenerate semiconductors) the value can be as low as $1.5 \times 10^{-8}\,\mathrm{W\,\Omega\,K^{-2}}$. While it is possible to obtain a much more accurate estimate from calculations based on the Boltzmann transport theory Sect. 3.3.6, this solution is not always convenient. Yet it been shown that a better agreement, compared to setting $L = 2.44 \times 10^{-8}\,\mathrm{W\,\Omega\,K^{-2}}$, can be achieved by using the following empirical expression [9],

$$L = 1.5 + \exp\left(\frac{S}{116}\right), \tag{3.74}$$

which has been found to give a reasonable accuracy (20 %) for a range of different thermoelectric materials.

3.3.4 Weighted mobility

The mobility is a fundamental property for characterising the carrier transport in semiconducting materials and a key parameter to consider when developing electronic devices [156]. According to the Drude-Sommerfeld model, which assumes that a metal can be treated as a gas of non-interacting electrons that are randomly scattered by the ionic cores yet follow Fermi-Dirac statistics [124], the former is directly proportional to the drift mobility μ,

$$\sigma = n\mu q_e, \tag{3.75}$$

where n is the carrier concentration and q_e the electronic charge. In practice, it is common to approximate μ with the hall mobility μ_{H}, since it can be more readily determined. One of the limitations of Hall measurements, however, is that these are difficult to perform at high temperatures. Under such conditions, the weighted mobility μ_{w} is a more appropriate estimate since it can be directly calculated from the resistivity and the Seebeck coefficient. This property can be interpreted as the mobility weighted by the density of states, which means that it, contrary to μ, does not depend on the carrier concentration.

By applying the free electron model described above and additionally assuming that the mean-free-path is constant, it is possible to derive a system of equations from which

the weighted mobility can be determined [156],

$$\sigma = \frac{8\pi q_e \left(2m_e k_B T\right)^{3/2}}{3h^3} \mu_{\mathrm{w}} \ln\left(1 + e^{\eta}\right), \tag{3.76}$$

$$S = \frac{k_B}{q_e} \left[\int_0^{\infty} \frac{\varepsilon}{1 + e^{\varepsilon - \eta}} \mathrm{d}\varepsilon \Big/ \ln\left(1 + e^{\eta}\right) \right]. \tag{3.77}$$

Here, h is Planck's constant while $\eta = \varepsilon_{\mathrm{F}}/k_B T$ represents a reduced version of the Fermi level ε_{F}. Since Eq. (3.76) cannot be solved exactly, it is convenient to define an approximate semi-empirical expression by combining the solutions for $\eta \ll 0$ and $\eta \gg 0$, which represent the limiting cases of non-degenerate and degenerate semiconductors, respectively,

$$\mu_w = \begin{cases} \exp\left(\frac{k_B}{q_e}|S| - 2\right), & \eta \ll 0 \\ \frac{3}{\pi^2}\frac{k_B}{q_e}|S|, & \eta \gg 0 \end{cases}. \tag{3.78}$$

Specifically, these are added together after being divided by a sigmoid function,

$$\mathcal{S}(x) = 1 + \exp\left(ax - b\right), \tag{3.79}$$

where $x = k_B|S|/q_e$ while the parameters a and b have been empirically determined so as to ensure that the approximate and exact solutions differ by no more than 3 %. In the end, this gives the following formula for the weighted mobility:

$$\mu_{\mathrm{w}} \approx \frac{3h^3\sigma}{8\pi q_e \left(2m_e k_B T\right)^{3/2}} \left[\frac{\exp\left(\frac{k_B}{q_e}|S| - 2\right)}{1 + \exp\left(-5\frac{k_B}{q_e}|S| - 1\right)} + \frac{\frac{3}{\pi^2}\frac{k_B}{q_e}|S|}{1 + \exp\left(5\frac{k_B}{q_e}|S| - 1\right)} \right]. \tag{3.80}$$

3.3.5 Scanning electron microscopy

Electron microscopy is widely used for investigating the micro-, meso- and nanostructures of materials [135, 138]. This includes characterisation of the morphology and grain size distribution in polycrystalline samples as well as examination of defects and detection of variations in the elemental composition. Scanning and transmission electron microscopes are among the most common variants. Yet only the former type of instrument has been utilised in this project. In either case, the basic principle is similar to that of their optical analogue. A key difference, however, is that the electron beam, which is commonly generated through the heating of tungsten or LaB_6 filament, is focused on the sample using magnetic fields rather than glass lenses. In addition, the

resolution is several orders of magnitude greater, due to the significantly shorter wavelengths of electrons compared to visible light, which means that features with dimensions as small as 0.1 nm can potentially be distinguished. What is, moreover, unique for a scanning electron microscope is that the image is built up by raster scanning the electron beam across the sample.

As the incoming electrons first decelerate and then impinge on the sample, various different scattering events occur, which lead to a transfer of energy to the material [135, 138]. Of the many signals that are thereby produced, only three are generally collected, via suitably designed and oriented detectors. As indicated by the illustration in Fig. 3.12, this includes the so-called secondary electrons, which have low energies and originate from a few Ångström thick layer below the surface. These are the most important for imaging purposes, since the phase contrast is mainly provided by the slope of the surface from which the electrons originate. In fact, the yield is higher for regions with a sharper inclination, which includes edges, because the projected volume is larger compared to a horizontal surface. Backscattered electrons meanwhile have much higher energies because these have been produced via elastic scattering. Crucially, elements with higher atomic numbers will have larger cross sections, thereby increasing the chance for such events. The escape depth is in addition more significant than for the secondary electrons, which means that the images produced with the backscattered signal provide less topological information but mainly convey mass contrast. Since the physical processes at the irradiated surface are similar to those that occur in the vacuum tubes typically found in, for instance, X-ray diffraction instruments (Sect. 3.2.2), X-rays will also be generated. The corresponding signal, which is termed energy dispersive X-rays, can be used to determine the chemical composition across the area of the specimen. In particular, this is due to the fact that the energy of the radiation depends on the nature of the element from which it originates while the count reflects the relative abundance.

3.3.6 Boltzmann transport theory for electrons

Since electrical conductivity and Seebeck coefficient as well as the electronic contribution to the thermal conductivity are of particular interest for thermoelectric research, it is crucial to have a reliable method for predicting these properties via first principles calculations. BTT offers this possibility and has been successfully applied to model the electronic transport in a wide range of materials. The implementation in the open source BoltzTraP2 [10] code, which has been utilised in this project, invokes two crucial approximations. This includes the rigid band approximation, meaning that the band structure is assumed to be independent of both the doping level and the temperature. In addition, it relies on the single-mode RTA, which states that the scattering rate is proportional to $-\tau^{-1}$ where τ is the so called relaxation time [124]. Under these conditions, the electrical conductivity σ, the Seebeck coefficient S, and electronic contribution to

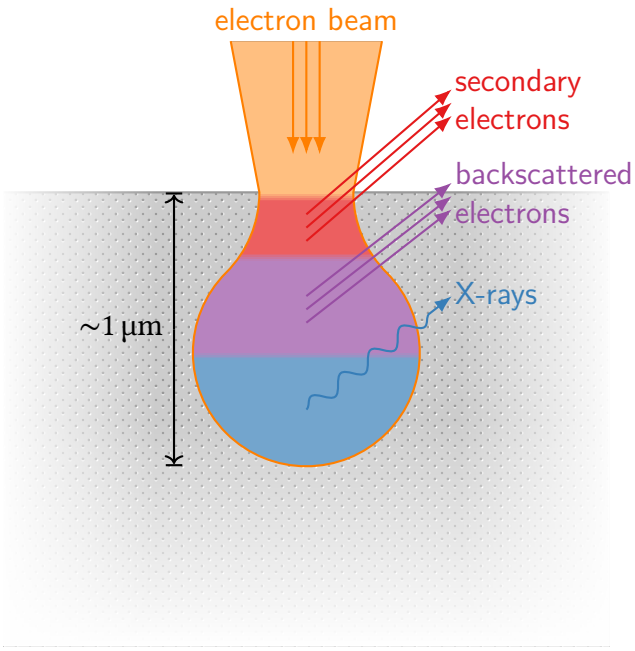

Figure 3.12: Depiction of the interaction between incident beam and material surface during electron microscopy. Because of the multitude scattering processes that take place when the incoming electrons impinge on the sample, a wide variety of different signals is produced. Typically, however, only three are collected, namely secondary and backscattered electrons as well as X-rays. When assessing the resulting data it is important to keep in mind that each originates from a volume at a certain depth from the surface.

the thermal conductivity κ_e are given by the following expressions:

$$\sigma = \mathscr{L}^{(0)}, \tag{3.81}$$

$$S = \frac{1}{q_e T} \frac{\mathscr{L}^{(1)}}{\mathscr{L}^{(0)}}, \tag{3.82}$$

$$\kappa_e = \frac{1}{q_e^2 T} \left[\frac{\left(\mathscr{L}^{(1)}\right)^2}{\mathscr{L}^{(0)}} - \mathscr{L}^{(2)} \right], \tag{3.83}$$

which have been written in terms of the generalised transport coefficients

$$\mathscr{L}^{(\alpha)}(\mu; T) = q_e^2 \int \Xi(\varepsilon, T)\, (\varepsilon - \mu)^\alpha \left(-\frac{\partial f(\varepsilon; \mu, T)}{\partial \varepsilon} \right) \mathrm{d}\varepsilon, \tag{3.84}$$

where the energy, chemical potential, elemental charge, and temperature are represented by ε, μ, q_e, and T, respectively. Here,

$$\Xi(\varepsilon, T) = \int \sum_b \boldsymbol{v}_{b,\boldsymbol{k}} \otimes \boldsymbol{v}_{b,\boldsymbol{k}} \tau_{b,\boldsymbol{k}} \delta\left(\varepsilon - \varepsilon_{b,\boldsymbol{k}}\right) \frac{\mathrm{d}\boldsymbol{k}}{8\pi^3}, \tag{3.85}$$

is the transport distribution function, which depends on both the group velocities $\boldsymbol{v}_{b,\boldsymbol{k}}$ and the relaxation times $\tau_{b,\boldsymbol{k}}$ associated with each band b and wave vector $\mathbf{k}$. It should also be noted that the electrons follow the Fermi distribution function

$$f(\varepsilon; \mu, T) = \frac{1}{e^{(\varepsilon-\mu)/k_B T} + 1}, \tag{3.86}$$

where μ is the electron chemical potential. It is also interesting (Paper VIII) to consider the electronic contribution to the heat capacity $\Delta c_v^{\mathrm{elec}}$, which can be expressed as

$$\Delta c_v^{\mathrm{elec}} = \int_0^\infty \rho_e(\varepsilon)\,(\varepsilon - \mu) \left(-\frac{\partial f(\varepsilon, \mu, T)}{\partial T}\right) \mathrm{d}\varepsilon, \tag{3.87}$$

where ρ_e is the electron DOS.

As evident from (3.85), the mode specific relaxation times must be known in order to calculate the transport coefficients. A radical yet useful assumption is to neglect this mode dependence, which is commonly referred to as the constant RTA. As a result, τ effectively disappears from the expression for the Seebeck coefficient, which can hence be used to fit the doping level through comparison with experimental data [10]. All BTT calculations in this project have been based on this assumption, since it has been shown to provide a reliable description of a similar system [11], provided that the temperature variation is taken into account, specifically by setting

$$\tau_{b,\boldsymbol{k}} \approx \tau_{\mathrm{eff}} = \tau_{300\,\mathrm{K}}(300\,\mathrm{K}/T)^a, \tag{3.88}$$

where the unknown parameters $\tau_{300\,\mathrm{K}}$ and a are fitted so as to give the best match between the predicted and measured electrical conductivity.

It is worth noting that BTT can only be expected to yield accurate results if there is a reasonable agreement between the calculated and experimentally determined band gaps. Unfortunately, it is a well known fact that these are often severely underestimated by conventional DFT functionals, which, consequently, leads to unreliable estimates of the transport properties [157, 158]. A solution, which has proven to be fairly efficient, is to apply a so called "scissor" operator. In essence, this corresponds to rigidly shifting the unoccupied conduction bands, while ensuring that the structure is otherwise preserved, so that the band gap becomes equal to some reference value, obtained either from experiments or via a more accurate computational method.

4

Summary of the results

The research efforts in this PhD project have concerned the three fundamental questions regarding inorganic clathrates introduced in Chap. 2:

- Why is the lattice thermal conductivity intrinsically low?
- What is the impact of chemical ordering on the physical properties?
- How can the electronic transport be optimised?

The following discussion will focus on these aspects one at a time with the aim of showing how the different papers have helped address each specific issue. This interrelationship is illustrated in Fig. 4.1, which shows that each paper is related to either one or two of the above questions[1].

4.1 Explanation for the low lattice thermal conductivity

As mentioned in Sect. 2.1, the understanding of thermal transport in inorganic type I clathrates has significantly improved in recent years thanks to a combination of advanced theoretical and experimental studies. The calculations performed in Paper I and Paper V verified these conclusions and additionally demonstrated the usefulness of multiple computational methods that had previously not been applied to these systems. In

[1]Although both Paper II and Paper VII involved thermal conductivity measurements, the main aim of these studies has been to evaluate and optimise the thermoelectric performance, with particular emphasis on the electronic transport properties, rather than explaining the low thermal conductivity.

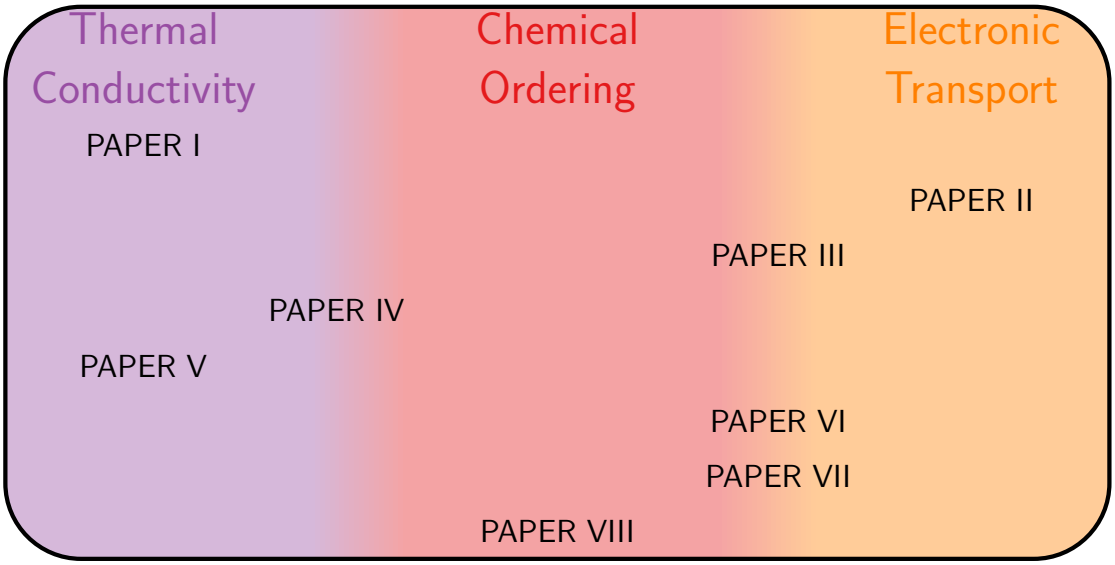

Figure 4.1: Illustration showing how the different papers are related to the three main questions that are the focus of this thesis: (i) *Why is the lattice* ***thermal conductivity*** *intrinsically low?* (ii) *What is the impact of* ***chemical ordering*** *on the physical properties?* (iii) *How can the* ***electronic transport*** *be optimised?*

particular, we find that calculations performed using either BTT combined with temperature dependent IFCs (Paper I) or HNEMD (Paper V) simulations based on fourth order models provide almost perfect agreement with experimental data, as is evident from Fig. 4.2. This is especially true when we correct for the discrepancies that result when the Wiedemann-Franz law is used to extract the lattice contribution from the measured thermal conductivity. It should also be emphasised that the BTT calculations, which only include static second and third order IFC, significantly underestimate the lattice thermal conductivity. The same models also predict that the temperature variations should follow a $\sim T^{-1}$ trend, even though the temperature dependence is in reality weaker and closer to $\sim T^{-0.7}$. It is thus crucial to account for the renormalization of the phonon modes due to phonon-phonon scattering.

By calculating and comparing both the phonon dispersion and life times, in Paper I, we were able to identify the origin of the observed discrepancies. Specifically, this analysis allowed us to conclude that the use of static IFCs leads to an underestimation of the rattler modes and thus a reduced Brillouin zone volume as well as a more significant dampening, as reflected by the reduced lifetimes. Another interesting aspect to consider is how the different phonon modes contribute to the thermal transport. This was achieved by calculating the DOS as well as the accumulated (Paper I) and spectrally decomposed (Paper V) lattice thermal conductivities. As can be seen from Fig. 4.3, a comparatively large contribution stems from low frequency modes, since

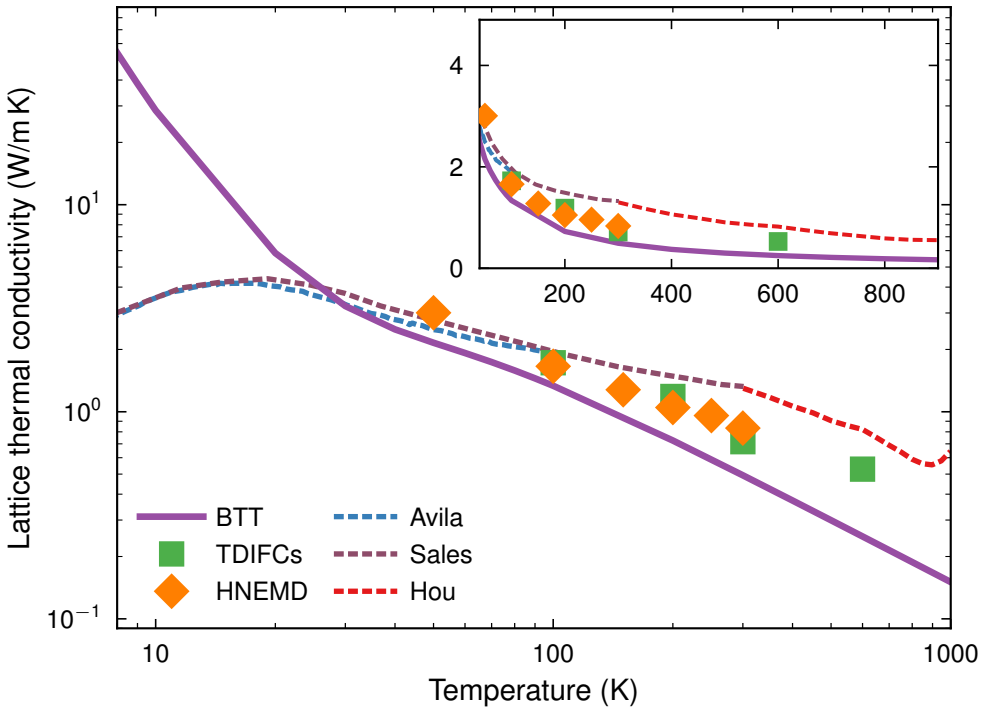

Figure 4.2: Lattice thermal conductivity of $Ba_8Ga_{16}Ge_{30}$ as a function of temperature from simulations and experiments on single-crystalline n-type samples [40, 87, 159]. The inset shows the same data when using a linear scaling of the axes. The BTT and HNEMD data have been obtained in Paper V. The results based on temperature-dependent interatomic force constants (TDIFCs) are from Paper I.

the integrated spectral thermal conductivity reaches 50 % of the total value already at 12 meV. Another interesting observation is that the sharp rise at about 3 meV matches the main peak in the phonon DOS for the Ba atom at the 6*d* site. Specifically, this can be seen as an indication of the profound influence that the guest atom in the large cage has on thermal transport. Further conclusions can be drawn when these results are compared with the predicted group velocities, which as shown in Paper I are highest in the regions $\omega \lesssim 3$ meV and 12 meV $\lesssim \omega \lesssim 16$ meV. This helps explain the peaks in the spectral thermal conductivity as well as the sharp rise in the integrated value that can be observed in the same intervals. The fact that the height of the peak in the former property at ~ 3 meV drops significantly with temperature while the phonon DOS is virtually unchanged, furthermore indicates that the concomitant decrease in the lattice thermal conductivity is mainly due to a successively lower contribution from the vibrational modes associated with the motion of Ba atoms on 6*d* sites.

Though the studies in Paper I and Paper V have mainly focused on stoichiometric

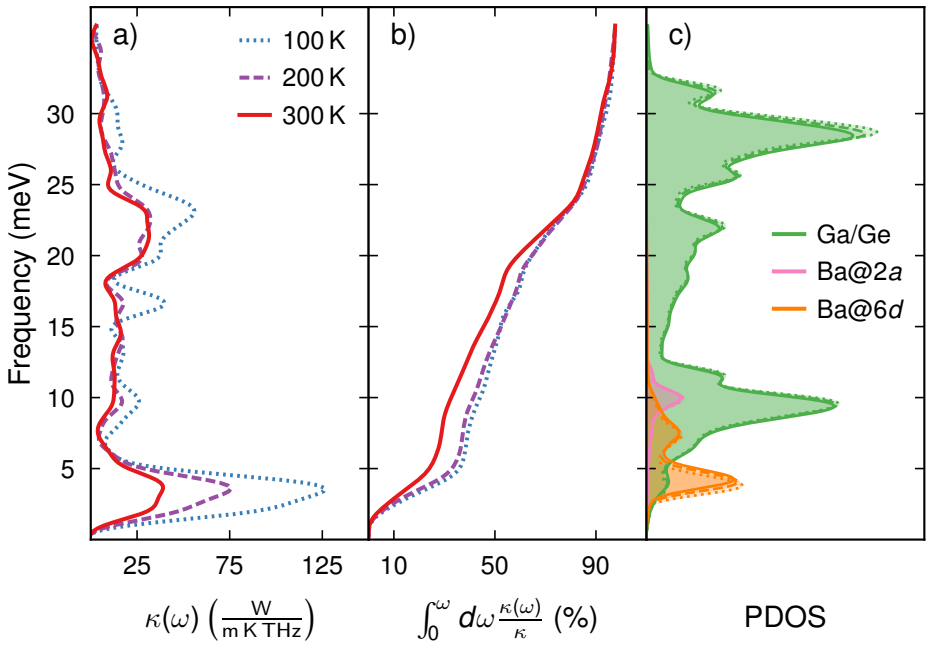

Figure 4.3: (a) Spectral decomposition according to Eq. (3.39), (b) relative integrated spectral thermal conductivity, and (c) phonon DOS of $Ba_8Ga_{16}Ge_{30}$.

$Ba_8Ga_{16}Ge_{30}$, the former study also included an analysis of the phonon frequencies associated with the Ba atom at the 6*d* site for a range of different $Ba_8Ga_xGe_{46-x}$ and $Ba_8Al_xSi_{46-x}$ compositions. This revealed that these tend to soften as x increases in the latter case and remain almost constant for the former, which we attribute to the fact that the concomitant expansion of the unit cell is more significant for $Ba_8Al_xSi_{46-x}$. Even so, the variations are relatively low compared to the standard deviations, suggesting that the overall conclusions drawn from the detailed study of $Ba_8Ga_{16}Ge_{30}$ should be applicable for a wider ranger of clathrate compounds. Yet our experimental investigation presented in Paper IV indicates that there are significant differences between $Ba_8Al_xGa_{16-x}Ge_{30}$ single crystals that have been synthesised using the Czochralski and flux methods, respectively. In particular, we find that the Czochralski-pulled sample exhibit much smaller atomic displacement parameters and, therefore, agree better with reference data for on-centre $Ba_8Ga_{16}Ge_{30}$ and $Ba_8Al_{16}Ge_{30}$. Not only is the opposite is true for the flux-grown crystallites, a comparison between the calculated and measured SOFs also indicate that these are more disordered. This suggests that chemical ordering can in fact have an impact on the lattice dynamics and, by extent, the thermal conductivity. The fact that the static disorder parameter associated with the Einstein model (Sect. 3.1.6) is significantly lower for the Czochralski crystal corroborates this hypothesis.

Based on the results presented above, it can be concluded that the recent advances in the development of computational methods have made it possible to accurately model thermal transport in inorganic clathrates, which not only yields predictions that are in good agreement with experimental data but also help reveal the physical origin of the intrinsically low lattice thermal conductivity. In fact, the research community is presumably on the verge of reaching a consensus, since both calculations and experiments seem to indicate that this is mainly due to the hybridisation of the host and guest modes, which in turn affects lifetimes, group velocities as well as phase space volume associated with propagating modes. What is still lacking, however, is a full understanding of the mechanisms that govern whether a given system displays a glass-like or crystalline behaviour. Though our studies have not provided any definitive answer to this question, we have been able to obtain some evidence indicating that this could be due to differences in the degrees of chemical ordering, which will be further discussed in the next section.

4.2 Impact of chemical ordering on physical properties

As discussed in Sect. 2.2, there exist several recent computational studies that have shown the importance of chemical ordering in inorganic clathrates. A key contribution that we have made is to prove the existence of order-disorder transitions in a variety of different systems (Paper VI), specifically $Ba_8Ga_xGe_{46-x}$, $Ba_8Ga_xSi_{46-x}$, $Ba_8Al_xGe_{46-x}$, and $Ba_8Al_xSi_{46-x}$. As can be seen from the heat maps in Fig. 4.4, these predictions are consistent with earlier experimental studies, in the latter two cases even on a quantitative level. Crucially, the variations in the SOFs mirror the temperature and composition dependence of the contribution to the heat capacity from disorder, shown in Fig. 4.5 and Fig. 4.4, respectively. Another interesting observation, which is the most evident for $Ba_8Al_xSi_{46-x}$, is that there are three separate regions corresponding to different degrees of chemical ordering. In particular, we observe a highly ordered state at low temperature and low Al content (bottom left hand corner of Fig. 4.5a), since the occupation of, for instance, the 6*c* sites deviates significantly from $16/46 \approx 35\,\%$, which is the value expected for a fully random distribution. When the number of Al atoms is increased (upper left hand corner of Fig. 4.5a), the 6*c* SOF drops significantly indicating that the configuration has become semi-disordered. While a rise in temperature does not immediately lead to a corresponding change in the composition, there is a significant shift in the SOFs at all sites as the system undergoes a transition to the disordered high-temperature state (right side of Fig. 4.5a).

In Paper III we not only show that our calculations for $Ba_8Al_xGa_{16-x}Ge_{30}$ yield results similar to those obtained for the pseudo-binary systems, but also confirm these

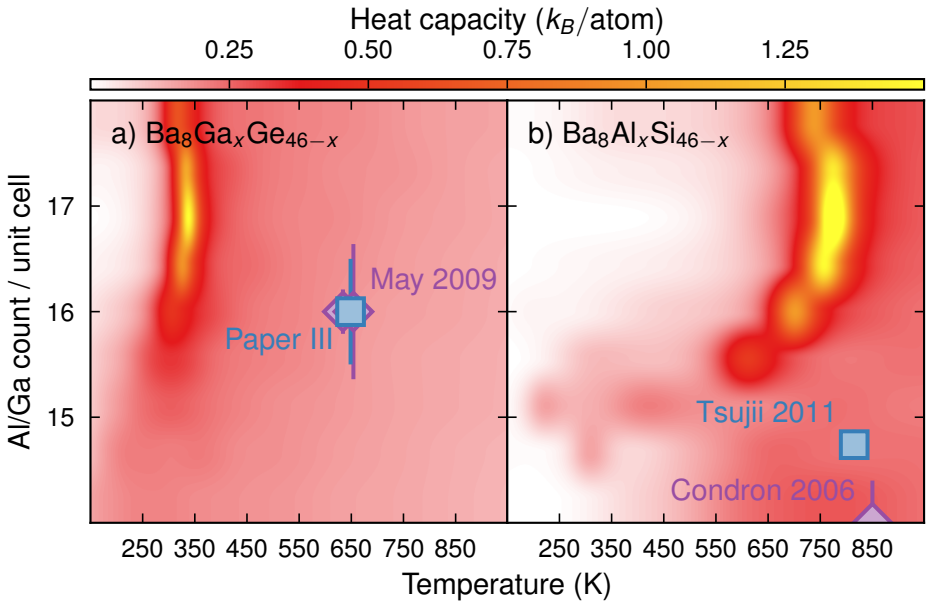

Figure 4.4: Heat maps showing the temperature and composition dependence of the contribution to the heat capacity from disorder for $Ba_8Ga_xGe_{46-x}$ (a) and $Ba_8Al_xSi_{46-x}$ (b). In the latter, transition temperatures that have been extracted from Refs. [25] (purple diamonds in a), [160] (purple diamonds in b), and [80] (blue square in b) as well as the experiments reported in Paper III (blue square in a) are also indicated.

predictions via heat capacity measurements on a Czochralski-pulled $Ba_8Al_5Ga_{11}Ge_{30}$ single crystal. Moreover, this study reveals that the order-disorder transition has a direct impact on the electronic transport properties, as discussed further in the next section. Additionally, the heat capacity measurements reported in Paper VII show that flux-grown $Ba_8Al_xGa_{16-x}Ge_{30}$ undergoes the same type of transformation. Our structural characterisation of the same samples, which is detailed in Paper IV, furthermore provided convincing evidence that flux-growth leads to a more disordered state than the Czochralski method. This is evident from the plot of the calculated and measured SOFs in Fig. 4.6, which also includes reference data for arc-melted $Ba_8Al_xGa_{16-x}Ge_{30}$. It is especially interesting to note that the SOFs for the flux-grown and Czochralski-pulled crystals agree better with the simulated disordered (1200 K) and semi-ordered (500 K) states, respectively. As was mentioned in the previous section, this suggests that chemical ordering is, at least in part, responsible for the observed differences in the off-centring of the guest atom in the large cage.

While Paper III and Paper VI have a strong emphasis on the order-disorder transition, most of our studies have to some extent taken chemical ordering into account, since we are convinced that this is crucial for understanding this group of materials. In

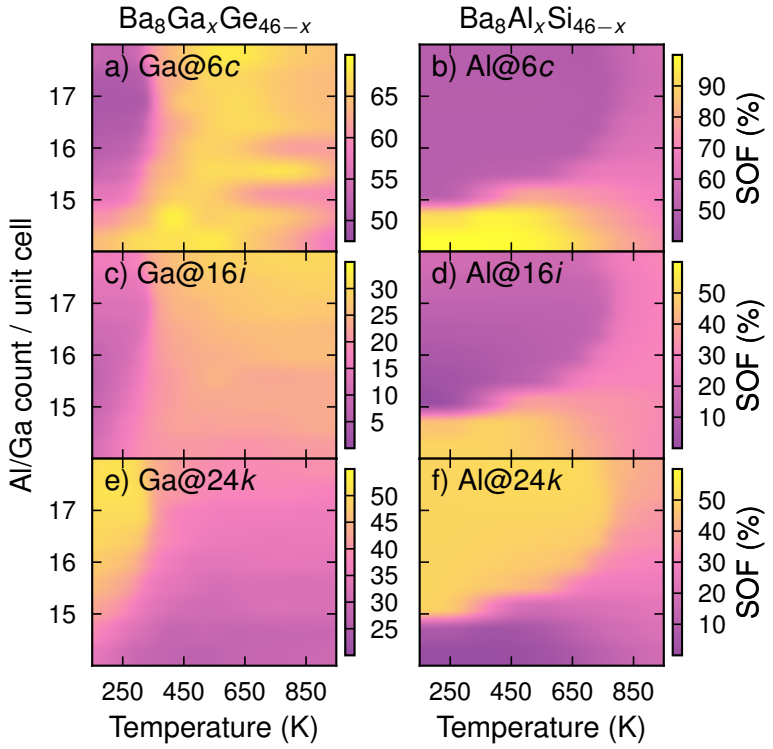

Figure 4.5: SOFs as functions of temperature and composition for Al/Ga atoms at the 6*c* (a,b), 16*i* (c,d), and 24*k* (e,f) sites for $Ba_8Ga_xGe_{46-x}$ (a,c,e) and $Ba_8Al_xSi_{46-x}$ (b,d,f).

Paper VIII, for instance, we have mapped the SOFs for both $Ba_8Al_xGa_yGe_{46-x-y}$ and $Ba_8Ga_xGe_ySi_{46-x-y}$ across a wide range of different compositions. As is revealed by the ternary diagrams in Fig. 4.7, the former system displays a pronounced non-linear behaviour. This is particularly evident from the Al SOF, which shows a very strong preference for the 6*c* site. The fact that the variations of the Ge and Si occupations in $Ba_8Ga_xGe_ySi_{46-x-y}$ are more or less completely symmetric suggests that the key to understanding these variations, as should be expected based on the discussion in Sect. 2.2, is related to the tendency to avoid bonds between trivalent atoms. We have been able to demonstrate this behaviour by counting the number of nearest neighbours, which, as reported in Paper IV and Paper VIII, reveals that pair interactions between Al atoms are more unfavourable than those that involve at least one Ga atom. The fact that the Al-containing systems therefore have a stronger tendency to avoid bonds between trivalent atoms is, most probably, part of the reason why the transition temperatures for $Ba_8Ga_xGe_{46-x}$ and $Ba_8Ga_xSi_{46-x}$ are 300 K to 600 K lower than for $Ba_8Al_xGe_{46-x}$ and $Ba_8Al_xSi_{46-x}$.

A key issue associated with the calculations in Paper III and Paper VI is the under-

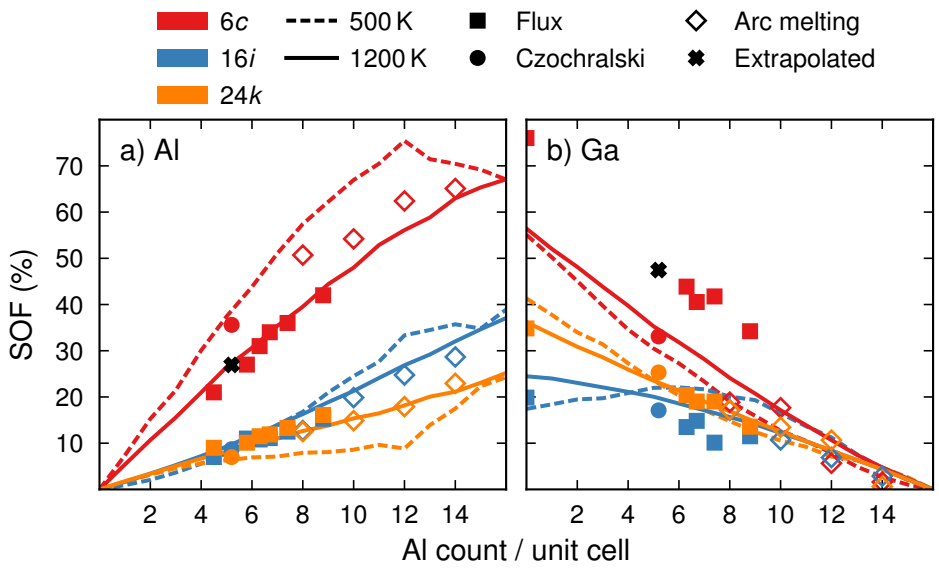

Figure 4.6: SOFs of the host elements (Al, Ga and Ge) at the 6*c* (red), 16*i* (blue), and 24*k* (orange) sites for Czochralski (filled circles), flux-grown (filled squares), and arc-melted [161] (open diamonds) samples together with results from MC simulations at 500 K (dashed lines) and 1200 K (solid lines). Black crosses indicate the predicted SOFs at $x = 5.2$ obtained via extrapolation of the data for the flux-grown samples.

estimation of the transition temperatures for both $Ba_8Ga_xGe_{46-x}$, $Ba_8Al_xGe_{46-x}$ and $Ba_8Al_xGa_yGe_{46-x-y}$. In spite of our extensive study of possible technical and physical origins for this discrepancy, we have, however, not yet found a satisfactory explanation. Still, it is important to note that a relatively good agreement is achieved for $Ba_8Al_xGe_{46-x}$ and $Ba_8Al_xSi_{46-x}$, which indicates that this problem is unique for the Ga-containing systems. For this reason, we find it reasonable to believe that this is, at least to some extent, related to the underlying DFT calculations, specifically the exchange-correlation functional and the treatment of the Ga 3*d*-states. One should also keep in mind that these are among the first studies that have explored order-disorder transitions in inorganic clathrates and therefore consider the results presented above in a broader context. The existing evidence strongly support the idea that it is neither unique for the specific systems that we have considered nor of purely academic interest. Rather, we suggest this transformation to be an inherent property of inorganic clathrates, which has a profound impact on a variety of physical properties. We therefore hope that our exploratory investigations can pave the way for future studies of these phenomena.

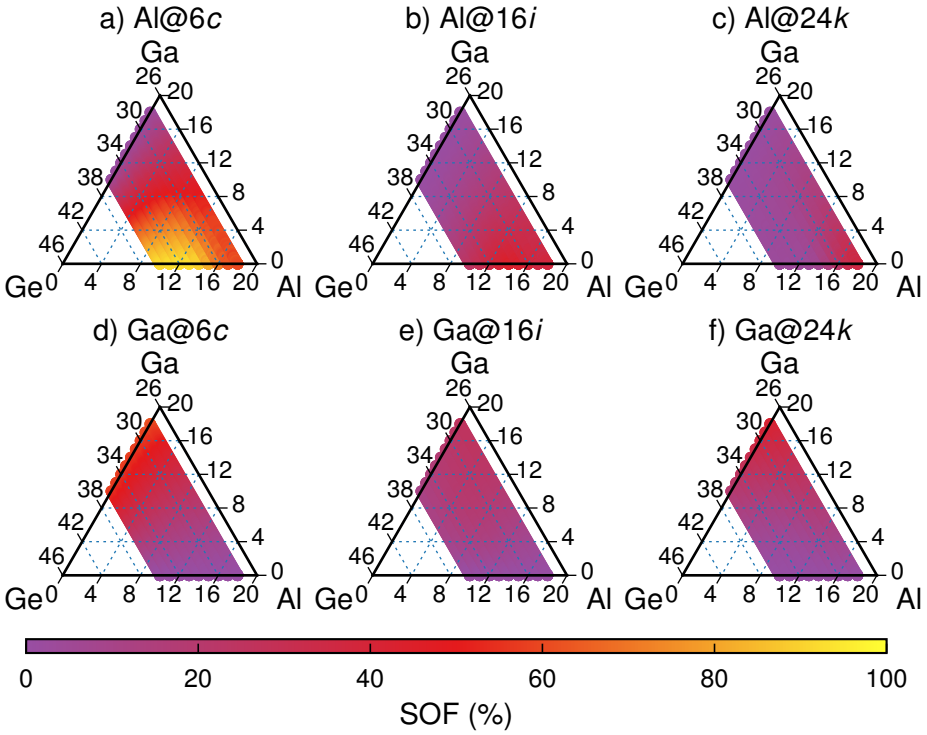

Figure 4.7: Maps with the Al (a-c) and Ga (d-f) SOFs at the 6*c* (a, d), 16*i* (b, e), and 24*k* (c, f) sites for $Ba_8Al_xGa_yGe_{46-x-y}$ based on MC simulations in hybrid canonical/VCSGC ensembles at 700 K.

4.3 Routes for optimising the electronic transport

Though there are several strategies for enhancing the thermoelectric performance, some of which were summarised in Sect. 1.4, only a handful have, as indicated in Sect. 2.3, been applied to inorganic clathrates. Given the intrinsically low lattice thermal conductivity for this group of materials we have decided to focus our attention on the electronic transport properties with the aim of finding ways to maximise the PF. It is interesting to note that our investigation of the lattice dynamics in $Ba_8Ga_{16}Ge_{30}$, presented in Paper I, essentially validates this choice. Specifically, this study revealed that the mean free paths of the propagating phonon modes decrease to about 1 nm already at 300 K, which means that even nanostructuring cannot be expected to have a significant influence on the thermal conductivity, especially not in the temperature range where inorganic clathrates are expected to be the most efficient with respect to thermoelectric energy conversion.

Since considerable effort has already been spent on trying to enhance the efficiency by optimising the carrier concentration in pseudo-binary systems, we decided to ex-

plore a pseudo-ternary system instead, specifically $Ba_8Al_xGa_yGe_{46-x-y}$. Through these efforts we found that $Ba_8Al_xGa_{16-x}Ge_{30}$ is in fact suitable for realising the modulation doping concept. As we show in Paper II, this is exactly what is achieved when pure $Ba_8Ga_{16}Ge_{30}$ and $Ba_8Al_{16}Ge_{30}$ powders are mixed and compacted into pellets via SPS. By studying the microstructure using scanning electron microscopy, we actually found that the material consisted of a $Ba_8Al_xGa_{16-x}Ge_{30}$ matrix together with micro- to nano-sized Al particles, which were both embedded in the clathrate phase and clustered on the grain boundaries. Remarkably, this leads to a significant increase in the weighted mobility (Sect. 3.3.4), which is even higher than that of a $Ba_8Al_5Ga_{11}Ge_{30}$ single crystal, and leading to a maximum zT of between 0.93 and 0.99 at 800 K. It is important to note that this approach is relatively fast, especially when compared to Czochralski-pulling, as well as scalable, meaning that it is potentially also interesting from a commercial perspective.

Another compelling reason for investigating pseudo-ternary clathrates is the greater tunability offered by the extra host species. In the case of $Ba_8Al_xGa_yGe_{46-x-y}$, for instance, it should as mentioned in Sect. 2.3 be possible to adjust the number of Al plus Ga atoms in order to optimise the carrier concentration while tuning the band structure via the Al/Ga ratio. Such possibilities have been explored in Paper VI where we calculated the power factor for a wide range of different $Ba_8Al_xGa_yGe_{46-x-y}$ and $Ba_8Ga_xGe_ySi_{46-x-y}$ compositions. By using a state-of-the-art $Ba_8Ga_{16}Ge_{30}$ sample as a reference, we could identify regions of interest that would be worthwhile to explore in more detail. Two key conclusions that can be drawn from this analysis is that the efficiency, as can be seen from Fig. 4.8, is generally enhanced if the number of trivalent elements is reduced, given that one somehow compensates for the resulting increase in the carrier concentration, for example, by extrinsic doping. In the case of $Ba_8Al_xGa_yGe_{46-x-y}$ it is moreover evident that a decent performance can only be expected for compositions with fewer than 9 Al atoms per unit cell. The situation for $Ba_8Ga_xGe_ySi_{46-x-y}$ meanwhile is quite different, since the calculations indicate that a performance similar to that of $Ba_8Ga_{16}Ge_{30}$ can be achieved even if the majority, or all, of the Ge atoms are replaced with Si. Since it is crucial to keep in mind that Al and Si are significantly cheaper as well as lighter than Ga and Ge, we repeated this analysis after weighting the PF by material cost and molar mass. As should be expected, the corresponding results further validate the above conclusions. The effect is, however, stronger for $Ba_8Ga_xGe_ySi_{46-x-y}$ compared to $Ba_8Al_xGa_yGe_{46-x-y}$, which is explained by the fact that that the difference in cost is more significant for Ge compared to Si and, additionally, because the total content of Al/Ga is lower than Si/Ge.

It is important to note that the study in Paper VI did not take into account the presence of the order-disorder transition. Elucidating the connection between this feature and the electronic transport parameters has instead been the primary focus of Paper III and, to some extent, Paper VII. Specifically, we find that accounting for this transformation is necessary in order to achieve good agreement with experiments, as

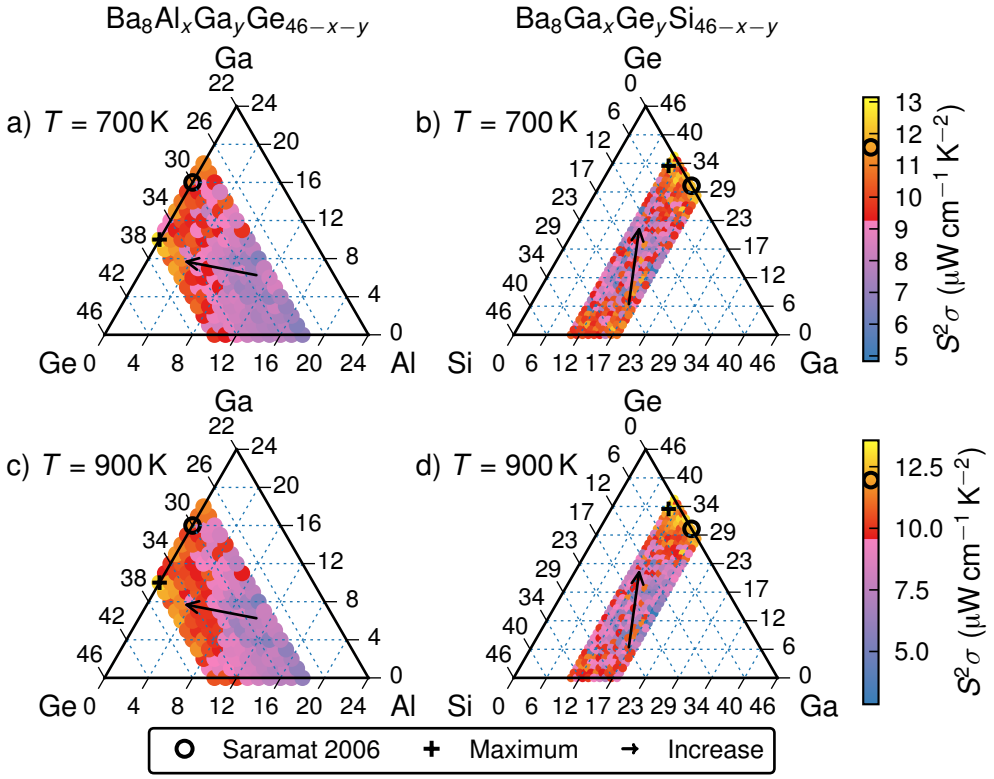

Figure 4.8: Mapping of the PF (σS^2) for $Ba_8Al_xGa_yGe_{46-x-y}$(a, c) and $Ba_8Ga_xGe_ySi_{46-x-y}$(b, d) at 700 K (a, b) and 900 K (c, d). The maximum value (plus) as well as the reference composition (circle), have also been indicated. Furthermore, the colour range, for each temperature, has been chosen so that the sharp shift (from pink to red) marks the 75 % limit, compared to value for the latter.

Fig. 4.9 clearly shows. One should especially note that by fitting the relaxation time, see Eq. (3.88), and doping level to the measured electrical conductivity and Seebeck coefficient using the calculations for the ground state below 650 K, we get a remarkably good match between the predicted and experimentally observed shifts in the same properties at the transition. It is worth noting that this is true not only for $Ba_8Al_5Ga_{11}Ge_{30}$ but also $Ba_8Ga_{16}Ge_{30}$ and $Ba_8Al_{16}Ge_{30}$. We moreover find that the transformation actually leads to an enhancement of the PF.

To further investigate the physical origin of the aforementioned observations, we have analysed and compared the band structure as well as the DOSs for the ordered and disordered states. As can be seen from Fig. 4.10, this leads to the conclusion that the transition leads to a significant increase in the regions of the DOSs that provide the largest contributions to the Seebeck coefficient while the effect is smaller in the energy range that is the most important for the electrical conductivity. This explains why the

shift at the transition temperature is more pronounced for the former property. In addition, it is clear that the transformation also leads to a much lower band gap, which is beneficial in this particular case. Interestingly, the situation is quite different for the compositions that we focus on in Paper VII, for which the reference data stems from measurements on flux-grown samples. For example, we find that the PF for the ground state is in several cases predicted to be higher than for the high temperature configuration and can moreover conclude that it is related to the relatively low carrier concentrations. The latter fact implies that the regions where the DOSs for the ground and high temperature states differ the most fall outside the windows that have the greatest effect on the electronic transport properties.

While the calculations presented in Paper III and Paper VI indicate that band structure engineering is feasible in $Ba_8Al_xGa_yGe_{46-x-y}$, our attempts to put this idea into practice, which is the main goal of Paper VII, revealed that tuning the Al/Ga ratio is not as simple as it may first appear. Specifically, we have found evidence that our flux-grown $Ba_8Al_xGa_{16-x}Ge_{30}$ samples with less than 5 Al atoms exhibit vacancies on the host sites, which leads to a lower thermoelectric performance. Interestingly, the features associated with presence of vacancies, which includes a previously reported but as of yet unexplained shift in the slope of the resistivity, disappear after annealing. As a result, the thermoelectric properties improve and become on par with those observed for the samples with higher Al content. Our detailed analysis of the weighted mobilities indicates, however, that tuning of the Al/Ga ratio does not yield any significant improvement. This conclusion is corroborated by the calculated electronic transport properties and band structures. In addition, the former reveal that the carrier concentrations is close to the optimum since any variations in the doping level lead to a lower PF. An unexpected result is that the sample with the highest Al content ($Ba_8Al_{8.8}Ga_{7.2}Ge_{30}$) displays a remarkably high mobility. The reason, as is revealed by a detailed analysis of the microstructure, is that it consists of a clathrate main phase together with Al nanoinclusions, similar to the samples that we investigated in Paper II. Hence, the flux-grown single crystals have, unintentionally, been transformed into a modulation-doped material via SPS.

Based on the results presented above it is evident that the order-disorder transition can have an impact on the thermoelectric performance of inorganic clathrates, especially in the temperature range that is of interest for practical applications. Yet the strength of the influence as well as the relative benefit depend on the doping level. In particular, the relative enhancement is larger for higher carrier concentrations. In our opinion, this phenomenon must consequently be taken into account when trying to optimise the electronic transport properties. We have also shown that simply varying the composition of phase pure $Ba_8Al_xGa_{16-x}Ge_{30}$ is not a very effective strategy for maximising the thermoelectric figure of merit, which in the case of polycrystalline samples should not be expected to reach much higher than 0.7. Significant improvements can, however, be achieved through microstructure engineering since our modulation

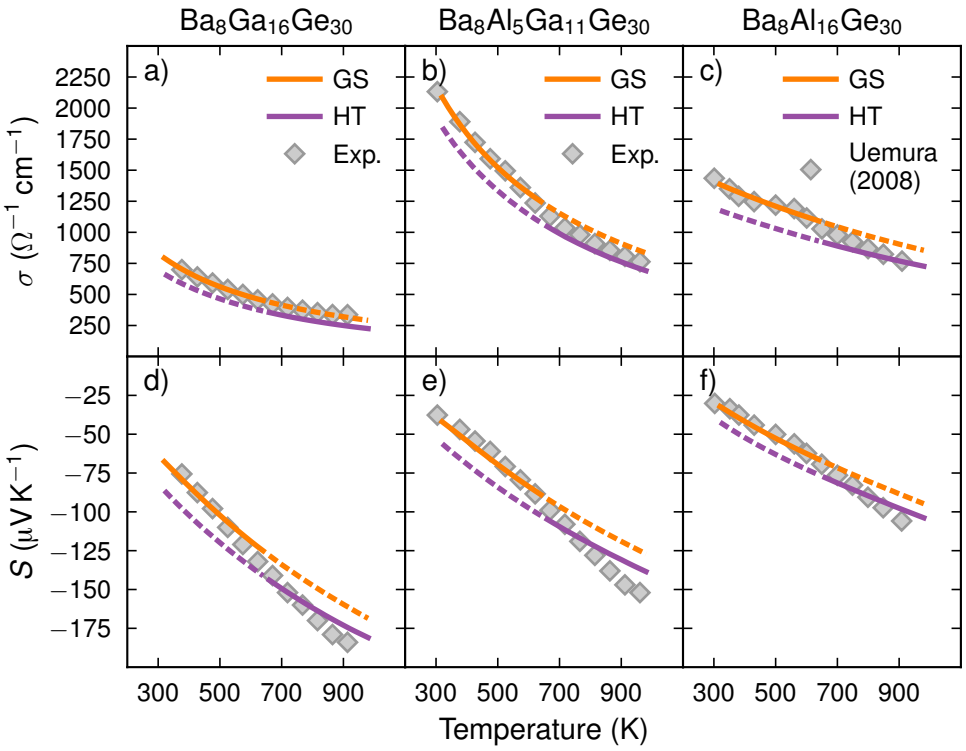

Figure 4.9: (a-c) Electrical conductivity and (d-f) Seebeck coefficient as a function of temperature. The calculated results for the ground state (GS) and high temperature (HT) structures have been plotted as orange and purple lines, respectively, while the grey diamonds represent data from experiments. The former curves correspond to the doping level that gave the best agreement between the measurements and calculated Seebeck coefficient, for the ground state, up to 650 K. In addition, the experimental electrical conductivity was used to fit the relaxation time, given by the expression $\tau_{\text{eff}} = \tau_{300\,\text{K}}(300\,\text{K}/T)^a$, in the same temperature interval. Note that the experimental measurements for $Ba_8Al_5Ga_{11}Ge_{30}$ have been performed on a single crystal, while the data for $Ba_8Ga_{16}Ge_{30}$ and $Ba_8Al_{16}Ge_{30}$ correspond to polycrystalline samples, of which the latter stems from a study by Uemura *et al.*[88]

doped samples display markedly higher mobilities and a 25 % better performance than a $Ba_8Al_xGa_{16-x}Ge_{30}$ single crystal. While band structure engineering has not proven to be very effective in the case of $Ba_8Al_xGa_{16-x}Ge_{30}$, the basic principles are equally applicable to other clathrate compounds, for which it might prove more useful. We therefore argue that pseudo-ternary inorganic type I clathrates, such as $Ba_8Al_xGa_ySi_{46-x-y}$, could, if suitably engineered, prove to be highly efficient and potentially even commercially viable candidates for thermoelectric applications. Hopefully, our efforts can serve as a guideline for future studies aimed at realising their full potential.

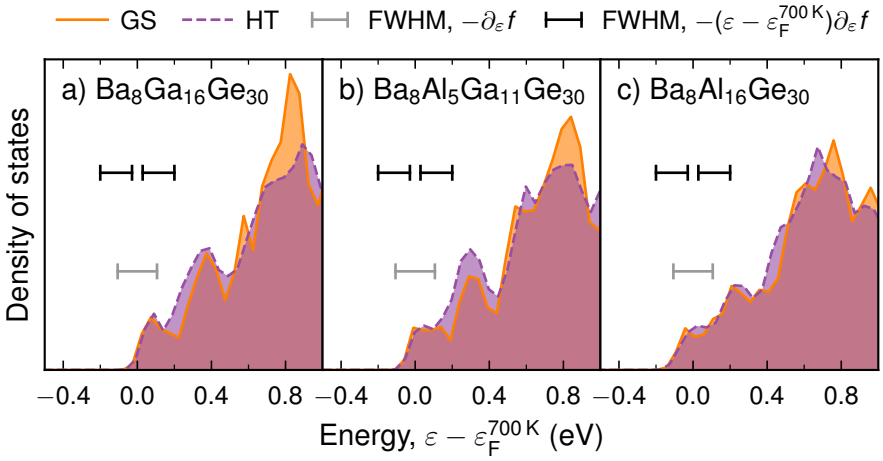

Figure 4.10: Electronic DOSs for (a) $Ba_8Ga_{16}Ge_{30}$, (b) $Ba_8Al_5Ga_{11}Ge_{30}$, and (c) $Ba_8Al_{16}Ge_{30}$, where the ground state (GS) and high temperature (HT) structures are represented by purple dotted and orange solid curves, respectively. Moreover, the full width at half maximum (FWHM) for both the derivative of the Fermi distribution function, $-\partial_\varepsilon f$, (grey horizontal bar) and the two peaks featured by the product $-(\varepsilon - \varepsilon_F^{700\,K})^\alpha \partial_\varepsilon f$ (black horizontal bars) have been indicated. Here, $\varepsilon_F^{700\,K}$ is the doping level that provides the best agreement between the calculated and experimental Seebeck coefficients at 700 K. For each composition, the energy scales have been aligned using the Ba-1s states, with the ground state valance band (VB) maximum set to zero [162].

Acknowledgments

This project has, in many respects, been a collaborative effort that his involved almost too many people to count. Though I value the efforts of each and every one of you, there are a few persons that deserve a special mention.

First and foremost I would like to extend my heartfelt gratitude to my supervisors Anders Palmqvist and Paul Erhart, without whose unwavering support and understanding I would never have reached this far. I thank you for guiding me on this seven year long journey.

In addition, would like to express my deep appreciation for the hard work and dedication, as well as good spirits and enthusiasm, of my dear collegue Yifei Zhang. I am so glad that we have shared this journey together and is looking forward to the day, which is not so far away, when you receive your well deserved PhD degree.

Though it is not until recently that we have interacted to a greater extent, I would also like to thank my examiner Hanna Härelind and the current vice head of the department of Chemistry and Chemical Engineering, Nina Kann, for helping with all the bureaucracy related to this last stretch of my PhD.

I moroever wish to acknowledge a few current and previous members of the computational materials group, namely Mattias Ångqvist, Erik Fransson, Magnus Rahm, Fredrik Eriksson, Joakim Löfgren and Daniel Lindroth whose assistance and expertise has been invaluable to me when I tried to grasp the various computational methods that I have employed in this project.

For the same reason, I would like to give thanks to Zheyong Fan and Jesús Carrete Montaña for not only helping me to familiarise myself with the GPUMD and BoltzTraP2 codes, respectively, but also their willingness to implement new functionalities to serve my needs.

While I am very grateful to my other coauthors I would like to thank Arsalan Hashemi, in particular, for his trust and good nature.

Though several years may have passed I have not forgotten all the help that I have received from Richard Heijl, Samrand Shafeie, Andrey Sizov, Hazel Reardon and David Kiefer as I began to get acquainted with the various experimental tools, techniques and instruments that have been employed in this project.

I am also thankful to Giulio Calcagno, Walter Rosas Arbelaez, Samuel Fretz, Milene

Zezzi do Valle Gomes, Gunnar Símonarson and Caroline Janson as well as all the other members of Anders' research group not only for their advice and practical assistance in various context but also their kindness and for being a source of energy and inspiration.

In the same spirit, I feel the need to mention the rest of my colleagues at the Applied Chemistry division for their role in creating a truly warm and inspiring environment, which makes it a delight to enter into the premises and especially the fika room, which is more often than not teeming with people willing to engage in quick chat and thereby forget one's burdens, if only for a moment.

At this point, I also want to acknowledge the Center for Thermoelectric Energy Conversion (CTEC), and by extent the Danish Research Council, for both their financial support and continued trust that I will see this project through. In this context, I would also like to mention Bo Iversen as well as all the other participants of the CTEC meetings, which I found truly enjoyable, for their friendly and valuable advice.

Last but by no means least I must say that I am in awe of my family for weathering with me during these turbulent years. Even though, there have been many ups and downs you have always been by my side and for carrying me through the rougher periods and, when required, either lifting me up or calming me down. I could never have made it without you.

Bibliography

[1] R. K. Pachauri, M. R. Allen, V. R. Barros, J. Broome, W. Cramer, R. Christ, J. A. Church, L. Clarke, Q. Dahe, P. Dasgupta, N. K. Dubash, O. Edenhofer, I. Elgizouli, C. B. Field, P. Forster, P. Friedlingstein, J. Fuglestvedt, L. Gomez-Echeverri, S. Hallegatte, G. Hegerl, M. Howden, K. Jiang, B. J. Cisneroz, V. Kattsov, H. Lee, K. J. Mach, J. Marotzke, M. D. Mastrandrea, L. Meyer, J. Minx, Y. Mulugetta, K. O'Brien, M. Oppenheimer, J. J. Pereira, R. Pichs-Madruga, G.-K. Plattner, H.-O. Pörtner, S. B. Power, B. Preston, N. H. Ravindranath, A. Reisinger, K. Riahi, M. Rusticucci, R. Scholes, K. Seyboth, Y. Sokona, R. Stavins, T. F. Stocker, P. Tschakert, D. van Vuuren, and J.-P. van Ypserle, in *Climate Change 2014: Synthesis Report. Contribution of Working Groups I, II and III to the Fifth Assessment Report of the Intergovernmental Panel on Climate Change*, edited by R. Pachauri and L. Meyer (IPCC, Geneva, Switzerland, 2014), p. 151.

[2] International Energy Agency, *World Energy Balances 2018* (OECD Publishing, Paris, France, 2018), p. 762.

[3] American Physical Society, *Energy Units*, 2018.

[4] Lawrence Livermore National Laboratory, *Energy Flow Charts: Charting the Complex Relationships among Energy, Water, and Carbon*, 2020.

[5] D. M. Rowe, in *Thermoelectrics Handbook: Macro to Nano*, edited by D. M. Rowe (CRC Press, Boca Raton, USA, 2005), Chap. 1, p. 1.

[6] C. B. Vining, *An inconvenient truth about thermoelectrics*, Nature Materials **8**, 83 (2009).

[7] G. Tan, L.-D. Zhao, and M. G. Kanatzidis, *Rationally Designing High-Performance Bulk Thermoelectric Materials*, Chemical Reviews **116**, 12123 (2016).

[8] L. Yang, Z.-G. Chen, M. S. Dargusch, and J. Zou, *High Performance Thermoelectric Materials: Progress and Their Applications*, Advanced Energy Materials **8**, 1701797 (2018).

[9] H.-S. Kim, Z. M. Gibbs, Y. Tang, H. Wang, and G. J. Snyder, *Characterization of Lorenz number with Seebeck coefficient measurement*, APL Materials **3**, 041506 (2015).

[10] G. K. Madsen, J. Carrete, and M. J. Verstraete, *BoltzTraP2, a program for interpolating band structures and calculating semi-classical transport coefficients*, Computer Physics Communications **231**, 140 (2018).

[11] M. Ångqvist, D. O. Lindroth, and P. Erhart, *Optimization of the Thermoelectric Power Factor: Coupling between Chemical Order and Transport Properties*, Chemistry of Materials **28**, 6877 (2016).

[12] J. R. Sootsman, D. Y. Chung, and M. G. Kanatzidis, *New and Old Concepts in Thermoelectric Materials*, Angewandte Chemie International Edition **48**, 8616 (2009).

[13] D. M. Rowe, in *CRC Handbook of Thermoelectrics*, edited by D. M. Rowe (CRC Press, Boca Raton, USA, 1995), Chap. 1, pp. 1–5.

[14] G. A. Slack, in *CRC Handbook of Thermoelectrics*, edited by D. M. Rowe (CRC Press, Boca Raton, USA, 1995), Chap. 34, pp. 407–440.

[15] M. S. Dresselhaus, G. Chen, M. Y. Tang, R. G. Yang, H. Lee, D. Z. Wang, Z. F. Ren, J.-P. Fleurial, and P. Gogna, *New Directions for Low-Dimensional Thermoelectric Materials*, Advanced Materials **19**, 1043 (2007).

[16] L. D. Hicks and M. S. Dresselhaus, *Effect of quantum-well structures on the thermoelectric figure of merit*, Physical Review B **47**, 12727 (1993).

[17] L. D. Hicks and M. S. Dresselhaus, *Thermoelectric figure of merit of a one-dimensional conductor*, Physical Review B **47**, 16631 (1993).

[18] C. Han, Z. Li, and S. Dou, *Recent progress in thermoelectric materials*, Chinese Science Bulletin **59**, 2073 (2014).

[19] G. D. Mahan and J. O. Sofo, *The best thermoelectric*, Proceedings of the National Academy of Sciences **93**, 7436 (1996).

[20] G. J. Snyder and E. S. Toberer, *Complex thermoelectric materials*, Nature Materials **7**, 105 (2008).

[21] M. Zebarjadi, K. Esfarjani, M. S. Dresselhaus, Z. F. Ren, and G. Chen, *Perspectives on thermoelectrics: from fundamentals to device applications*, Energy & Environmental Science **5**, 5147 (2012).

[22] L.-D. Zhao, V. P. Dravid, and M. G. Kanatzidis, *The panoscopic approach to high performance thermoelectrics*, Energy & Environmental Science **7**, 251 (2014).

[23] C. Gayner and K. K. Kar, *Recent advances in thermoelectric materials*, Progress in Materials Science **83**, 330 (2016).

[24] T. Zhu, Y. Liu, C. Fu, J. P. Heremans, J. G. Snyder, and X. Zhao, *Compromise and Synergy in High-Efficiency Thermoelectric Materials*, Advanced Materials **29**, 1605884 (2017).

[25] A. F. May, E. S. Toberer, A. Saramat, and G. J. Snyder, *Characterization and analysis of thermoelectric transport in n-type* $Ba_8Ga_{16-x}Ge_{30+x}$, Physical Review B **80**, 125205 (2009).

[26] Y. Pei, A. F. May, and G. J. Snyder, *Self-Tuning the Carrier Concentration of PbTe/*Ag_2Te *Composites with Excess Ag for High Thermoelectric Performance*, Advanced Energy Materials **1**, 291 (2011).

[27] K. Biswas, J. He, Q. Zhang, G. Wang, C. Uher, V. P. Dravid, and M. G. Kanatzidis, *Strained endotaxial nanostructures with high thermoelectric figure of merit*, Nature Chemistry **3**, 160 (2011).

[28] K. Biswas, J. He, I. D. Blum, C.-I. Wu, T. P. Hogan, D. N. Seidman, V. P. Dravid, and M. G. Kanatzidis, *High-performance bulk thermoelectrics with all-scale hierarchical architectures*, Nature **489**, 414 (2012).

[29] J. He, M. G. Kanatzidis, and V. P. Dravid, *High performance bulk thermoelectrics via a panoscopic approach*, Materials Today **16**, 166 (2013).

[30] T. Liang, X. Su, Y. Yan, G. Zheng, X. She, Y. You, C. Uher, M. G. Kanatzidis, and X. Tang, *Panoscopic approach for high-performance Te-doped skutterudite*, NPG Asia Materials **9**, e352 (2017).

[31] F. Pulizzi, *The panoscopic approach*, Nature Nanotechnology **7**, 622 (2012).

[32] M. Zebarjadi, G. Joshi, G. Zhu, B. Yu, A. Minnich, Y. Lan, X. Wang, M. Dresselhaus, Z. Ren, and G. Chen, *Power Factor Enhancement by Modulation Doping in Bulk Nanocomposites*, Nano Letters **11**, 2225 (2011).

[33] J. S. Kasper, P. Hagenmuller, M. Pouchard, and C. Cros, *Clathrate Structure of Silicon* Na_8Si_{46} *and* Na_xSi_{136} *(*$x < 11$*)*, Science **150**, 1713 (1965).

[34] C. Cros, in *The Physics and Chemistry of Inorganic Clathrates*, Vol. 199 of *Springer Series in Materials Science*, edited by G. S. Nolas (Springer, Dordrecht, Netherlands, 2014), pp. v–vii.

[35] T. Takabatake, K. Suekuni, T. Nakayama, and E. Kaneshita, *Phonon-glass electron-crystal thermoelectric clathrates: Experiments and theory*, Reviews of Modern Physics **86**, 669 (2014).

[36] J.-A. Dolyniuk, B. Owens-Baird, J. Wang, J. V. Zaikina, and K. Kovnir, *Clathrate thermoelectrics*, Materials Science and Engineering: R: Reports **108**, 1 (2016).

[37] A. V. Shevelkov, K. A. Kovnir, and J. V. Zaikina, *The Physics and Chemistry of Inorganic Clathrates*, *Springer Series in Materials Science* (Springer, Dordrecht, Netherlands, 2014), pp. 125–167.

[38] A. Bentien, A. E. C. Palmqvist, J. D. Bryan, S. Latturner, G. D. Stucky, L. Furenlid, and B. B. Iversen, *Experimental Charge Densities of Semiconducting Cage Structures Containing Alkaline Earth Guest Atoms*, Angewandte Chemie International Edition **39**, 3613 (2000).

[39] B. Chakoumakos, B. Sales, D. Mandrus, and G. Nolas, *Structural disorder and thermal conductivity of the semiconducting clathrate* $Sr_8Ga_{16}Ge_{30}$, Journal of Alloys and Compounds **296**, 80 (2000).

[40] B. C. Sales, B. C. Chakoumakos, R. Jin, J. R. Thompson, and D. Mandrus, *Structural, magnetic, thermal, and transport properties of* $X_8Ga_{16}Ge_{30}$ (X = Eu, Sr, Ba) *single crystals*, Physical Review B **63**, 245113 (2001).

[41] B. Chakoumakos, B. Sales, and D. Mandrus, *Structural disorder and magnetism of the semiconducting clathrate* $Eu_8Ga_{16}Ge_{30}$, Journal of Alloys and Compounds **322**, 127 (2001).

[42] N. P. Blake, D. Bryan, S. Latturner, L. Møllnitz, G. D. Stucky, and H. Metiu, *Structure and stability of the clathrates* $Ba_8Ga_{16}Ge_{30}$, *Sr8Ga16Ge30, Ba8Ga16Si30, and Ba8In16Sn30*, The Journal of Chemical Physics **114**, 10063 (2001).

[43] A. Bentien, B. Iversen, J. Bryan, G. Stucky, A. Palmqvist, A. Schultz, and R. Henning, *Maximum entropy method analysis of thermal motion and disorder in thermoelectric clathrate* $Ba_8Ga_{16}Si_{30}$, Journal of Applied Physics **91**, 5694 (2002).

[44] A. Bentien, M. Christensen, J. D. Bryan, A. Sanchez, S. Paschen, F. Steglich, G. D. Stucky, and B. B. Iversen, *Thermal conductivity of thermoelectric clathrates*, Physical Review B **69**, 045107 (2004).

[45] A. Bentien, E. Nishibori, S. Paschen, and B. B. Iversen, *Crystal structures, atomic vibration, and disorder of the type-I thermoelectric clathrates* $Ba_8Ga_{16}Si_{30}$, $Ba_8Ga_{16}Ge_{30}$, $Ba_8In_{16}Ge_{30}$, *and* $Sr_8Ga_{16}Ge_{30}$, Physical Review B **71**, 1 (2005).

[46] M. Christensen, N. Lock, J. Overgaardk, and B. B. Iversen, *Crystal Structures of Thermoelectric n- and p-type* $Ba_8Ga_{16}Ge_{30}$ *Studied by Single Crystal, Multitemperature, Neutron Diffraction, Conventional X-ray Diffraction and Resonant Synchrotron X-ray Diffraction*, Journal of the American Chemical Society **128**, 15657 (2006).

[47] M. A. Avila, K. Suekuni, K. Umeo, H. Fukuoka, S. Yamanaka, and T. Takabatake, *Glasslike versus crystalline thermal conductivity in carrier-tuned $Ba_8Ga_{16}X_{30}$ clathrates (X=Ge,Sn)*, Physical Review B **74**, 125109 (2006).

[48] M. Christensen and B. B. Iversen, *Host Structure Engineering in Thermoelectric Clathrates*, Chemistry of Materials **19**, 4896 (2007).

[49] K. Suekuni, M. Avila, K. b. Umeo, and T. c. Takabatake, *Cage-size control of guest vibration and thermal conductivity in $Sr_8Ga_{16}Si_{30-x}Ge_x$*, Physical Review B **75**, 195210 (2007).

[50] Y. Takasu, T. Hasegawa, N. Ogita, M. Udagawa, M. A. Avila, K. Suekuni, and T. Takabatake, *Off-Center Rattling and Anisotropic Expansion of Type-I Clathrates Studied by Raman Scattering*, Physical Review Letters **100**, 1 (2008).

[51] T. Mori, S. Goshima, K. Iwamoto, S. Kushibiki, H. Matsumoto, N. Toyota, K. Suekuni, M. A. Avila, T. Takabatake, T. Hasegawa, N. Ogita, and M. Udagawa, *Optical conductivity of rattling phonons in type-I clathrate $Ba_8Ga_{16}Ge_{30}$*, Physical Review B **79**, 212301 (2009).

[52] K. Suekuni, Y. Takasu, T. Hasegawa, N. Ogita, M. Udagawa, M. A. Avila, and T. Takabatake, *Off-center rattling modes and glasslike thermal conductivity in the type-I clathrate $Ba_8Ga_{16}Sn_{30}$*, Physical Review B **81**, 205207 (2010).

[53] Y. Takasu, T. Hasegawa, N. Ogita, M. Udagawa, M. A. Avila, K. Suekuni, and T. Takabatake, *Off-center rattling and cage vibration of the carrier-tuned type-I clathrate $Ba_8Ga_{16}Ge_{30}$ studied by Raman scattering*, Physical Review B **82**, 134302 (2010).

[54] K. Iwamoto, T. Mori, S. Kushibiki, H. Honda, H. Matsumoto, K. Suekuni, M. Avila, T. Takabatake, and N. Toyota, in *Materials Integration*, Vol. 508 of *Key Engineering Materials* (Trans Tech Publications, Baech, Switzerland, 2012), pp. 341–346.

[55] K. Iwamoto, S. Kushibiki, H. Honda, S. Kajitani, T. Mori, H. Matsumoto, N. Toyota, K. Suekuni, M. A. Avila, and T. Takabatake, *Anomalous Infrared Spectra of Hybridized Phonons in Type-I Clathrate $Ba_8Ga_{16}Ge_{30}$*, Journal of the Physical Society of Japan **82**, 024601 (2013).

[56] S. Christensen, M. S. Schmøkel, K. A. Borup, G. K. H. Madsen, G. J. McIntyre, S. C. Capelli, M. Christensen, and B. B. Iversen, *"Glass-like" thermal conductivity gradually induced in thermoelectric $Sr_8Ga_{16}Ge_{30}$ clathrate by off-centered guest atoms*, Journal of Applied Physics **119**, 185102 (2016).

[57] W. R. Puspita, H. Takeya, T. Mochiku, Y. Ishikawa, S. Lee, S. Torii, M. Yonemura, and T. Kamiyama, *Temperature dependence of structural disorder in thermoelectric clathrate $Ba_8Al_{16}Ge_{30}$*, Physica B **551**, 41 (2018).

[58] N. P. Blake, L. Møllnitz, G. Kresse, and H. Metiu, *Why clathrates are good thermoelectrics: A theoretical study of $Sr_8Ga_{16}Ge_{30}$*, The Journal of Chemical Physics **111**, 3133 (1999).

[59] G. K. H. Madsen and G. Santi, *Anharmonic lattice dynamics in type-I clathrates from first-principles calculations*, Physical Review B **72**, 220301 (2005).

[60] M. Ångqvist and P. Erhart, *Understanding Chemical Ordering in Intermetallic Clathrates from Atomic Scale Simulations*, Chemistry of Materials **29**, 7554 (2017).

[61] M. A. Avila, K. Suekuni, K. Umeo, H. Fukuoka, S. Yamanaka, and T. Takabatake, *$Ba_8Ga_{16}Sn_{30}$ with type-I clathrate structure: Drastic suppression of heat conduction*, Applied Physics Letters **92**, 041901 (2008).

[62] G. S. Nolas, J. L. Cohn, G. A. Slack, and S. B. Schujman, *Semiconducting Ge clathrates: Promising candidates for thermoelectric applications*, Applied Physics Letters **73**, 178 (1998).

[63] J. L. Cohn, G. S. Nolas, V. Fessatidis, T. H. Metcalf, and G. A. Slack, *Glasslike Heat Conduction in High-Mobility Crystalline Semiconductors*, Physical Review Letters **82**, 779 (1999).

[64] V. Keppens, B. Sales, D. Mandrus, B. Chakoumakos, and C. Laermans, *When does a crystal conduct heat like a glass?*, Philosophical Magazine Letters **80**, 807 (2000).

[65] P.-F. Lory, S. Pailhès, V. M. Giordano, H. Euchner, H. D. Nguyen, R. Ramlau, H. Borrmann, M. Schmidt, M. Baitinger, M. Ikeda, P. Tomeš, M. Mihalkovič, C. Allio, M. R. Johnson, H. Schober, Y. Sidis, F. Bourdarot, L. P. Regnault, J. Ollivier, S. Paschen, Y. Grin, and M. de Boissieu, *Direct measurement of individual phonon lifetimes in the clathrate compound $Ba_{7.81}Ge_{40.67}Au_{5.33}$*, Nature Communications **8**, 491 (2017).

[66] Y. Liu, Q. Xi, J. Zhou, T. Nakayama, and B. Li, *Phonon-glass dynamics in thermoelectric clathrates*, Physical Review B **93**, 214305 (2016).

[67] C. Chen, Z. Zhang, and J. Chen, *Revisit to the Impacts of Rattlers on Thermal Conductivity of Clathrates*, Frontiers in Energy Research **6**, 34 (2018).

[68] T. Tadano and S. Tsuneyuki, *Quartic Anharmonicity of Rattlers and Its Effect on Lattice Thermal Conductivity of Clathrates from First Principles*, Physical Review Letters **120**, 105901 (2018).

[69] T. Tadano, Y. Gohda, and S. Tsuneyuki, *Impact of Rattlers on Thermal Conductivity of a Thermoelectric Clathrate: A First-Principles Study*, Physical Review Letters **114**, 095501 (2015).

[70] M. S. Ikeda, H. Euchner, X. Yan, P. Tomeš, A. Prokofiev, L. Prochaska, G. Lientschnig, R. Svagera, S. Hartmann, E. Gati, M. Lang, and S. Paschen, *Kondo-like phonon scattering in thermoelectric clathrates*, Nature Communications **10**, 887 (2019).

[71] D. G. Cahill, S. K. Watson, and R. O. Pohl, *Lower limit to the thermal conductivity of disordered crystals*, Phys. Rev. B **46**, 6131 (1992).

[72] M. Christensen, A. B. Abrahamsen, N. B. Christensen, F. Juranyi, N. H. Andersen, K. Lefmann, J. Andreasson, C. R. H. Bahl, and B. B. Iversen, *Avoided crossing of rattler modes in thermoelectric materials*, Nature Materials **7**, 811 (2008).

[73] Q. Xi, Z. Zhang, T. Nakayama, J. Chen, J. Zhou, and B. Li, *Off-center rattling triggers high-temperature thermal transport in thermoelectric clathrates: Nonperturbative approach*, Physical Review B **97**, 224308 (2018).

[74] M. Christensen, S. Johnsen, and B. B. Iversen, *Thermoelectric clathrates of type I*, Dalton Transactions **39**, 978 (2010).

[75] M. Troppenz, S. Rigamonti, and C. Draxl, *Predicting Ground-State Configurations and Electronic Properties of the Thermoelectric Clathrates $Ba_8Al_xSi_{46-x}$ and $Sr_8Al_xSi_{46-x}$*, Chemistry of Materials **29**, 2414 (2017).

[76] N. L. Okamoto, K. Kishida, K. Tanaka, and H. Inui, *Crystal structure and thermoelectric properties of type-I clathrate compounds in the Ba–Ga–Ge system*, Journal of Applied Physics **100**, 073504 (2006).

[77] H. Anno, H. Yamada, T. Nakabayashi, M. Hokazono, and R. Shirataki, *Gallium composition dependence of crystallographic and thermoelectric properties in polycrystalline type-I $Ba_8Ga_xSi_{46-x}$ (nominal $x = 14 - 18$) clathrates prepared by combining arc melting and spark plasma sintering methods*, Journal of Solid State Chemistry **193**, 94 (2012).

[78] S. Y. Rodriguez, L. Saribaev, and J. H. Ross, *Zintl behavior and vacancy formation in type-I Ba-Al-Ge clathrates*, Physical Review B **82**, 064111 (2010).

[79] H. Anno, M. Hokazono, R. Shirataki, and Y. Nagami, *Crystallographic, Thermoelectric, and Mechanical Properties of Polycrystalline $Ba_8Al_xSi_{46-x}$ Clathrates*, Journal of Electronic Materials **42**, 2326 (2013).

[80] N. Tsujii, J. H. Roudebush, A. Zevalkink, C. A. Cox-Uvarov, G. J. Snyder, and S. M. Kauzlarich, *Phase stability and chemical composition dependence of the thermoelectric properties of the type-I clathrate* $Ba_8Al_xSi_{46-x}$, ($8 \leq x \leq 15$), Journal of Solid State Chemistry **184**, 1293 (2011).

[81] Y. Nagatomo, N. Mugita, Y. Nakakohara, M. Saisho, M. Tajiri, R. Teranishi, and S. Munetoh, *Thermoelectric properties of single crystalline* $Ba_8Al_xSi_{46-x}$ *clathrate by using flux Czochralski method*, Journal of Physics: Conference Series **379**, 012008 (2012).

[82] H. Anno, M. Hokazono, R. Shirataki, and Y. Nagami, *Crystallographic, thermoelectric, and mechanical properties of polycrystalline type-I* $Ba_8Al_{16}Si_{30}$*-based clathrates*, Journal of Materials Science **48**, 2846 (2013).

[83] S. M. Kauzlarich, A. Zevalkink, E. Toberer, and G. J. Snyder, *Thermoelectric Materials and Devices* (The Royal Society of Chemistry, Cambridge, UK, 2017), pp. 1–26.

[84] S. Stefanoski, M. Beekman, and G. S. Nolas, in *The Physics and Chemistry of Inorganic Clathrates*, Vol. 199 of *Springer Series in Materials Science*, edited by G. S. Nolas (Springer, Dordrecht, Netherlands, 2014), Chap. 6, pp. 169–191.

[85] H. Anno, M. Hokazono, M. Kawamura, J. Nagao, and K. Matsubara, in *Proceedings ICT '02. Twenty-First International Conference on Thermoelectrics, 2002.* (IEEE, New York, USA, 2002), pp. 77–80.

[86] J. D. Bryan, N. P. Blake, H. Metiu, G. D. Stucky, B. B. Iversen, R. D. Poulsen, and A. Bentien, *Nonstoichiometry and chemical purity effects in thermoelectric* $Ba_8Ga_{16}Ge_{30}$ *clathrate*, Journal of Applied Physics **92**, 7281 (2002).

[87] M. Avila, K. Suekuni, K. Umeo, and T. Takabatake, *Carrier-tuning of single-crystalline* $Ba_8Ga_{16}Ge_{30}$, Physica B **383**, 124 (2006).

[88] T. Uemura, K. Akai, K. Koga, T. Tanaka, H. Kurisu, S. Yamamoto, K. Kishimoto, T. Koyanagi, and M. Matsuura, *Electronic structure and thermoelectric properties of clathrate compounds* $Ba_8Al_xGe_{46-x}$, Journal of Applied Physics **104**, 013702 (2008).

[89] J. Martin, H. Wang, and G. S. Nolas, *Optimization of the thermoelectric properties of* $Ba_8Ga_{16}Ge_{30}$, Applied Physics Letters **92**, 222110 (2008).

[90] S.-K. Deng, X.-F. Tang, and R.-S. Tang, *Synthesis and high temperature thermoelectric transport properties of Si-based type-I clathrates*, Chinese Physics B **18**, 3084 (2009).

[91] J. Leszczynski, A. Kolezynski, and K. Wojciechowski, *Electronic and transport properties of polycrystalline $Ba_8Ga_{15}Ge_{31}$ type I clathrate prepared by SPS method*, Journal of Solid State Chemistry **193**, 114 (2012).

[92] L.-H. Wang and L.-S. Chang, *Thermoelectric properties of p-type $Ba_8Ga_{16}Ge_{30}$ type-I clathrate compounds prepared by the vertical Bridgman method*, Journal of Alloys and Compounds **722**, 644 (2017).

[93] J.-W. Yeh, S.-K. Chen, S.-J. Lin, J.-Y. Gan, T.-S. Chin, T.-T. Shun, C.-H. Tsau, and S.-Y. Chang, *Nanostructured High-Entropy Alloys with Multiple Principal Elements: Novel Alloy Design Concepts and Outcomes*, Advanced Engineering Materials **6**, 299 (2004).

[94] S. Shafeie, S. Guo, Q. Hu, H. Fahlquist, P. Erhart, and A. Palmqvist, *High-entropy alloys as high-temperature thermoelectric materials*, Journal of Applied Physics **118**, 184905 (2015).

[95] S. Shafeie, S. Guo, P. Erhart, Q. Hu, and A. Palmqvist, *Balancing Scattering Channels: A Panoscopic Approach toward Zero Temperature Coefficient of Resistance Using High-Entropy Alloys*, Advanced Materials **31**, 1805392 (2019).

[96] M. Beekman and G. S. Nolas, in *The Physics and Chemistry of Inorganic Clathrates*, Vol. 199 of *Springer Series in Materials Science*, edited by G. S. Nolas (Springer, Dordrecht, Netherlands, 2014), Chap. 8, pp. 227–258.

[97] E. George, D. Raabe, and R. Ritchie, *High-entropy alloys*, Nature Reviews Materials **4**, 515 (2019).

[98] K. Kishimoto, N. Ikeda, K. Akai, and T. Koyanagi, *Synthesis and Thermoelectric Properties of Silicon Clathrates $Sr_8Al_xGa_{16-x}Si_{30}$ with the Type-I and Type-VIII Structures*, Applied Physics Express **1**, 1 (2008).

[99] H. Shimizu, Y. Takeuchi, T. Kume, S. Sasaki, K. Kishimoto, N. Ikeda, and T. Koyanagi, *Raman spectroscopy of type-I and type-VIII silicon clathrate alloys $Sr_8Al_xGa_{16-x}Si_{30}$*, Journal of Alloys and Compounds **487**, 47 (2009).

[100] M. Imai, K. Nishida, T. Kimura, and K. Yamada, *Synthesis of a Si-clathrate compound, $Sr_8Ga_xSi_{46-x}$, and its electrical resistivity measurements*, Journal of Alloys and Compounds **335**, 270 (2002).

[101] J. H. Roudebush, N. Tsujii, A. Hurtando, H. Hope, Y. Grin, and S. M. Kauzlarich, *Phase Range of the Type-I Clathrate $Sr_8Al_xSi_{46-x}$ and Crystal Structure of $Sr_8Al_{10}Si_{36}$*, Inorganic Chemistry **51**, 4161 (2012).

[102] D. Kikuchi, J. Tadokoro, and T. Eguchi, *The High-Temperature Thermoelectric Properties of Polycrystalline $Ba_8Ga_xAl_ySi_{46-x-y}$ Type-I Clathrates*, Journal of Electronic Materials **43**, 2141 (2014).

[103] S. Witanachchi, R. Hyde, H. Nagaraja, M. Beekman, G. Nolas, and P. Mukherjee, *Growth and characterization of Germanium-based type I clathrate thin films deposited by pulsed laser ablation*, Materials Research Society Symposium Proceedings **886**, 401 (2006).

[104] L. Miao, S. Tanemura, T. Watanabe, M. Tanemura, S. Toh, K. Kaneko, Y. Sugahara, and T. Hirayama, *Epitaxial growth of $Ba_8Ga_{16}Ge_{30}$ clathrate film on Si substrate by RF helicon magnetron sputtering with evaluation on thermoelectric properties*, Applied Surface Science **254**, 167 (2007).

[105] R. Shirataki, M. Hokazono, T. Nakabayashi, and H. Anno, *Preparation and characterization of planetary ball milled Si-based clathrates and their spark plasma sintered materials*, IOP Conference Series: Materials Science and Engineering **18**, 142012 (2011).

[106] R. Christian, M. Ikeda, G. Lientschnig, L. Prochaska, A. Prokofiev, P. Tomeš, X. Yan, A. Zolriasatein, J. Bernardi, T. Schachinger, S. Schwarz, A. Steiger-Thirsfeld, P. Rogl, S. Populoh, A. Weidenkaff, and S. Paschen, *Nanostructured clathrates and clathrate-based nanocomposites*, physica status solidi (a) **213**, 784 (2016).

[107] V. Pacheco, H. Görlitz, M. Wagner-Reetz, D. Kasinathan, R. Cardoso-Gil, W. Carrillo-Cabrera, K. Meier-Kirchner, H. Rosner, and Y. Grin, *Nanostructuring of $Ba_8Ga_{16}Ge_{30}$ clathrates by sol-gel-calcination/chemical-reduction route*, physica status solidi (a) **213**, 774 (2016).

[108] R. Heijl, D. Cederkrantz, M. Nygren, and A. E. C. Palmqvist, *Thermoelectric properties of $Ba_8Ga_{16}Ge_{30}$ with TiO_2 nanoinclusions*, Journal of Applied Physics **112**, 044313 (2012).

[109] M. Christensen, S. Johnsen, M. Søndergaard, J. Overgaard, H. Birkedal, and B. B. Iversen, *Fast Preparation and Characterization of Quarternary Thermoelectric Clathrates*, Chemistry of Materials **21**, 122 (2009).

[110] K. Yamasoto, Y. Osakabe, S. Adachi, S. Munetoh, and O. Furukimi, *A Novel Electric Power Generation Mechanism from Waste Heat without Temperature Gradient*, MRS Advances **1**, 3941 (2016).

[111] Y. Osakabe, S. Tatsumi, Y. Kotsubo, J. Iwanaga, K. Yamasoto, S. Munetoh, O. Furukimi, and K. Nakashima, *Heat–Electric Power Conversion Without Temperature Difference Using Only n-Type $Ba_8Au_xSi_{46-x}$ Clathrate with Au Compositional Density-Gradient*, Journal of Electronic Materials **47**, 3273 (2018).

[112] X. Shi, J. Yang, S. Bai, J. Yang, H. Wang, M. Chi, J. R. Salvador, W. Zhang, L. Chen, and W. Wong-Ng, *On the Design of High-Efficiency Thermoelectric Clathrates through a Systematic Cross-Substitution of Framework Elements*, Advanced Functional Materials **20**, 755 (2010).

[113] S. E. Gustafsson, *Transient plane source techniques for thermal conductivity and thermal diffusivity measurements of solid materials*, Review of Scientific Instruments **62**, 797 (1991).

[114] Y. Ma, J. S. Gustavsson, Å. Haglund, M. Gustavsson, and S. E. Gustafsson, *Pulse transient hot strip technique adapted for slab sample geometry to study anisotropic thermal transport properties of μm-thin crystalline films*, Review of Scientific Instruments **85**, 044903 (2014).

[115] G. Höhne, W. F. Hemminger, and H.-J. Flammersheim, *Differential Scanning Calorimetry* (Springer-Verlag, Heidelberg, Germany, 2003).

[116] Mettler-Toledo, *Heat capacity determination at high temperatures by TGA/DSC Part 1: DSC standard procedures*, Thermal Analysis UserCom **27**, 1 (2010).

[117] M. Ångqvist, W. A. Muñoz, J. M. Rahm, E. Fransson, C. Durniak, P. Rozyczko, T. H. Rod, and P. Erhart, *ICET – A Python Library for Constructing and Sampling Alloy Cluster Expansions*, Advanced Theory and Simulations **2**, 1900015 (2019).

[118] F. Eriksson, E. Fransson, and P. Erhart, *The Hiphive Package for the Extraction of High-Order Force Constants by Machine Learning*, Advanced Theory and Simulations **2**, 1800184 (2019).

[119] K. Parlinski, *Calculation of phonon dispersion curves by the direct method*, AIP Conference Proceedings **479**, 121 (1999).

[120] A. Togo and I. Tanaka, *First principles phonon calculations in materials science*, Scripta Materialia **108**, 1 (2015).

[121] K. Esfarjani and H. T. Stokes, *Method to extract anharmonic force constants from first principles calculations*, Physical Review B **77**, 144112 (2008).

[122] K. Esfarjani, G. Chen, and H. T. Stokes, *Heat transport in silicon from first-principles calculations*, Physical Review B **84**, 085204 (2011).

[123] G. Kresse and J. Furthmüller, *Efficient iterative schemes for ab initio total-energy calculations using a plane-wave basis set*, Physical Review B **54**, 11169 (1996).

[124] J. D. Patterson and B. C. Bailey, *Solid-State Physics: Introduction to the Theory.* (Springer International Publishing, Cham, Switzerland, 2018).

[125] C. Kittel, *Introduction to solid state physics.* (Wiley, New York, USA, 2005).

[126] A. Togo, L. Chaput, and I. Tanaka, *Distributions of phonon lifetimes in Brillouin zones*, Physical Review B **91**, 094306 (2015).

[127] W. Li, J. Carrete, N. A. Katcho, and N. Mingo, *ShengBTE: A solver of the Boltzmann transport equation for phonons*, Computer Physics Communications **185**, 1747 (2014).

[128] Z. Fan, T. Siro, and A. Harju, *Accelerated molecular dynamics force evaluation on graphics processing units for thermal conductivity calculations*, Computer Physics Communications **184**, 1414 (2013).

[129] D. Frenkel, B. Smit, and B. Smit, *Understanding Molecular Simulation: From Algorithms to Applications* (Elsevier Science & Technology, San Diego, United States, 2001).

[130] Z. Fan, H. Dong, A. Harju, and T. Ala-Nissila, *Homogeneous nonequilibrium molecular dynamics method for heat transport and spectral decomposition with many-body potentials*, Physical Review B **99**, 064308 (2019).

[131] J. M. Dickey and A. Paskin, *Computer Simulation of the Lattice Dynamics of Solids*, Physical Review **188**, 1407 (1969).

[132] A. Zevalkink, D. M. Smiadak, J. L. Blackburn, A. J. Ferguson, M. L. Chabinyc, O. Delaire, J. Wang, K. Kovnir, J. Martin, L. T. Schelhas, T. D. Sparks, S. D. Kang, M. T. Dylla, G. J. Snyder, B. R. Ortiz, and E. S. Toberer, *A practical field guide to thermoelectrics: Fundamentals, synthesis, and characterization*, Applied Physics Reviews **5**, 021303 (2018).

[133] Y. M. Belov, S. M. Maniakin, and I. V. Morgunov, in *Thermoelectrics Handbook: Macro to Nano*, edited by D. M. Rowe (CRC Press, Boca Raton, USA, 2005), Chap. 20, p. 1.

[134] G. Will, *Powder Diffraction: The Rietveld Method and the Two Stage Method to Determine and Refine Crystal Structures from Powder Diffraction Data.* (Springer-Verlag, Heidelberg, Germany, 2006).

[135] L. Smart and E. Moore, *Solid state chemistry: an introduction.* (CRC Press, Boca Raton, USA, 2005).

[136] L. B. McCusker, R. B. Von Dreele, D. E. Cox, D. Louër, and P. Scardi, *Rietveld refinement guidelines*, Journal of Applied Crystallography **32**, 36 (1999).

[137] E. Margui and R. Van Grieken, *X-Ray Fluorescence Spectrometry and Related Techniques : An Introduction* (Momentum Press, New York, USA, 2013).

[138] M. Ohring, *Materials science of thin films : deposition and structure* (Academic Press, London, UK, 2002).

[139] H. B. Callen, *Thermodynamics and an introduction to thermostatistics.* (Wiley, New York, USA, 1985).

[140] W. Kohn, *Nobel Lecture: Electronic structure of matter–wave functions and density functionals*, Review Modern Physics **71**, 1253 (1999).

[141] K. Berland, V. R. Cooper, K. Lee, E. Schröder, T. Thonhauser, P. Hyldgaard, and B. I. Lundqvist, *Van Der Waals Forces in Density Functional Theory: A Review of the vdW-DF Method*, Reports on Progress in Physics **78**, 066501 (2015).

[142] K. Berland and P. Hyldgaard, *Exchange functional that tests the robustness of the plasmon description of the van der Waals density functional*, Physical Review B **89**, 035412 (2014).

[143] L. Gharaee, P. Erhart, and P. Hyldgaard, *Finite-temperature properties of nonmagnetic transition metals: Comparison of the performance of constraint-based semilocal and nonlocal functionals*, Physical Review B **95**, 085147 (2017).

[144] E. Fransson, F. Eriksson, and P. Erhart, *Efficient construction of linear models in materials modeling and applications to force constant expansions*, npj Computational Materials **6**, 135 (2020).

[145] T. Mueller and G. Ceder, *Bayesian approach to cluster expansions*, Physical Review B **80**, 024103 (2009).

[146] L. J. Nelson, V. Ozoliņš, C. S. Reese, F. Zhou, and G. L. W. Hart, *Cluster expansion made easy with Bayesian compressive sensing*, Physical Review B **88**, 155105 (2013).

[147] T. Bayes and R. Price, *LII. An essay towards solving a problem in the doctrine of chances. By the late Rev. Mr. Bayes, F. R. S. communicated by Mr. Price, in a letter to John Canton, A. M. F. R. S*, Philosophical Transactions of the Royal Society of London **53**, 370 (1763).

[148] I. Guyon, J. Weston, S. Barnhill, and V. Vapnik, *Gene Selection for Cancer Classification using Support Vector Machines*, Machine Learning **46**, 389 (2002).

[149] J. M. Rahm, J. Löfgren, E. Fransson, and P. Erhart, *A tale of two phase diagrams: Interplay of ordering and hydrogen uptake in Pd-Au-H*, Acta Materialia **211**, 116893 (2021).

[150] B. Sadigh and P. Erhart, *Calculation of excess free energies of precipitates via direct thermodynamic integration across phase boundaries*, Physical Review B **86**, 134204 (2012).

[151] F. Wang and D. P. Landau, *Efficient, Multiple-Range Random Walk Algorithm to Calculate the Density of States*, Physical Review Letters **86**, 2050 (2001).

[152] D. P. Landau, S.-H. Tsai, and M. Exler, *A new approach to Monte Carlo simulations in statistical physics: Wang-Landau sampling*, American Journal of Physics **72**, 1294 (2004).

[153] S.-k. Ma, *Modern theory of critical phenomena*, *Frontiers in physics: 46* (Westview Press, Boulder, USA, 1976).

[154] P. M. Larsen, K. W. Jacobsen, and J. Schiøtz, *Rich Ground-State Chemical Ordering in Nanoparticles: Exact Solution of a Model for Ag-Au Clusters*, Physical Review Letters **120**, 256101 (2018).

[155] A. van de Walle, P. Tiwary, M. de Jong, D. Olmsted, M. Asta, A. Dick, D. Shin, Y. Wang, L.-Q. Chen, and Z.-K. Liu, *Efficient stochastic generation of special quasirandom structures*, Calphad **42**, 13 (2013).

[156] G. J. Snyder, A. H. Snyder, M. Wood, R. Gurunathan, B. H. Snyder, and C. Niu, *Weighted Mobility*, Advanced Materials **32**, 2001537 (2020).

[157] W. Chen, J.-H. Pöhls, G. Hautier, D. Broberg, S. Bajaj, U. Aydemir, Z. M. Gibbs, H. Zhu, M. Asta, G. J. Snyder, B. Meredig, M. A. White, K. Persson, and A. Jain, *Understanding thermoelectric properties from high-throughput calculations: trends, insights, and comparisons with experiment*, Journal of Materials Chemistry C **4**, 4414 (2016).

[158] A. L. Kutepov and A. Ruth, *Electronic structure and thermoelectric properties of CoAsSb with post-DFT approaches*, Applied Physics A **126**, 137 (2020).

[159] X. Hou, Y. Zhou, L. Wang, W. Zhang, W. Zhang, and L. Chen, *Growth and thermoelectric properties of $Ba_8Ga_{16}Ge_{30}$ clathrate crystals*, Journal of Alloys and Compounds **482**, 544 (2009).

[160] C. L. Condron, S. M. Kauzlarich, F. Gascoin, and G. J. Snyder, *Thermoelectric Properties and Microstructure of $Ba_8Al_{14}Si_{31}$ and $EuBa_7Al_{13}Si_{33}$*, Chemistry of Materials **18**, 4939 (2006).

[161] W. R. Puspita, H. Takeya, T. Mochiku, Y. Ishikawa, S. Lee, S. Torii, M. Hagihala, and T. Kamiyama, in *2019 2nd International Conference on Applied Engineering (ICAE)* (IEEE, Batam, Indonesia, 2019), pp. 1–5.

[162] V. Pfeifer, P. Erhart, S. Li, K. Rachut, J. Morasch, J. Brötz, P. Reckers, T. Mayer, S. Rühle, A. Zaban, I. Mora Seró, J. Bisquert, W. Jaegermann, and A. Klein, *Energy Band Alignment between Anatase and Rutile TiO_2*, The Journal of Physical Chemistry Letters **4**, 4182 (2013).